https://lib.uliege.be https://matheo.uliege.be

Master thesis and internship[BR]- Master's thesis : Modelling of Gas Foil Bearing with a high order Discontinuous Galerkin Method[BR]- Integration Internship

Auteur : Alshikh Saleh, Ammar
Promoteur(s) : Hillewaert, Koen
Faculté : Faculté des Sciences appliquées
Diplôme : Master en ingénieur civil en aérospatiale, à finalité spécialisée en "aerospace engineering"
Année académique : 2021-2022
URI/URL : http://hdl.handle.net/2268.2/15884

Avertissement à l'attention des usagers :

Tous les documents placés en accès ouvert sur le site le site MatheO sont protégés par le droit d'auteur. Conformément aux principes énoncés par la "Budapest Open Access Initiative"(BOAI, 2002), l'utilisateur du site peut lire, télécharger, copier, transmettre, imprimer, chercher ou faire un lien vers le texte intégral de ces documents, les disséquer pour les indexer, s'en servir de données pour un logiciel, ou s'en servir à toute autre fin légale (ou prévue par la réglementation relative au droit d'auteur). Toute utilisation du document à des fins commerciales est strictement interdite.

Par ailleurs, l'utilisateur s'engage à respecter les droits moraux de l'auteur, principalement le droit à l'intégrité de l'oeuvre et le droit de paternité et ce dans toute utilisation que l'utilisateur entreprend. Ainsi, à titre d'exemple, lorsqu'il reproduira un document par extrait ou dans son intégralité, l'utilisateur citera de manière complète les sources telles que mentionnées ci-dessus. Toute utilisation non explicitement autorisée ci-avant (telle que par exemple, la modification du document ou son résumé) nécessite l'autorisation préalable et expresse des auteurs ou de leurs ayants droit.

Modelling of Gas Foil Bearing with a high order Discontinuous Galerkin Method

Master's thesis completed in order to obtain the degree of Master of Science in Aerospace Engineering by

Alshikh Saleh Ammar

Supervisors :
Pr. Koen Hilleweart - ULiège
Martin Heylen - Mitis

Jury members :
Pr. Koen Hilleweart - ULiège
Pr. Romain Boman - ULiège
Nayan Leveux - ULiège

University of Liège
School of Engineering and Computer Science
Academic year 2021-2022

Acknowledgements

Now that this work is done, I would like to thank, with a few lines, all those involved in achieving this work, either directly or indirectly.

First of all, I would like to express my deepest gratitude to my professor and academic supervisor, Koen Hilleweart, for teaching me, encouraging me to do this interesting subject, and guiding me throughout this work. This endeavour would not have been possible without his thoughtful, valuable and constructive comments and his sharing of knowledge and time. I would also like to thank all ForDGe team members of the ULiège for accounting me as a member of their group and for their kindness and advice. A special thanks are addressed to Nayan Leveux, who helped me first integrate the ForDGe team and do my first steps in the code and throughout the whole project. I would like to thank him for his kindness and his unfailing availability throughout the semester. Furthermore, I would like to thank Pr. Romain Boman, for taking the time to be a member of the jury.

I would like to extend my sincere thanks to my industrial supervisor Martin Heylen for following my work progress and providing all the necessary information concerning foil bearings. I am also grateful to Michel Delanaye for giving me the opportunity to do my internship within his wonderful company. Thanks should also go to Mehdi Roubah, Andres Giraldo, Jojomon Joseph, Danish Rehman and all Mitis personnel for their kindness and encouragement.

Finally, all my gratitude goes to my parents, Omar and Safaa, who gave me the opportunity to study in a very supportive, reassuring, friendly and lovely environment for all these years. Words cannot express my gratitude to them for their love, help, constant support and their patience even in difficult times. I also extend my gratitude to my sister Raghad for supporting me with their amazing homemade desserts and my brother Ahmad for helping me changing mode with his good humour. Thanks also should go to Marwa, my older sister, her husband Omran Zaki and her beautiful girl Salma for their encouragement. Once again, thank you all.

Nomenclature & Abbreviations

Abbreviation

AFB	Air Foil Bearing
BC	Boundary Condition
FD	Finite Difference
FE	Finite Element
FV	Finite Volume
GFB	Gas Foil Bearing
ODE	Ordinary Differential Equation
PDE	Partial Differential Equation
SEFM	Simple Elastic Foundation Model

Symbols

α	Bearing compliance
β	Pad angular extend, $\beta = \theta_t - \theta_l$
Λ	Compressibility/Bearing number
μ	Dynamic viscosity
μ_f	Friction coefficient
ν_b	Bump foil Poisson's ratio
ν_t	Top foil Poisson's ratio
ω	Journal/Shaft angular speed
Φ_L	Load angle
ρ_b	Bump foil material density
ρ_t	Top foil material density
θ	Circumferential coordinate, $\theta = x/R$
θ_0, ϕ_0	Angular position of h_{min}, $\phi_0 = \theta_0 - \pi$
θ_b	Bump half angle
θ_i	i-th pad inlet slope angle
θ_l	First pad leading edge angle
θ_s	Inlet slope extend
θ_t	First pad leading edge angle
θ_{li}	i-th pad leading edge angle
θ_{ti}	i-th pad trailing edge angle
$\tilde{p}_m$	Maximum film pressure
C	Radial Clearance
e, ε	Journal/Shaft eccentricity, $\varepsilon = e/C$
E_b	Bump foil Young's Modulus
E_t	Top foil Young's Modulus
h, $\tilde{h}$	Film height, $\tilde{h} = h/C$
h, $\tilde{h}_c$	Film height (compliant), $\tilde{h}_c = h_c/C$
h, $\tilde{h}_r$	Film height (rigid), $\tilde{h}_r = h_r/C$
h, $\tilde{h}_s$	Slope height, $\tilde{h}_s = h_s/C$
h_b	Bump foil height
h_m	Minimum film thickness
K	Bump structural stiffness, $K = \alpha C/p_a$
L, $\tilde{L}$	Bearing length, $\tilde{L} = L/R$
l_b	Bump half length
N_b	Number of bumps
N_p	Number of bearing pads
$N_{x,z}$	Number of elements in x and z direction
p, $\tilde{p}$	Film pressure, $\tilde{p} = p/p_a$
p_a	Ambient pressure
R	Journal/Shaft radius
R_b	Bump radius of curvature
s_b	Bump foil pitch
t_b	Bump foil thickness
t_t	Top foil thickness
W, $\tilde{W}$	Static load, $\tilde{W} = W/(p_a R^2)$
$x, y, z, \tilde{z}$	Cartesian coordinates, $\tilde{z} = z/R$

Contents

List of Figures

List of Tables

Chapter 1

Introduction

1.1 Context

Year on year, a significant portion of the technology that has transitioned to modern society relies on rotating machinery, also called turbomachinery. Indeed, in modern turbomachinery applications, the trends tend to higher speeds and weight reduction through improved prediction of rotor dynamics. Bearings have been substantially used in turbomachinery applications for three reasons: reducing friction and allowing a smoother rotation, protecting the part that supports the rotation, and maintaining the rotating shaft at its nominal position. Various bearing designs exist (see Fig. 1.1) depending on the application to be correctly met for maximum efficiency, durability, reliability, and performance.

The concept of Gas Bearing that operates on the hydrodynamic lubrication principle appeared as an alternative for existing liquid-lubricated bearings. The main advantages of this technology are that it increases the service life and offers an oil-free operation ultimately. Recently, a particular class of gas bearings called foil bearings began to receive widespread convergence in many scientific publications [33]. Despite its origins in rigid gas bearings, Gas Foil Bearings (GFBs) have evolved to overcome physical limitations during operations, namely the use of low viscosity fluids and modest self-generated hydrodynamic fluid film pressures [30]. Therefore they were widely used in microturbomachinery because of their advantages for reducing system complexity, maintenance costs, and easing in temperature limitations [7]. Moreover, they also offer other advantages: (1) environmental durability, (2) higher reliability in operations, since no lubrication is needed to feed the system and therefore no maintenance is scheduled, and (3) higher load capacity at high-speed [17, 67]. In this context, GFBs have demonstrated superior reliability in Air Cycle Machines (ACMs) used in aircraft environment control systems compared to the ball bearings used previously. Consequently, all the ACMs of civil and military aircraft built since 1988 have been equipped with GFBs [18]. In addition, other advanced turbomachinery systems that utilize GFBs, with air as a lubricant, exist (micro gas turbines [52, 25], turbochargers [50], air cycle machines [12] and many others).

1.2 Bearing Technology Development

Recent technological advances in turbomachinery led to the development of many foil bearing structures. In terms of bearing modelling, the flexibility of the geometry is directly related to fluid film pressure and results in improved performance. In general, foil bearings are made of one or more compliant layers topped by one or more layers of top foil surfaces. The main goal of the compliant surface is to provide structural stiffness and comes in several configurations such as leaf-type and bump-type [43]. Different Bump-type foil bearings exist depending on their operating parameters, and their geometry [33]. A widely accepted classification of GFBs into first, second and third generations was introduced by DellaCorte [21] based on the foil geometry and thus stiffness distribution. The earliest bearings design, known as the first generation,

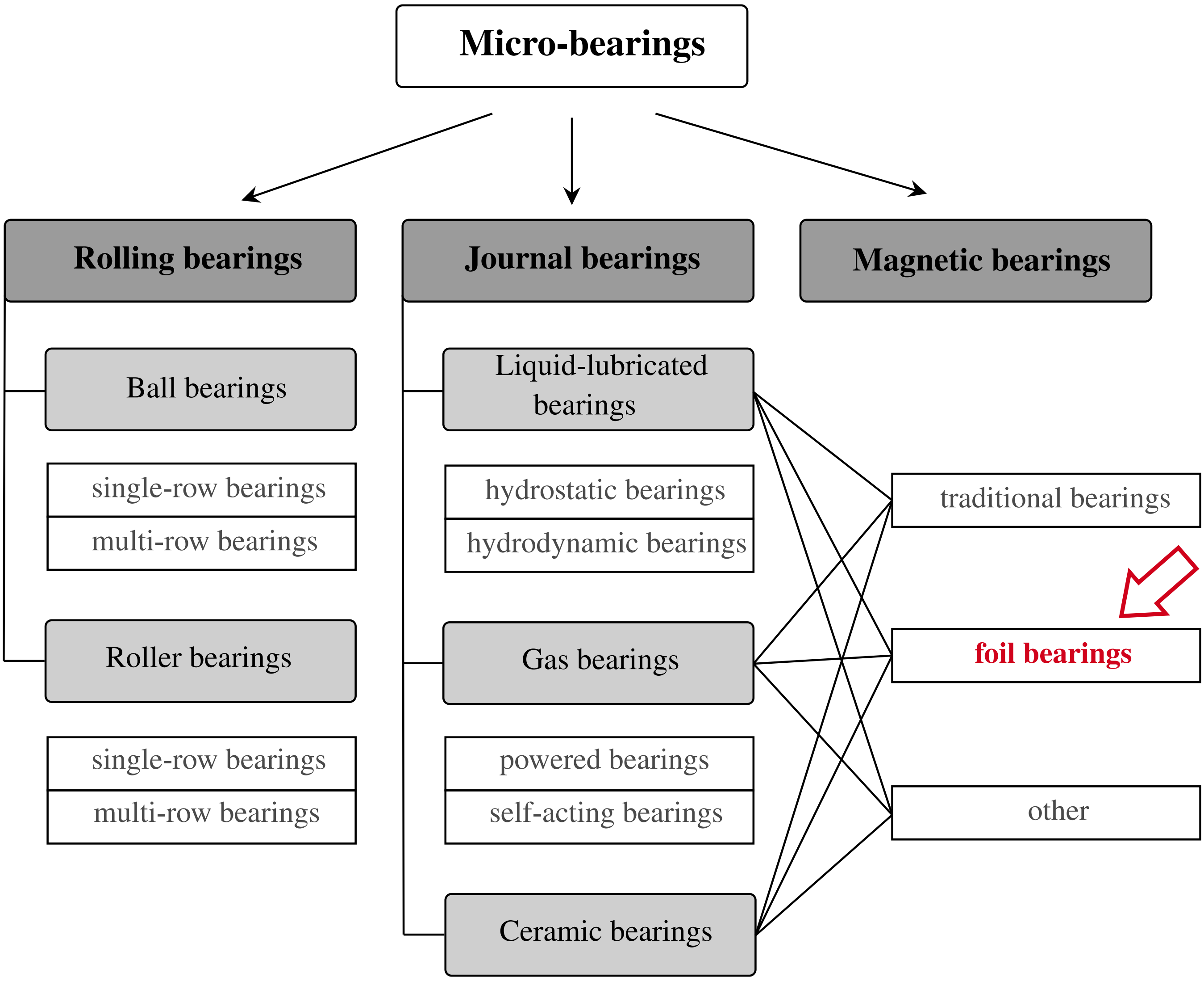

Figure 1.1: Microbearing classification in view of bearing structure and operating principle. Position of foil bearings in the classification of microbearings [33].

was developed by Mohawk Innovative Technology Incorporation (MITI) and mainly supported by the National Aeronautics and Space Administration (NASA). The bearing has uniform compliant surface geometry in both circumferential and axial directions. Therefore, such a compliant structure's stiffness characteristics are more or less constant. This kind of bearing has a relatively simple structure, sound damping, and endurance for misalignment [62]. However, its application field was limited to high-speed to lightly loaded systems. In this context, more advanced designs were developed to be known as the second generation. In these bearings, the compliant structure's stiffness characteristic varies axially or circumferential. This design is achieved by using variable pitch in the desired direction. Indeed, by controlling the foil support structure in a given direction (most frequently in the axial direction), physical phenomena like edge-leakage caused by the lubricant can be accommodated, leading to better performance and hence increasing the load capacity ([21, 33]). Later, the third generation of GFBs in which stiffness distribution varies in both directions simultaneously was developed. Such bearings show improvements in load carrying capacity so that they are used in microturbines and devices in which first and second-generation bearings could not be used due to the heavily loaded conditions [33]. Advancements in foil bearing technology have led Heshmat et al. and MITI to develop fourth, fifth and sixth generation GFBs, distinguished by their coatings and operating temperature ranges [60]. This seems to improve the dynamic characteristics of the bearing and also enhance its load capacity [62].

1.3 Working principle

GFBs are compliant-surface hydrodynamic bearings that use gas, usually air, as a lubricant. Typical GFBs consist of four main parts (see Fig. 1.2): the bearing housing, also called sleeve (Steel 316L), the rotating shaft (Steel 316L) and the top foil, supported by a series of corrugated bump strip layer (Inconel X718 or Inconel X750), acting as springs and thus providing the tunable structural stiffness. The top foil and the bump strip are welded to the bearing housing at their leading edges and are free at the trailing edge. Coulomb-type damping arises due to material hysteresis and dry-friction between the bumps strip and top foil, and the bumps and the bearing housing [43].

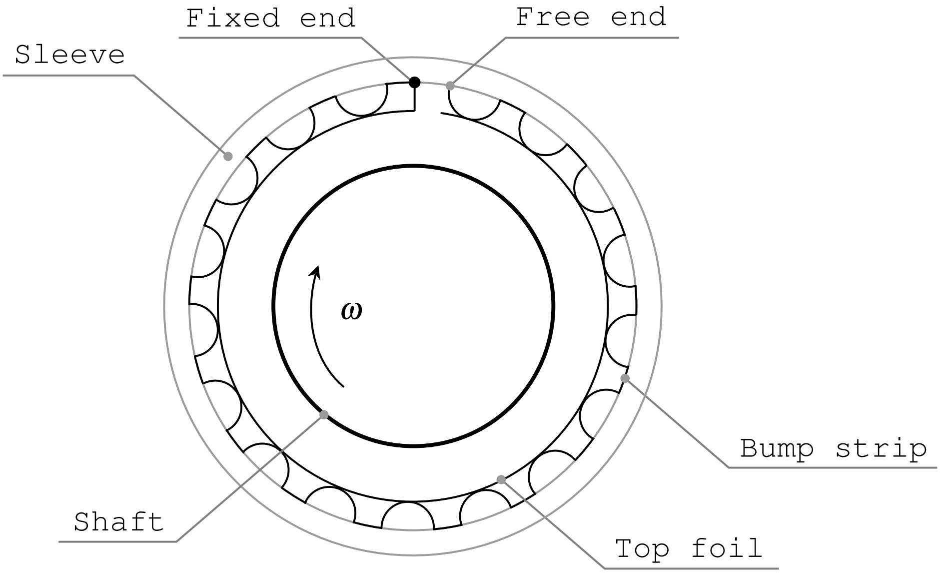

Figure 1.2: First generation bump-type foil bearing component nomenclature.

The working principle is relatively simple; initially (at spin-off), the bump foil trailing edge is in contact with the top foil, which is in contact with the shaft. Once the shaft is spinning fast enough, a hydrodynamic film is created, and the air pushes the foil away from the shaft, ensuring no contact and wear occurs between the foil and the shaft. High pressure generated by the shaft's rotation separates thus the shaft from the foil structure. Misalignment of the shaft leads to a local increase of the pressure at the region of minimum thickness, pushing the shaft away from the foil, and preventing any contact. The system acts thus as a controller/damper for the perturbation caused by the misalignment of the shaft. The local pressure increase depends on the level of misalignment, and thus high misalignment leads to higher values of local pressure since the film thickness at this location becomes smaller. Note that for single pad foil bearing, known as first generation (see Fig. 1.2), the direction of rotation is always from the free end (trailing edge) of the pad towards the attached end (leading edge) to prevent the pad being ripped off by Eytrlwein winch forces [54]. For bearings with multiple pads, rotation can go both ways.

1.4 Literature Review

The theoretical foundation for hydrodynamic lubrication was first established and published in the Proceedings of the Royal Society by Reynolds in 1886 [1]. The theory was then detailed and confirmed with Beachamp Tower's experimental data on hydrodynamic lubrication, which was available then. The result was that a viscous liquid could separate two sliding surfaces by hydrodynamic pressure, with lower friction and, theoretically, no wear [45].

At the beginning of the 20th century, the hydrodynamic lubrication theory started getting widespread. Michel and Kingsbury applied the theory of hydrodynamic lubrication to thrust bearings. The result was the development of the pivoted pad bearing. Additionally, in 1904 Sommerfeld published the complete analytical solution for the full infinite journal bearing with periodic Boundary Conditions (BCs) (same pressure at the domain ends, *i.e.* $\theta = 0°$ and $\theta = 360°$). The solution was a simplification of the original Reynolds's work in 1886. He assumed the solution to be continuous for the full 360° journal bearing, leading to skew-symmetric pressure distribution, with pressure lower than the ambient pressure in the divergent region. However, such behaviour is rarely encountered in real bearings since fluids used in lubrication cannot withstand pressures below their vapour pressure, and the supply pressure is usually small compared with the one generated inside the film [3]. In 1925, Gümbel suggested neglecting the negative part of the Sommerfeld solution and focusing only on the convergent region (see [19],[35]). This leads to more realistic predictions of some bearing's characteristics. However, this leads to a violation of the continuity of mass flow at the end of the convergent region (*i.e.* $\theta = 180°$) [35]. For this purpose, Cameron and Wood [3] used the correct set of BCs, put by Reynolds ([1]). Results showed good agreement with experimental data provided by Nücker in 1932.

Blok and Rossum first introduced the concept of GFBs in 1953. The authors mentioned that such a bearing results in a larger film thickness than a conventional rigid bearing and can increase efficiency, reliability and operating life. Heshmat et al. [10] first presented an analysis of bump-type gas foil journal bearing with compliant foil as the bearing surface. The compliance foil is represented by an elastic foundation in which the top foil is neglected. The stiffness of the bump foil is coupled to the compressible steady-state Reynolds equation through the film height equation, and the gas film hydrodynamic pressure is coupled to a local deflection of the bumps. The bumps deform elastically, and the deflection is proportional to the local pressure difference $(p - p_a)$ through structural compliance α that depends on the bump material and geometrical properties. This model is the simplest one, named the Simple Elastic Foundation Model (SEFM). The authors also detailed the bearing's static load performance for single and multi-pad configurations and pointed out a series of advantages compared to the conventional gas journal bearing. Indeed, complaint foil bearing exhibits higher load capacity at high speed for a given minimum clearance, lower power losses and superior qualities in high-temperature operation.

The stiffness of the SEFM presented by [10] is calculated based on the analytical single-bump expression of Wallowit (1973). In this theory, the bump-bump interaction, as well as the frictional effects, are neglected. Accordingly, theoretical and experimental studies ([11],[14]) have found this expression to underestimate the foil stiffness compared to an actual multi-bump foil. The authors presented a theoretical and experimental model of a bump foil strip deformation in compliant foil bearings. At that period, the model was complete since local interaction forces, variable load distributions, bump geometries, and friction forces between the bump foil and the bearing housing or the top foil were considered. The authors pointed out that the bumps near the fixation have a much higher stiffness (lower deflection) than those near the free end. For the bump geometry effects, results showed an increase in the stiffness for increasing bump thickness or height and decreasing length. However, this type of direct modelling requires a long computation time for solving coupled structural and aerodynamics problems. That was the motivation for the second formulation for the single bump static stiffness, developed by Iordanoff [20]. Contrary to Wallowit and Anno's analytical expression, this model considers friction between the bumps and the bearing housing and provides analytical expressions for the stiffness per unit area for a single bump with either its two ends free or one free and the other fixed. More advanced model including top foil sagging effect (= deflection of the top foil between the bumps) and bump-bump interactions ([28], [53]). In [28], a multidegree of freedom model of interacting bumps describing the foil bearings was developed. Each bump comprises three degrees of freedom (DOFs), horizontal and vertical displacement and rotation. The bumps are linked via elementary springs with analytically expressed stiffness so that the model can be adjusted for a wide range of diameters and material properties. Therefore, this model can be easily integrated into a foil bearing prediction code. Compared with finite element simulations, results for various loads and friction coefficients showed good agreements.

Furthermore, Peng and Carpino ([15],[16]) presented Finite Difference (FD) formulations to estimate the stiffness and damping coefficients of an elastically supported GFB. A perturbation method is used to obtain the linearized dynamic equations. The model solves the compressible Reynolds equation by considering a perfectly extensible top foil and a series of corrugated bumps. In [15], the effect of structural compliance on the dynamic coefficients is discussed, with the assumption of no damping in the foil foundation structure. The work was followed by [16] that investigated the damping effects on a sub-foil structure. The stiffness and damping coefficients were calculated for different values of Coulomb friction. It was shown that as the Coulomb friction achieved by the relative motion (that occurs when the elastic foundation deflects under loading) between the bump foil and the bearing housing increases, the stiffness and the damping coefficients of the bearing increase. This feature is not available in conventional rigid bearings.

Kim and San Andrés [31], in comparisons with experimental data test by Ruscitto [9], validate heavily loaded GFB static and dynamic force characteristics implementing the SEFM. The model uses an averaged pressure enabling a journal to move beyond its nominal clearance when it is supposed to high static load. At high static load, predictions show eccentricities that exceed the bearing's nominal clearance (about three times). Predictions for minimum film thickness and attitude angle for increasing load show good agreement with the experimental data test for moderately to heavily loaded GFB. At low static load, discrepancies appear between the predicted and experimental results due to fabrication inaccuracy of the tested bearing. The same authors tried to provide a more realistic model for the top foil that was neglected in the SEFM. Indeed, conventional models consider only the stiffness of the bumps, uniformly distributed around the circumference of the bearing. The authors presented two more complex finite element (FE) models for the top foil elastic structure [34]. The models couple the elastic deflection of the 1D beam-like or 2D shell top foil to the bump deflection. Both are coupled to the gas film hydrodynamics. Compared to the experimental results, the 1D FE model shows better agreement than the second model for the minimum film thickness predictions. Moreover, the model shows improvement over the SEFM as it considers sagging and foil fixation effects. The 2D FE model overestimates the minimum film trickiness at the centerline while underestimates it at the bearing edges. Both models lead to lower bearing stiffness and damping predictions than the SEFM.

In 2004 Peng and Khonsari [23] developed a numerical procedure to predict the hydrodynamic performance of both first and second-generation foil bearing. The model considers air compressibility effects and provides results about pressure distribution, operating hydrodynamic film thickness, load-carrying capacity and attitude angle for a wide range of operating speeds. Good agreement with existing experimental data provided by Ruscitto [9] is shown.

The above-cited paper has been used as a reference by many researchers. Sankar [55] presented a methodology based on the pseudo-spectral scheme to solve the compressible Reynolds equation. The scheme is coupled to a structural model of the foil structure. Both 1D and 2D cases are investigated, and the results were validated with [23]. The authors pointed out that, despite its relative simplicity, such a pseudo-spectral scheme increases solution accuracy for a given stencil size compared to FE or Finite Volume (FV) scheme. Both models (Peng and Khonsari and Sankar) are based on the Wallowit expression for estimating structural stiffness. At that period, Patil et al. studied the static performance of a GFB using the SEFM developed by Heshmat [10]. The characteristic of the bearings is investigated by changing the foil pivot. The effect of eccentricity ratio, bearing number, bearing compliance, and length to diameter ratio on the load-carrying capacity is compared to reference cases [10, 16]. Later, Leister et al. presented a numerical procedure resolving the compressible Reynolds equation coupled to an inherent structural foil model. The implemented segmented foil model works for static and transient simulations and considers the top foil sagging effect and resulting ripple-like film thickness variations. Results show agreement with reference model [34]

Recently, Osmanski published his doctoral thesis about the modelling of GFBs. The aim is to understand GFBs better and improve existing modelling tools. The work comprises a detailed analysis of the fluid film, the foil structure and the rotor dynamics of the three pads GFB manufactured by Siemens. The author combines a truss-based bump foil, a beam-based top foil model (including foil mass) and a smooth friction model. After comparing with experimental result [54], it was demonstrated that a dynamic friction model is insufficient to explain differences between numerical and experimental results. Thus, a model allowing sticking would be required. The author also presented a new GFB simulation tool based on an FV discretization of the Reynolds equation coupled to foil and rotor models along with clearly defined interfaces. The foil model is based on the analytical springs stiffness coefficients provided by [28]. The stability of such a bearing is also discussed.

1.5 Motivation and Objectives

To meet customer's specifications and remain ahead of its competitors, Mitis SA is developing a new generation of clean energy converters for decentralized Combined Heat and Power (CHP) based on flameless combustion chamber microturbines. Target markets include micro-biomechanization and collective building heating CHP, off-grid power generation for telco and remote communities, and range extenders for vehicles and leisure boats. For this purpose, engineers are constantly working in the R&D department on the different components through numerical simulations. The results are then compared to experimental data performed in the laboratory. Mitis SA is using Air Foil Bearings (AFBs) in their systems to avoid any oil lubrication, guaranteeing an oil-free system and increasing reliability. Therefore, Mitis SA is interested in developing a simulation methodology to evaluate the performance of AFBs based upon the methodology of Von Osmanski [65]. The work presents complete and advanced modelling of the AFB based on a multiphysics coupling of shaft kinetics, flows equations and foils structure deformations, including frictional considerations. The air bearings are provided by Omega Dot, a British company that design, develop and test the latest concepts in oil-free turbomachinery. A schematic of foil bearing used in Mitis SA is available in Fig. 1.3c and 1.3d.

The overall objective of this work is to contribute to a better understanding of the AFB technology. In fact, any model aiming to predict the dynamics of a GFB-supported rotor must deal with three distinct domains, as depicted in Fig. 1.4. In this report, only the second part representing the behaviour of the lubrication gas film is investigated. First, numerical simulations of the isothermal, steady state Reynolds equation with the use of Discontinuous Galerkin Finite Element Method (DG-FEM) are performed. Such a method has several advantages over classical FV and FD methods that most authors use for their numerical recipes. These advantages are cited in chapter 4. Next, the modelling of the foil structure is done based on existing models. Three expressions are used for the estimation of the foil structure stiffness. Finally, the coupling between structural and fluid parts is done at the level of the film thickness using the SEFM. This work would be recognized as the reference, providing numerical results for GFBs used by Mitis SA and/or any kind of gas foil journal bearing with variable geometries and different working gases and operating conditions.

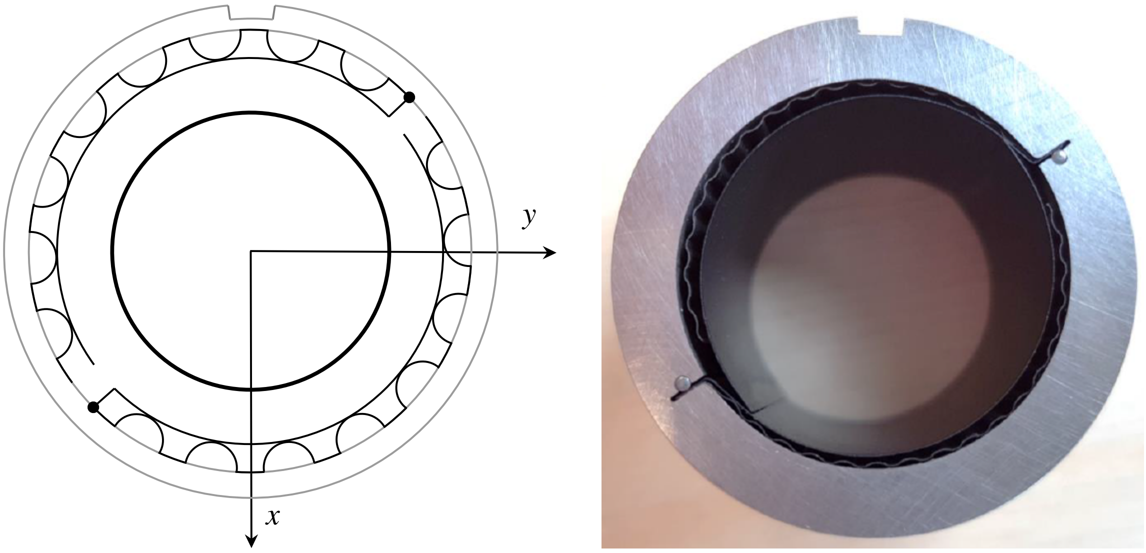

(a) (b)

Figure 1.3: Schematics of the air foil bearing developed by Omega Dot and used by Mitis SA.

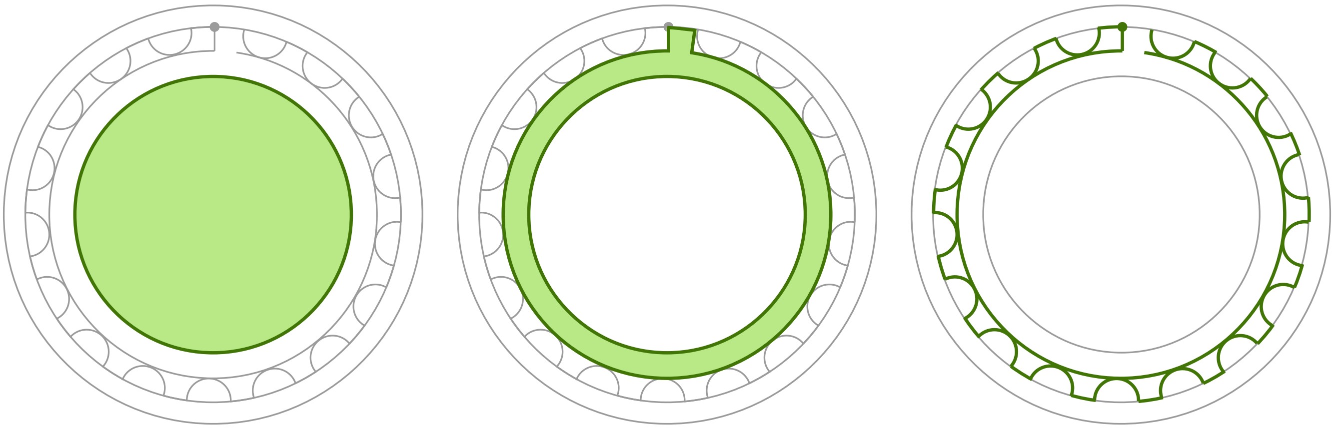

(a) (b) (c)

Figure 1.4: Domains that can be treated in a GFB model: (a) the journal/rotor, (b) the lubricating gas film, and (c) the compliant foil structure.

1.6 Outline of the thesis

The present work is organised in three main parts: *Theoretical Background*, *Numerical Methods* and *Results*. In particular, it is divided into seven chapters

Chapter 2 introduces the theory of gas film lubrication in general and the gas journal bearings in particular. The mathematical derivation of the steady state Reynolds equation and its simplifying assumptions are given. Some existing analytical and limiting case solutions are presented for both rigid and foil bearings. Dimensional analysis is done to highlight the important design parameters for both cases (rigid and foil).

Chapter 3 apply the gas film lubrication theory to GFBs. The mathematical modelling of the GFB is separated into two parts: modelling the fluid film and the foil structure. Three existing models for the foil structure are presented and discussed.

Chapter 4 gives a detailed theoretical background of the numerical approach followed in this work (DG-FEM) and its advantages and drawbacks. The detailed mathematical development is presented and then applied to the Reynolds equation. The strategy used to couple the diffusive and convective parts of the problem and the different resolution techniques are presented.

Chapter 5 validate the numerical model based on existing published data. Two different sections for rigid and foil bearings are presented, and a mesh convergence study is performed to eliminate any errors that may come from mesh resolution.

Chapter 6 highlight some of the main results obtained in the case of foil bearings with a compressible fluid. Parametric studies showing the effect of the design parameters on load-carrying capacity are performed. In particular, three bearings geometries that differ in the number of pads and foil geometry are investigated and compared.

Chapter 7 focuses the analysis on the bearing developed by Omega Dot and used by Mitis SA. The effects of operating conditions (rotation speed, temperature) and axial clearance variation are shown.

THEORETICAL ASPECTS

Chapter 2

Steady State Reynolds Equation

This chapter presents the derivation of the classical Reynolds equation based on the original work of Reynolds [1]. In the work of Reynolds, the analysis was restricted to incompressible fluids. Harrison lifted this unnecessary restriction in 1913, which included the compressibility effects. Mathematically, the Reynolds equation is a partial differential equation (PDE) governing the pressure distribution in fluid film lubrication. It can be derived in several ways. Indeed, since it is a combination/simplification of the Navier-Stokes continuity and momentum, it can be derived from this basis. However, it is more often derived by considering the equilibrium of an element of liquid subjected to viscous shear and applying the continuity of flow principle [45]. The solution of the Reynolds equation gives the pressure distribution in a bearing with an arbitrary film shape. From this last, all the bearing performance parameters such as the load-carrying capacity, attitude angle, friction force, and many others can be easily calculated.

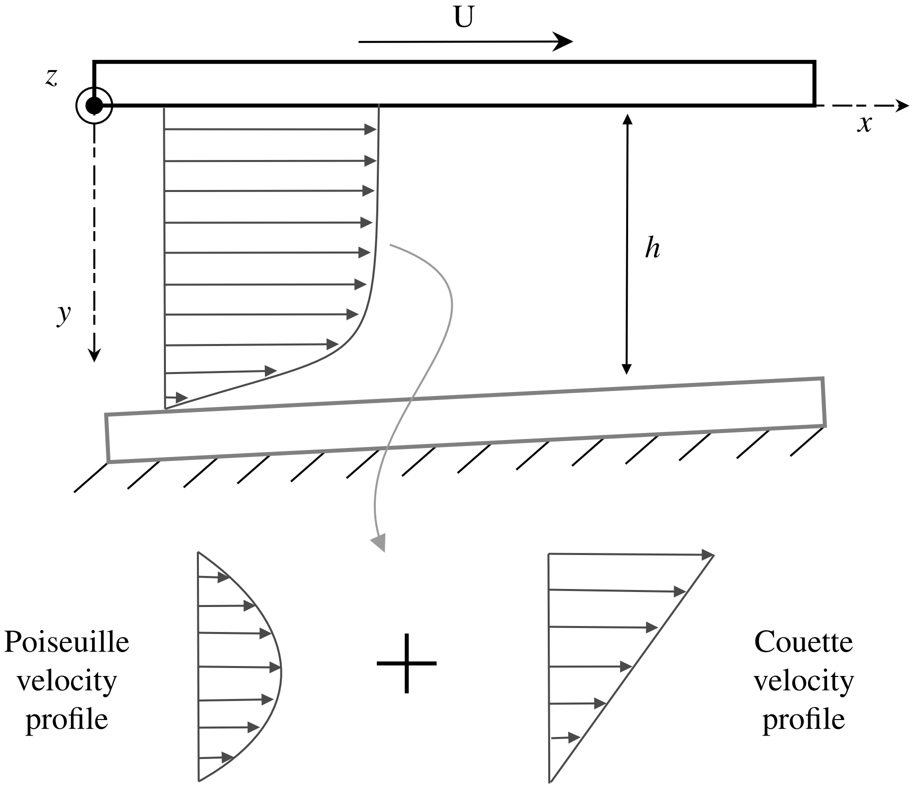

Figure 2.1: Simplified schematic and velocity profile at the entry of the hydrodynamic film [45]. The velocity profile combined two distinct effects. The Poiseuille flow show a parabolic velocity distribution through the film height, while the Couette flow results in a linear velocity profile.

2.1 Simplifying Assumptions

Consider a three-dimensional journal bearing configuration with a film gap, noted h as shown in Fig.2.1. The inner/top surface is undergoing a sliding motion at constant velocity U while the outer/bottom surface that corresponds to the bearings housing/sleeve surface is not moving. Let Cartesian coordinate system (x,y,z) denote the coordinates along the direction of the flow, the radial direction and the direction parallel journal/shaft axis. The following key assumptions, used later on in the derivation, are valid in the majority of encountered applications [58]

- The fluid is assumed to be Newtonian
- The flow is laminar. In the presence of turbulence, a modified form of the Reynolds equations must be used
- Inertia and body forces are assumed to be negligible compared to viscous forces. In advanced analysis, the inertia effects are considered.
- Viscosity is constant throughout the fluid film
- Squeeze motion is negligible

The small thickness of the hydrodynamic film allows considering the following simplifying assumptions

- Variation of pressure across the film thickness is assumed to be small, i.e. $\frac{\partial p}{\partial y}$, so that the pressure is only a function of the tangential and axial direction. This assumption is justified by Dowson (1962) since the film thickness is in the order of micrometres
- Curvature effects are negligible: the film thickness is small compared to the bearing radius $(h/R <<)$, so the physical domain can be unwrapped. This allows using Cartesian coordinate system [58]

2.2 Mathematical Derivation

With the assumptions listed in section 2.1, the momentum equations in the three directions write

$$\frac{\partial p}{\partial x} = \frac{\partial}{\partial y}\left(\mu \frac{\partial u}{\partial y}\right) \tag{2.1}$$

$$\frac{\partial p}{\partial y} = 0 \tag{2.2}$$

$$\frac{\partial p}{\partial z} = \frac{\partial}{\partial y}\left(\mu \frac{\partial w}{\partial y}\right) \tag{2.3}$$

with p the pressure film, μ the dynamic viscosity, u and w the velocity components in the x and z direction respectively. Integrating Eq. (2.1) with respect to y

$$u(y) = \frac{1}{2\mu}\frac{\partial p}{\partial x} y^2 + Ay + B \tag{2.4}$$

The constant of integration A and B are determined using the no-slip boundary condition at the outer/bottom surface and the sliding motion of the inner/top surface induced by the rotation of the shaft. Substituting in Eq. (2.4) the expressions of A and B leads to

$$u(y) = \frac{1}{2\mu}\frac{\partial p}{\partial x}(y^2 - hy) + U\frac{h-y}{h} \tag{2.5}$$

where the first and second terms represent the motion due to pressure gradient (Poiseuille flow) and the motion by shear driven effect due to the motion of the top surface (Coette flow) respectively. A similar analysis is done to find the velocity component w

$$w(y) = \frac{1}{2\mu}\frac{\partial p}{\partial z}(y^2 - hy) + W\frac{h-y}{h} \tag{2.6}$$

The conservation of mass in the compressible case writes

$$\frac{\partial \rho}{\partial t} + \frac{\partial(\rho u)}{\partial x} + \frac{\partial(\rho v)}{\partial y} + \frac{\partial(\rho w)}{\partial z} = 0 \tag{2.7}$$

with ρ the fluid density. The Reynolds equation is obtained by substituting u and w into Eq. (2.7) and integrating over the film thickness h

$$\begin{aligned} \frac{\partial(\rho u)}{\partial x} + \frac{\partial(\rho w)}{\partial z} &= 0 \\ \int_0^h \frac{\partial \rho}{\partial t} dy + \frac{\partial}{\partial x}\int_0^h \rho u\, dy + \frac{\partial}{\partial z}\int_0^h \rho w\, dy &= 0 \\ \frac{\partial}{\partial x}\left(\rho\left[-\frac{h^3}{12\mu}\frac{\partial p}{\partial x} + \frac{Uh}{2}\right]\right) + \frac{\partial}{\partial z}\left(\rho\left[-\frac{h^3}{12\mu}\frac{\partial p}{\partial z} + \frac{Wh}{2}\right]\right) &= 0 \\ \frac{\partial}{\partial x}\left(\frac{\rho h^3}{12\mu}\frac{\partial p}{\partial x}\right) + \frac{\partial}{\partial z}\left(\frac{\rho h^3}{12\mu}\frac{\partial p}{\partial z}\right) &= \frac{\partial}{\partial x}\left(\frac{\rho U h}{2}\right) + \frac{\partial}{\partial z}\left(\frac{\rho W h}{2}\right) \end{aligned} \tag{2.8}$$

Assuming that U and W are not function of x and z respectively, and no motion in the axial direction $(W = 0)$ it comes

$$\frac{\partial}{\partial x}\left(\frac{\rho h^3}{12\mu}\frac{\partial p}{\partial x}\right) + \frac{\partial}{\partial z}\left(\frac{\rho h^3}{12\mu}\frac{\partial p}{\partial z}\right) = \frac{U}{2}\frac{\partial}{\partial x}(\rho h) \tag{2.9}$$

which represents the simplified steady state two dimensional Reynolds equation describing the behavior of fluids in most known bearing configurations. For compressible flow, an equation of states is required since the density varies. Ideal gas law suggests the polytropic relation $\rho = k\,p^{1/n}$, where k is a constant and n the polytropic index. This last can be set to 1 by assuming isothermal process, which is valid since bearing surfaces are nearly isothermal. The Reynolds equation can be rewritten as

$$\frac{\partial}{\partial x}\left(\frac{ph^3}{12\mu}\frac{\partial p}{\partial x}\right) + \frac{\partial}{\partial z}\left(\frac{ph^3}{12\mu}\frac{\partial p}{\partial z}\right) = \frac{U}{2}\frac{\partial}{\partial x}(ph) \tag{2.10}$$

which is an hyperbolic-elliptic differential equation for the pressure. Appropriate boundary conditions specifying the pressure value at inlet and outlet are usually required. Note that for one dimensional case, especially for infinitely long journal bearing, the second term in the left hand side of equation Eq. 2.10 drops since $\partial p/\partial z = 0$.

2.3 Limiting Cases and Closed-Form Solutions

The general Reynolds equation, as it appears in Eq. (2.10) is strongly non-linear. Consequently, no direct analytical solution exists. The following limiting cases can be considered:

- **Incompressible solution** At low bearing number ($U \to 0$), pressure rise tends to zero and the effect of compressibility diminishes. Thus, the solution to the Reynolds equation reduces to the incompressible case

$$\frac{\partial}{\partial x}\left(\frac{h^3}{12\mu}\frac{\partial p}{\partial x}\right) + \frac{\partial}{\partial z}\left(\frac{h^3}{12\mu}\frac{\partial p}{\partial z}\right) = \frac{U}{2}\frac{\partial h}{\partial x} \tag{2.11}$$

- **Compressible solution** When the bearing number is high ($U \rightarrow \infty$), a limiting solution can be obtained by solving the compressible Reynolds equation as it appears in Eq. (2.10).

The limiting cases are indeed used to bound the actual solution (pressure, load carrying capacity, etc...) that lies between these limiting solutions.

Journal bearings

For a full 360° infinitely long journal bearing, analytical limiting expressions exist for the pressure, dimensionless load, friction coefficient and other parameters. Those are available in the original source [58]. Additionally, some publishers have tried to solve the Reynolds equation analytically under some assumptions. Tab. 2.1 shows some existing analytical solutions of the Reynolds equation in the case of journal bearing. The several presented solutions differ in the form of the equation to be solved (1D, 2D, incompressible, compressible) as well as the BCs to be applied/imposed (Periodic, Dirichlet, Neumman).

Sommerfeld developed an incompressible analytical solution for the full infinite journal bearings with periodic BCs for the pressure. The obtained pressure distribution is skew-symmetric, continuous with pressure lower than ambient value in the divergent region. Later on, Gümbel extended this theory to journal bearings with liquid as working fluid. The negative part of the Sommerfeld solution has been neglected to represent better the actual functioning of bearings operating with liquid. Periodic BCs have been used at the limits of the convergent region.

Cameron and Wood solution came as an improvement of the Gümbel solution since this last leads to a violation of the continuity of mass flow at the end of the domain. The authors use Reynolds BCs consisting of imposing Dirichlet condition (ambient pressure) and Neumman condition (zero gradient) at the domain's beginning and end, respectively. For compressible case, Ausman introduced a linearized ph solution for the finite self-acting lubricated journal bearing. This model corrected the deficiency of the first-order perturbation solution at high eccentricity ratios. Indeed, the first model yields a linear load-eccentricity dependency; thus, the linearization is only valid for small eccentricity ratio values (< 0.3). The second model differs from the first one in the definition of the dependent variable (here ph). The method provides analytical expressions for a two-dimensional compressible case's pressure and load-carrying capacity. The cited cases will be further used as validation cases for the journal bearing. Other analytical solutions for the finite journal bearings exit; some are reported in Tab. 2.1.

Foil bearings

Direct analytical solutions for foil bearings do not exist due to the additional complexity in the structural modelling. However, Peng and Khonsari [23] developed a numerical procedure based on FD method to predict the pressure distribution and the eccentricity ratio of foil bearings based on a minimum imposed film thickness. Results concerning the load-carrying capacity have been compared to those obtained with Dellacorte and Valo [21]. Both empirical and numerical results showed a linear behaviour of the load with increasing speed up to moderate speed. Moreover, the authors pointed out that foil bearings tend to reach their limiting load capacity at much higher speeds than rigid bearings (*i.e.* the load plateau is reached at a much higher speed for foil bearings) leading to better performances. Furthermore, limiting solutions for high bearing numbers ($\Lambda \rightarrow \infty$) exist (see [58]), and a comparison for the load-carrying capacity has been shown for rigid and foil bearing with similar sizes. Other authors present results for foil bearings through either numerical simulations ([55, 31, 43, 29, 47]) or experimental setup [9]. The cited solutions will be used further as validation cases for the implemented numerical code.

	Reynolds Equation	BCs	Reference
Incompressible:			
1D	$\frac{\partial}{\partial x}\left(\frac{h^3}{12\mu}\frac{\partial p}{\partial x}\right) = \frac{U}{2}\frac{\partial}{\partial x}(h)$	Various	Sommerfeld [2], Cameron & Wood [3]
2D	$\frac{\partial}{\partial x}\left(\frac{h^3}{12\mu}\frac{\partial p}{\partial x}\right) + \frac{\partial}{\partial z}\left(\frac{h^3}{12\mu}\frac{\partial p}{\partial z}\right) = \frac{U}{2}\frac{\partial}{\partial x}(h)$	Various	Tao [4], Ramachandra [6], D. Sfyris et al. [40]
Compressible:			
1D	$\frac{\partial}{\partial x}\left(\frac{ph^3}{12\mu}\frac{\partial p}{\partial x}\right) = \frac{U}{2}\frac{\partial}{\partial x}(ph)$	/	/
2D	$\frac{\partial}{\partial x}\left(\frac{ph^3}{12\mu}\frac{\partial p}{\partial x}\right) + \frac{\partial}{\partial z}\left(\frac{ph^3}{12\mu}\frac{\partial p}{\partial z}\right) = \frac{U}{2}\frac{\partial}{\partial x}(ph)$	Various	J.S. Ausman [5]

Table 2.1: Known analytical solutions for Reynolds equation in journal bearing. ”Various” means that Dirichlet and Neumann BCs are used.

2.4 Dimensional Analysis

According to Buckingham Π theorem, if there are n dimensional variables in a dimensionally homogeneous equation, described by i fundamental dimensions, they may be grouped in $k = n - i$ dimensionless group. Each dimensionless group is called Π. For rigid bearings, the dimensional parameters are reported in Tab. 2.2

Bearing diameter, D	L	Rotation speed ω	s^{-1}
Radial clearance, C	L	Dynamic viscosity, μ	$\mathrm{ML}^{-1}\mathrm{T}^{-1}$
Bearing length, L	L	Reference pressure, p_a	$\mathrm{ML}^{-1}\mathrm{T}^{-2}$

Table 2.2: Rigid bearings dimensional design parameters, $F = \mathrm{f}(D, C, L\ ;\ \omega\ ;\ \mu, p_a)$.

Therefore, the number of dimensionless group Π_k is $k = n - i = 6 - 3 = 3$.

$$\begin{cases} \Pi_1 = D^{a_1} & p_a^{b_1} & \omega^{c_1} & C \\ \Pi_2 = D^{a_2} & p_a^{b_2} & \omega^{c_2} & L \\ \Pi_3 = D^{a_3} & p_a^{b_3} & \omega^{c_3} & \mu \end{cases} \Rightarrow \begin{cases} \mathrm{M}^0\mathrm{L}^0\mathrm{T}^0 = \mathrm{L}^{a_1} & (\mathrm{ML}^{-1}\mathrm{T}^{-2})^{b_1} & (\mathrm{s}^{-1})^{c_1} & \mathrm{L} \\ \mathrm{M}^0\mathrm{L}^0\mathrm{T}^0 = \mathrm{L}^{a_2} & (\mathrm{ML}^{-1}\mathrm{T}^{-2})^{b_2} & (\mathrm{s}^{-1})^{c_2} & \mathrm{L} \\ \mathrm{M}^0\mathrm{L}^0\mathrm{T}^0 = \mathrm{L}^{a_3} & (\mathrm{ML}^{-1}\mathrm{T}^{-2})^{b_3} & (\mathrm{s}^{-1})^{c_3} & \mathrm{ML}^{-1}\mathrm{T}^{-1} \end{cases}$$

This leads to

$$\Pi_1 = C/D, \qquad \Pi_2 = L/D, \qquad \Pi_3 = \mu\omega/p_a$$

The radial clearance C is fixed for a given bearing and thus one can form two dimensionless parameters as follows

$$\Pi_1' = L/D, \qquad \Pi_2' = \frac{\mu\omega}{p_a}\frac{D}{C}$$

For foil bearings, the dimensionless compliance α reflecting the bump foil stiffness will be also used as design parameter.

Chapter 3

Modelling of the Gas Foil Bearing

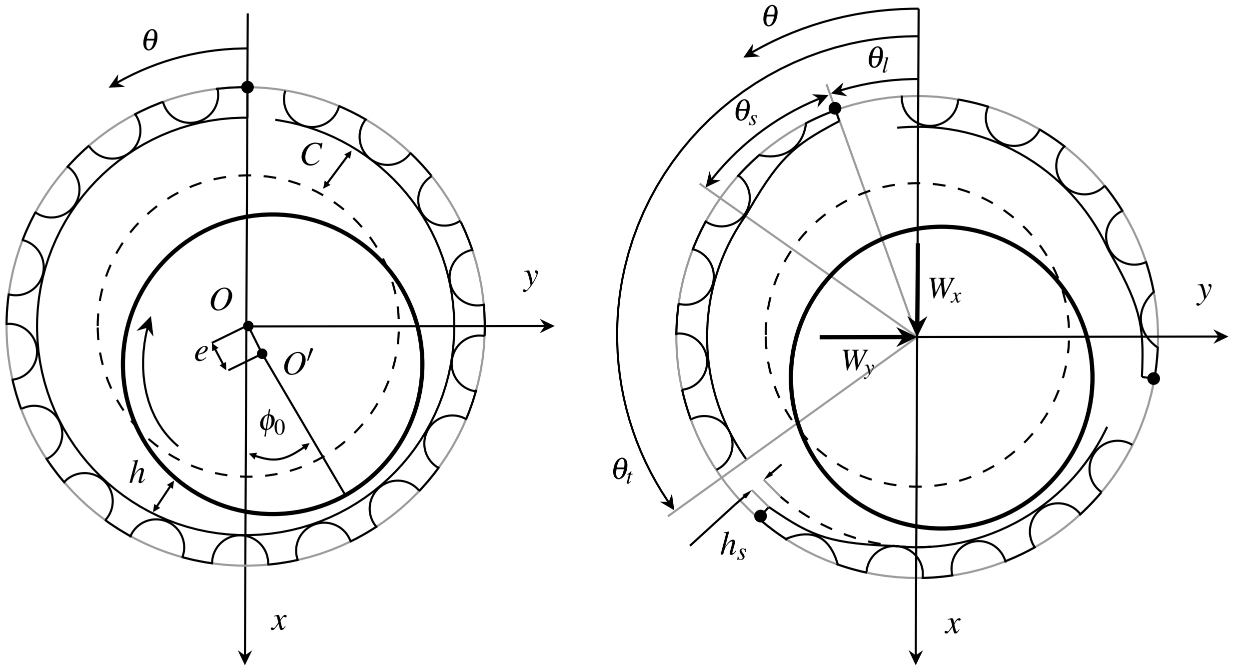

(a)

(b)

Figure 3.1: Detailed view geometry of the rigid rotor supported by foil bearing: (a) Single 360° pad and (b) Multiple pads [65].

3.1 Modelling of the Fluid Film

The pressure in each bearing can be obtained by solving the generalized steady state Reynolds equation for an isothermal, isoviscous ideal gas given by

$$\frac{\partial}{\partial x}\left(ph^3\frac{\partial p}{\partial x}\right)+\frac{\partial}{\partial z}\left(ph^3\frac{\partial p}{\partial z}\right)=6\mu\omega R\frac{\partial(ph)}{\partial x} \tag{3.1}$$

with (x, z) the circumferential and axial coordinate in the bearing plane as shown in Fig. 3.1. The variables in Eq. (3.1) can be normalized using the following substitutions

$$\theta=x/R, \qquad \tilde{z}=z/R, \qquad \tilde{p}=p/p_a, \qquad \tilde{h}=h/C, \qquad \varepsilon=e/C \tag{3.2}$$

where $\tilde{p}$, $\tilde{h}$ and ε stand respectively for dimensionless pressure, dimensionless film height and eccentricity ratio. Thus Eq. (3.1) can be rewritten in dimensionless form as

$$\frac{\partial}{\partial\theta}\left(-\tilde{p}\tilde{h}^3\frac{\partial\tilde{p}}{\partial\theta}\right)+\frac{\partial}{\partial\tilde{z}}\left(-\tilde{p}\tilde{h}^3\frac{\partial\tilde{p}}{\partial\tilde{z}}\right)+\frac{\partial(\Lambda\tilde{p}\tilde{h})}{\partial\theta}=0, \qquad \theta\in[0;2\pi], \quad \tilde{z}\in[0;L/R] \tag{3.3}$$

with Λ the bearing number defined as follows

$$\Lambda=\frac{6\mu\omega}{p_a}\left(\frac{R}{C}\right)^2 \tag{3.4}$$

This bearing number could be easily retrieved from the dimensional analysis performed in section 2.4. The form of Eq. (3.3) is suitable since the mathematical model relies exclusively on dimensionless quantities marked with "$\sim$", so that any consistent system could be applied.

As first suggested by Heshmat et al. [10], the film height $\tilde{h}$ could be divided into a rigid and compliant contribution

$$\tilde{h}=\left(\frac{h}{C}\right)=\tilde{h}_r(\varepsilon,\phi_0,\theta)+\tilde{h}_c \tag{3.5}$$

The first contribution corresponds to the film height in the undeformed, rigid bearing $\tilde{h}_r$ that depends on the shaft eccentricity ratio ε, the angular position of minimum film thickness ϕ_0 and the circumferential coordinate θ through

$$\tilde{h}_r(\varepsilon,\phi_0,\theta)=1+\varepsilon\cos(\theta-\phi_0)=1+\varepsilon_x\cos(\theta)+\varepsilon_y\sin(\theta) \tag{3.6}$$

with $(\varepsilon_x,\varepsilon_y)$ the shaft eccentricity components. While ε is always smaller than 1 for rigid bearings, foil bearings eccentricity ratio can exceed 1, while still maintaining a positive minimum film thickness. This is because as the hydrodynamic pressure deforms the top foil, it enlarges the original clearance and so allowing the shaft to move towards the minimum film thickness. For a segmented bearing with inlet slope and the nomenclature as represented in Fig. 3.1b, the film height contribution $\tilde{h}_r$ can be expressed as

$$\tilde{h}_r(\varepsilon_x,\varepsilon_y,\theta)=\begin{cases}1+\varepsilon_x\cos(\theta)+\varepsilon_y\sin(\theta)-\tilde{h}_s\left(\frac{\theta-\theta_i}{\theta_s}\right)^3, & \theta_{li}\le\theta\le\theta_i\\ 1+\varepsilon_x\cos(\theta)+\varepsilon_y\sin(\theta), & \theta_i<\theta\le\theta_{ti}\end{cases} \tag{3.7}$$

where the leading edge, inlet region and trailing edge angle of the i-th pad in a bearing with N_p pads are given by

$$\theta_{li}=\theta_l+\frac{2\pi}{N_p}(i-1), \quad \theta_i=\theta_s+\theta_l+\frac{2\pi}{N_p}(i-1) \quad \text{and} \quad \theta_{ti}=\theta_t+\frac{2\pi}{N_p}(i-1) \tag{3.8}$$

As stated by [65], the cubic inlet slope function used in Eq. (3.7) is necessary to make $\frac{\partial^2\tilde{h}_r}{\partial\theta^2}$ continuous at $\theta=\theta_i$, since Eq. 3.3 contains second order spatial derivative of $\tilde{h}$.

The compliant height $\tilde{h}_c$ can be expressed in various form, depending on the considered foil structure model. More details are given in the next section 3.2.

3.1.1 Boundary Conditions

For the fluid film boundary conditions, ambient pressure is enforced at the outer edges of the bearing and at the leading and trailing edge of each pad in the general case. In dimensionless form, this can be expressed as

$$\begin{aligned}\tilde{p}(\theta,0)=\tilde{p}(\theta,\tilde{L})&=1\\ \tilde{p}(\theta_{li},\tilde{z})=\tilde{p}(\theta_{ti},\tilde{z})&=1 \quad \text{for} \quad i=1,2,\dots,N_p\end{aligned} \tag{3.9}$$

with $\tilde{L} = L/R$ the dimensionless bearing length. By assuming the AFB to be perfectly aligned, the pressure profile is symmetric about the bearing midplane. This is exploited to reduce computational cost by only considering half of each bearing in the simulations. The simulation computational time is thus reduced by half. This implies in this case to enforce $\partial\tilde{p}/\partial\tilde{z} = 0$ at $\tilde{L}/2$ but also to multiply the resultant load by a factor of two.

Other types of boundary conditions will be used for validation purposes. Indeed, in gas bearings, sub-ambient pressure $\tilde{p} < 1$ may arise. These sub-ambient pressures can cause the top foil to separate from the bumps into a position in which the pressure on both sides of the pad are equal [54]. Heshmat et al. [10] employed the so called Gümbel conditions accounting for this separation effect. This means that the sub-ambient pressures are discarded when integrating the pressure to obtain the load components, rendering these regions inactive. Additionally, the authors use additional boundary conditions to fulfill continuity requirements. At an unknown angular position, $\tilde{p} = 1$ and $\partial\tilde{p}/\partial\theta = 0$ are enforced beyond this position in the divergent region. Note that is some case, periodic boundary conditions in the tangential direction of the flow (direction θ) are enforced for comparisons with other references data.

3.1.2 Performance Parameters

Load Carrying Capacity

Once the pressure distribution is known, the load carrying capacity, or again the force of the gas film acting on the shaft can be computed by proper integration of the fluid film pressure over the bearing surface

$$\left\{ \begin{array}{c} \tilde{W}_x \\ \tilde{W}_y \end{array} \right\} = \int_0^{\tilde{L}} \int_0^{2\pi} (\tilde{p} - 1) \left\{ \begin{array}{c} -\cos\theta \\ \sin\theta \end{array} \right\} d\theta d\tilde{z} \tag{3.10}$$

with $\tilde{L} = L/R$ the dimensionless bearing length and θ and $\tilde{z}$ the dimensionless circumferential and axial coordinate. The total/resultant nondimensional load $\tilde{W}$ and the load angle ϕ_L are therefore given by

$$\tilde{W} = \frac{W}{p_a R^2} = \sqrt{\tilde{W}_x^2 + \tilde{W}_y^2}, \qquad \Phi_L = \tan^{-1}(\tilde{W}_y/\tilde{W}_x) \tag{3.11}$$

Energy dissipation

An important feature of AFBs is the energy dissipation due to sliding friction in their foil structures. Indeed, one of the main problems in rotating machinery concerns the operating point stability. GFBs rotor systems tend to become unstable at higher rotational speeds due to highly nonlinear bearing forces caused by pressurized fluid [17, 37]. Consequently, oscillations with relatively large amplitudes may result in undesirable self-excitation vibrations [46, 51]. For these reasons, AFBs are preferred over rigid conventional bearings due to their design foil structure, which, once in contact with the working fluid, leads to energy dissipation via sliding friction mechanism [16, 15]. This reduces the amplitudes of the vibrations, thereby preventing the occurrence of self-excited rotor vibrations [59].

In this context, Larsen et al. [48] presented a theoretical and experimental analysis based on a two-dimensional quasi-static FE model, including geometrical non-linearities and Coulomb friction and neglecting foil mass. The Coulomb friction forces are modelled based on equivalent nonlinear springs located in the contact points between the bump foils and the contact surfaces. Good agreement with experimental results was observed at low frequencies. Other publishers have developed friction models to approximate the sign function in Coulomb friction law [24, 57]. In the present work, the frictional considerations are considered through the structural stiffness. Irodanoff model, presented in the next section, uses friction coefficient μ_f that characterizes friction between the fluid and the structural foil. The effect of the friction coefficients on the stiffness and load-carrying capacity will be discussed later.

Viscosity

As far as hydrodynamic lubrication is concerned, viscosity comes to play the most critical property. In general, the viscosity of a fluid is governed by the combined effect of intermolecular forces and momentum transfer. For gas, momentum transfer is the dominant factor [58, 35] and thus a rise in temperature leads to an increase in momentum transfer and hence viscosity tends to increase. Most publishers derived the Reynolds equation under the assumption of constant viscosity in the fluid film. In this present work, the same assumption is maintained and the Sutherland formula is used to determine the working gas dynamic viscosity as a function of the operating temperature

$$\mu = \mu_0 \left(\frac{T}{T_0}\right)^{3/2} \left(\frac{T_0 + C_s}{T + C_s}\right) \tag{3.12}$$

with μ and μ_0 the dynamic and reference viscosity, T and T_0 the operating and reference temperature and C_s the Sutherland's constant. Note that Eq. (3.12) is valid for single-component gases operating at a wide range of temperature [44]. It does, however, work well for air because air is mainly composed of nitrogen and oxygen, which have very similar properties. For air, it comes

$$\mu_0 = 1.715\,.\,10^{-5}\ \mathrm{N.s/m^2}, \qquad T_0 = 273.15\ \mathrm{K}, \qquad C_s = 110.4\ \mathrm{K} \tag{3.13}$$

Parameters values for other common gases can be found in [26].

Since the foil bearing used by Mitis SA is located at different positions in the machine (depending on the turbogenerator configuration), the effect of operating temperature/viscosity on pressure and load capacity will be shown in the last chapter.

3.2 Modelling of the Foil Structure

The compliant height term $\tilde{h}_c$ of Eq. (3.5) can be expressed using a variety of foil structural models. The compliant foil structure is typically composed of a corrugated bump strip (Young's modulus E_b, Poisson ratio ν_b, thickness t_b, density ρ_b) topped by a thin smooth foil, called top foil (Young's modulus E_t, Poisson ratio ν_t, thickness t_t, density ρ_t). Both bumps foil and top foil are welded to the bearing housing at one end and are free at the other end, as can be seen in Fig. 3.2a.

The first theoretical model of a single bump stiffness was proposed by Wallowit and Anno and used in the original work of Heshmat et al. [10]. This model assuming zero friction coefficient was used by most publishers ([55, 43, 23, 61]) for its simplicity. The model consists of representing the foil structure as a simple elastic foundation with the following assumptions: (1) the stiffness of the foil is taken to be uniformly distributed through the bearing surface (uniform elastic foundation) and is constant and independent of the amount of bump deflection, (2) The top foil does not sag between adjacent bumps and does not have either bending or membrane stiffness, and its deflection follows that of the bump that only depends on local effect, (3) The fluid in the film is isothermal and behaves like a gas perfect. With these considerations, the compliant height term $\tilde{h}_c$ can be expressed as

$$\tilde{h}_c = \alpha(\tilde{p} - 1) \tag{3.14}$$

with

$$K_W = \left(\frac{\alpha_W C}{p_a}\right), \qquad \alpha_W = \frac{2 p_a S_b}{CE}\left(\frac{l_b}{t_b}\right)^3 \left(1 - \nu_b^2\right) \tag{3.15}$$

K_W is the bump structural stiffness, and α_w is the bearing compliance. The sub-index ”W” is for Wallowit. Ku and Heshmat [13] then presented a more elaborated model of a complete corrugated foil strip layer in

1993. This model uses shell theory and considers friction between bump foils and the housing or the top foil, local interaction forces variable load distributions and bump geometries [13].

A second formulation for the single bump rigidity was given by Iordanoff [20]. This model considers frictional effects between the bumps foil and the bearing housing and uses different boundary conditions for the welded and free end bump. In this model, the bump material is assumed to be isotropic, and the bump pitch is constant for all the bumps. The interaction between bumps is also neglected, as is the case for the Wallowit and Anno formula. The bearing compliance for a welded (fixed-free) α_I^{fw} and free (free-free) α_I^{ff} end are given by

$$\alpha_I^{fw} = \frac{12p_a S_b J\left(\theta_b, \mu_f\right)}{EC\sin^3(\theta_b)} \left(\frac{l_b}{t_b}\right)^3 \left(1-\nu_b^2\right), \qquad \alpha_I^{ff} = \frac{6p_a S_b I\left(\theta_b, \mu_f\right)}{EC\sin^3(\theta_b)} \left(\frac{l_b}{t_b}\right)^3 \left(1-\nu_b^2\right) \tag{3.16}$$

where $I(\mu_f, \theta_b)$ and $J(\mu_f, \theta_b)$ are functions depending of bump geometrical parameters (see Appendix B). This model is widely known and has been used by [31] and [29] in their analysis. The models mentioned above do not take into account the effect of the top foil model and compute the structural stiffness based on the bump foil. In this context, Larsen and Santos [53] extended the Wallowit and Anno expression to include the top foil sagging effect that may modify the global foil stiffness. Such a phenomenon occurs when the pressure causes a deflection of the top foil between two bumps (see Fig. 3.2b). The authors developed a periodic expression (see Eq. (3.17)) based on basic beam theory to approximate the sagging effect analytically and then integrate it into the rigidity formula originally provided by Wallowit and Anno. This last makes numerical implementation straightforward compared to the reference analytical model presented in [32]. However, this formula is only applicable for periodic bump foil distributions; thus, in the presence of inlet slope, this formula is no more valid. Note that in the following, two notations, α a,d S will be used for the compliance factor or again bearing compliance.

$$\alpha_L(\tilde{\theta}) \approx \frac{p_a s_b^4\left(1-\nu^2\right)}{ECt_{\mathrm{t}}^3}\left(\frac{1}{60}-\frac{3}{2\pi^4}\cos\left(\frac{2\pi\tilde{\theta}}{S_b}\right)\right)+\frac{2p_a S_b}{CE}\left(\frac{l_0}{t_b}\right)^3\left(1-\nu^2\right), \quad \tilde{\theta}\in[0;S_b] \tag{3.17}$$

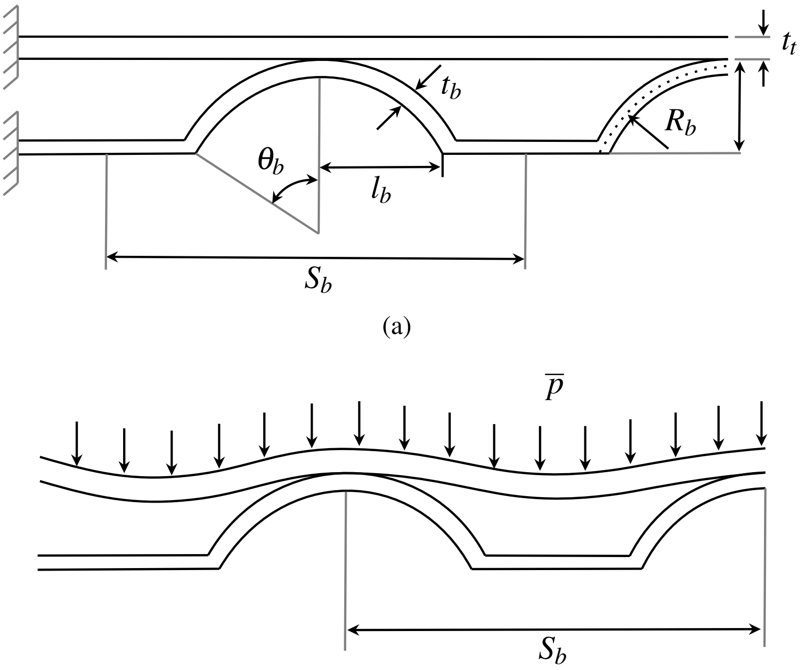

(a)

(b)

Figure 3.2: Detailed view of the bump structure: (a) geometrical parameters and (b) top foil sagging.

NUMERICAL METHODS

Chapter 4

Discontinuous Galerkin Finite Element Method

This chapter presents the theoretical background of the Discontinuous Galerkin Finite Element Method (DGFEM) and its application to the gas film lubrication equation. This finite element method combines discontinuous interpolation with a Galerkin variational formulation. In contrast to most FE methods, which require that the solution be at least continuous across elements, DG-FEM has a broken trial space property. The solution is fully regular inside the element, but not necessarily continuous across elements (See Fig. 4.1). Each element communicates information to the other through numerical fluxes.

Since 1973, the current method has been developed in a vast domain of application [39] and started being applied more frequently over the recent years, more precisely in the frame of transport on neutrons [8] and computational fluid dynamic [39]. Indeed, DG has the following main advantages over classical FV and FD methods [42, 39]:

- DG method allows for obtaining high order of accuracy in terms of interpolation and spectral properties on unstructured meshes without opting for large stencils.
- The lack of continuity constraint/restriction, typical for FE method, introduces additional easiness and flexibility in the choice of local interpolation order (*i.e.* degree of approximation polynomial change from one element to another) and shape functions.
- DG methods are very well suited for handling complex geometries and require a straightforward treatment of the boundary conditions, making it attractive for multi-physics problems.
- DG method demonstrates better accuracy than FV method and better stability than FE method, at least for convective problems [68]

The chapter is organized as follows. First, the DG method in presented in a general way and applied to a general conservative system. This part will be inspired by [42]. Then, the discretization is applied to the Reynolds equation. Numerical fluxes and source terms are then identified and discussed. Finally, a brief description of the solver ”ForDGe” developed at ULiège and used in the frame of this work is given.

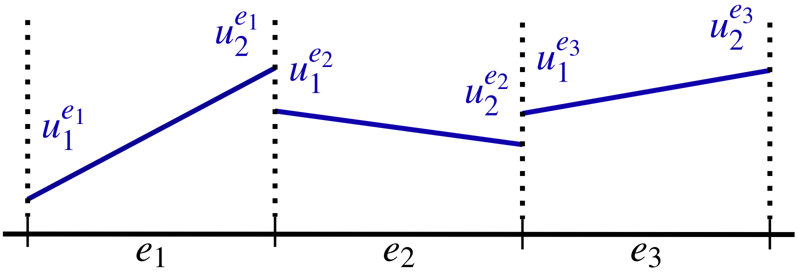

Figure 4.1: Simplifying schematics of a solution $\boldsymbol{u}$ across element for the DG method with shape function of order 1 [68]

4.1 Application to Conservative System

Let us consider the general conservative system of partial differential equations [42]

$$\partial_t \boldsymbol{u}(\boldsymbol{r},t) + \nabla\cdot\boldsymbol{F}(\boldsymbol{u},\boldsymbol{r},t) + \nabla\cdot\boldsymbol{D}(\boldsymbol{u},\nabla\boldsymbol{u},\boldsymbol{r},t) = \boldsymbol{S}(\boldsymbol{u},\nabla\boldsymbol{u}), \quad \boldsymbol{r}\in\Omega,\ t\in\mathbb{R}^+ \tag{4.1}$$

with $\boldsymbol{r}$ the position vector defined on domain Ω, t the temporal variable, $\boldsymbol{u}$ the state vector of conserved variables, $\boldsymbol{F}$ the convective flux vector only dependant on the solution, $\boldsymbol{D}$ the diffusive flux vector that depends on the solution as well as its gradients and $\boldsymbol{S}$ the source or reaction term vector regrouping all the terms that can not be expressed as fluxes.

Moreover, a linear diffusive flux $\boldsymbol{D}$ can be expressed in index notation (Einstein notation, *i.e.* summation occurs on repeated indices) [42]

$$D_m^k = -\mathscr{D}_{kl}^{mn}\frac{\partial u_n}{\partial x^l} \tag{4.2}$$

with $\mathscr{D}$ the Jacobian of the diffusive flux $\boldsymbol{D}$ with respect to the solution gradients, m and n are indices for variables and k and l are indices for coordinate directions.

4.1.1 Galerkin Variational Form

In order to obtain a general form of the Galerkin variational formulation, a generic flux $\boldsymbol{H}=\boldsymbol{F}+\boldsymbol{D}$ is considered so that Eq. (4.1) is rewritten as:

$$\partial_t \boldsymbol{u}(\boldsymbol{r},t) + \nabla\cdot\boldsymbol{H}(\boldsymbol{u},\nabla\boldsymbol{u},\boldsymbol{r},t) = \boldsymbol{S}(\boldsymbol{u},\nabla\boldsymbol{u}), \quad \boldsymbol{r}\in\Omega, t\in\mathbb{R}^+ \tag{4.3}$$

A weak form of Eq. (4.3) can be obtained by multiplying all terms by ϕ, $\forall\phi\in\mathscr{V}$, with $\mathscr{V}$ functional space and integrating over the whole domain Ω

$$\int_\Omega \phi\,\partial_t\boldsymbol{u}\,d\Omega + \int_\Omega \phi\nabla\cdot\boldsymbol{H}\,d\Omega = \int_\Omega \phi\boldsymbol{S}\,d\Omega, \quad \phi\in\mathscr{V} \tag{4.4}$$

The Galerkin variational form can then be rewritten, using an elementwise decomposition. Each integral is evaluated as the sum of of the integrals over all the elements. On each element e, the integrands consists of fully regular functions so that the integration by parts can be performed

$$\sum_e\int_e \phi\left(\partial_t\boldsymbol{u}-\boldsymbol{S}\right)d\Omega + \sum_e\int_e \phi\nabla\cdot\boldsymbol{H}\,d\Omega = 0 \tag{4.5}$$

$$\sum_e\int_e \phi\left(\partial_t\boldsymbol{u}-\boldsymbol{S}\right)d\Omega - \sum_e\left(\int_e \nabla\phi\cdot\boldsymbol{H}\,d\Omega + \int_{\partial e}\phi\boldsymbol{H}\cdot\boldsymbol{n}\,dS\right) = 0 \tag{4.6}$$

with $\boldsymbol{n}$ the normal of the face boundary, pointing outward of the element. The boundary ∂e is in fact the union of the faces f of the element, *i.e.* $\partial e = \bigcup_f I_f$, with I_f the interfaces between two elements or between an element and the domain boundary

$$\sum_e\int_e \phi\left(\partial_t\boldsymbol{u}-\boldsymbol{S}\right)d\Omega - \sum_e\int_e \nabla\phi\cdot\boldsymbol{H}\,d\Omega + \sum_{f\in\partial e}\int_f \phi\boldsymbol{H}\cdot\boldsymbol{n}\,dS = 0 \tag{4.7}$$

The last term in Eq. (4.7) can be rewritten by considering the sum on all the element interfaces f

$$\begin{aligned}\sum_e\int_{\partial e}\phi\boldsymbol{H}\cdot\boldsymbol{n}\,dS &= \sum_{f\in\partial e}\int_f \phi\boldsymbol{H}\cdot\boldsymbol{n}\,dS \\ &= \sum_f\int_f \left(\phi^+\boldsymbol{H}^+ + \phi^-\boldsymbol{H}^-\right)\cdot\boldsymbol{n}\,dS \\ &= \sum_f\int_f \left(\phi^+\boldsymbol{H}^+\cdot\boldsymbol{n}^+ + \phi^-\boldsymbol{H}^-\cdot\boldsymbol{n}^-\right)dS\end{aligned} \tag{4.8}$$

The $+$ and $-$ are to distinguish the values of the discontinuous quantities/solutions at both side of the interface, depending on the element from which the interface is approached. As it is shown in Fig. 4.2, the $+$ sign corresponds to the elements whose external normal corresponds to that of the oriented face, while the $-$ sign corresponds to the other (*i.e.* $\boldsymbol{n}^+ = \boldsymbol{n}$ and $\boldsymbol{n}^- = -\boldsymbol{n}$).

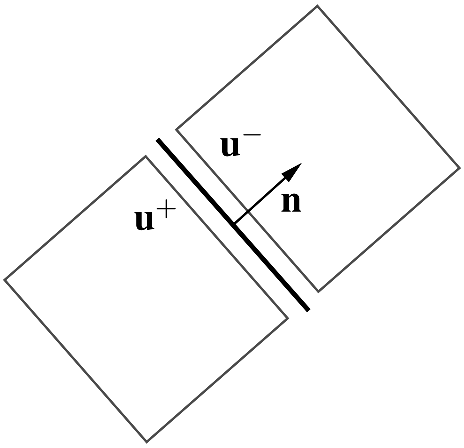

Figure 4.2: Convention for suffixes $+$ and $-$ of the solution when approaching the interface. The interface boundary is represented by the thick black line as well as its normal [42].

By defining the jump $[[\cdot]]$ and the average operator $\langle\cdot\rangle$ available in Appendix C, we can write

$$\begin{aligned}\sum_e \int_{\partial e} \phi \boldsymbol{H} \cdot \boldsymbol{n}\, dS &= \sum_f \int_f [[\phi \boldsymbol{H}]]\, dS \\ &= \sum_f \int_f \left([[\phi]] \langle \boldsymbol{H} \rangle + \langle \phi \rangle [[\boldsymbol{H}]]\right) dS\end{aligned} \tag{4.9}$$

The term in Eq. 4.9 can be replaced by a suitable interface flux functions γ such that the general Galerkin variational formulation is given by

$$\sum_e \int_e \phi\, (\partial_t \boldsymbol{u} - \boldsymbol{S})\, d\Omega - \sum_e \int_e \nabla\phi \cdot \boldsymbol{H}\, d\Omega + \sum_f \int_f \gamma\left(\boldsymbol{u}^+, \boldsymbol{u}^-, \phi^+, \phi^-, \boldsymbol{n}\right) dS = 0, \quad \phi \in \mathscr{V} \tag{4.10}$$

where the first term accounts for the temporal variation of the elemental solution and its source term $\boldsymbol{S}$, the second term corresponds to the element's volume flux $\boldsymbol{H}$ and the last one to the interface flux γ. A particular attention will be given to this last term in the following subsections, since its formulation/expression depends on the system to be considered, either hyperbolic or elliptic.

4.1.2 Convective Variational Form

It was found that by selecting an approximate Riemann solver $\boldsymbol{F}^*$ for γ, the discretisation of the convective parts of Eq. 4.10 is always stabilized [42, 41]. Then the interface flux writes

$$\gamma^{\boldsymbol{F}}\left(\boldsymbol{u}^+, \boldsymbol{u}^-, \phi^+, \phi^-, n\right) = \phi^+ \boldsymbol{F}^*\left(\boldsymbol{u}^+, \boldsymbol{u}^-, \boldsymbol{n}\right) \tag{4.11}$$

This choice satisfies all of the requirements for a stable and convergent numerical method [42, 36, 66]:

Consistency The numerical flux is consistent if the residual of Eq. (4.12) evaluated at the actual solution $\tilde{\boldsymbol{u}}$ is zero

$$V_e \partial_t \boldsymbol{u} = -\sum_{f \cap e \neq \emptyset} \int_f \boldsymbol{F}^*\left(\boldsymbol{u}^+, \boldsymbol{u}^-, \boldsymbol{n}\right) dS \tag{4.12}$$

This require the solution on both side of the interface to be the same

$$\boldsymbol{F}^*(\boldsymbol{u},\boldsymbol{u},\boldsymbol{n}) = \mathbf{f}(\boldsymbol{u})\cdot\boldsymbol{n} \tag{4.13}$$

For sake of simplicity, one assume in Eq. (4.12) that the normal on the face f is pointing outward of the cell e into cell e'.

Conservativity The conservation principle is retrieved at the discrete level, since the discretization describes conservation of quantities. This is translated by the fact that the numerical flux should be the same for two elements sharing the same interface, but of opposite sign (See Fig. 4.2 for used convention)

$$\boldsymbol{F}^*\left(\boldsymbol{u}^+,\boldsymbol{u}^-,\boldsymbol{n}\right) = -\boldsymbol{F}^*\left(\boldsymbol{u}^-,\boldsymbol{u}^+,-\boldsymbol{n}\right) \tag{4.14}$$

The flux leaving the element through a face is thus completely recuperated by its neighbour.

Stability Stability is required to ensure the convergence of the numerical method. Numerical flux should thus be chosen so that a bounded norm of the solution is retrieved after discretization. Different notion of stability exist and one of them is the non linear entropy stability. A numerical flux $\boldsymbol{F}^*$ is entropy stable if [36],

$$\boldsymbol{v}\in[\boldsymbol{u}^-,\boldsymbol{u}^+], \quad \text{with } [\boldsymbol{u}^-,\boldsymbol{u}^+] := \left\{\theta\boldsymbol{u}^- + (1-\theta)\boldsymbol{u}^+\right\}, \quad \theta\in[0,1] \tag{4.15}$$

one has

$$\left(\boldsymbol{F}^*\left(\boldsymbol{u}^-,\boldsymbol{u}^+,\boldsymbol{n}\right) - \boldsymbol{f}(\boldsymbol{v})\right)\left(\boldsymbol{u}^+ - \boldsymbol{u}^-\right) \geq 0 \tag{4.16}$$

This stability criterion guarantees the entropy of the system to not grow. Since the mathematical interpretation of the entropy corresponds to an energy of the solution, it must decrease with time or at least remains a constant [66, 36, 64].

4.1.3 Diffusive Variational Form

An *Interior Penalty Method (IP)* is used for the discretization of the diffusive/viscous term in Eq. (4.1). The main reason of choosing such a method is its complicity. Indeed, the evaluation of the residual is only based upon direct neighbours of the element, thus simplifying the structure as well as evaluation of the Jacobian [42] [1]. However, IP method depends on a tunable, seemingly arbitrary parameter. Adequate and sufficiently strict values for this parameter have been presented in Hilleweart doctoral thesis [42].

IP methods can be build starting from the reinterpretation of the DGM as element wise FEM problems, coupled by internal boundary conditions. It seeks to resolve the problem continuously across boundaries by imposing Dirichlet condition on the boundaries of neighbouring elements. Let consider a simple linear elliptic problem on unidimensional domain Ω with Dirichlet boundary conditions on $\partial\Omega$

$$\begin{aligned} \partial_t u + \nabla\cdot(-\mathbf{D}\cdot\nabla u) &= 0, \quad \forall x\in\Omega \\ u &= u^*, \quad \forall x\in\partial\Omega \end{aligned} \tag{4.17}$$

for which an approximate finite element solution $\tilde{u}\in\Omega$ is sought using the below Galerkin variational formulation:

$$\int_\Omega \phi\,(\partial_t\tilde{u})\,d\Omega - \int_{\partial\Omega}\nabla\phi\cdot(\mathbf{D}\cdot\nabla\tilde{u})\,d\Omega - \int_{\partial\Omega}\phi\,(\mathbf{D}\cdot\nabla\tilde{u})\cdot\boldsymbol{n}\,dS = 0, \quad \phi\in\mathscr{V} \tag{4.18}$$

A common and standard approach would be to impose strong boundary conditions, hence imposing the value of solution $\tilde{u}$ at the domain boundary $\partial\Omega$. Such approach is relatively simple, easy to implement and

---

[1] Other alternative scheme (developed by Bassi and Rebay) providing the same capacity as the above cited method, but with an additional complexity for the interface term implementation, especially for systems.

has the intuitive advantage to use the exact solution at those locations, where it is a priori known. However, this may be not very appropriate in case the boundary condition data are noisy, as it can be clearly seen in Fig. 4.3. One would rather prefer an approach, similar to the behavior of the green line in Fig. 4.3 that minimises the average interpolation error between $\tilde{u}$ and u^*. This way of imposing boundary conditions is called weak imposition.

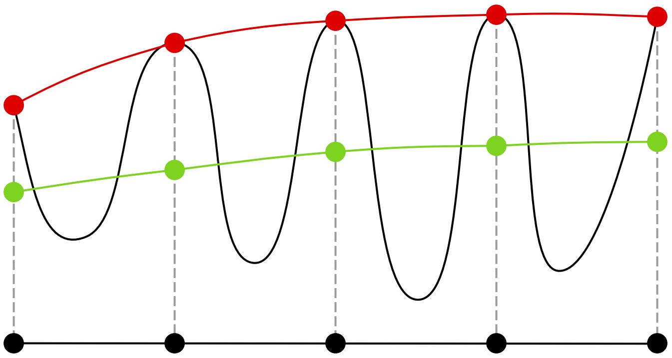

Figure 4.3: Strong (red) and weak imposition (green) of Dirichlet boundary conditions. The strong imposition may lead to large error and potentially very rapidly varying values. The weak imposition is preferred since it results in a much smoother values with a lower global error [42].

Concretely, the main idea is then to penalise the difference $\tilde{u} - u^*$ between the desired and actual solution by adding an additional variational term DP (*Galerking penalty term*) to the variational formulation equation (Eq. (4.18))

$$\begin{aligned}\int_{\Omega} \phi\,(\partial_t \tilde{u})\,d\Omega + \int_{\partial\Omega} \nabla\phi \cdot (\mathbf{D} \cdot \nabla\tilde{u})\,d\Omega - \underbrace{\int_{\partial\Omega} \sigma\phi\,(\tilde{u} - u^*)\,dS}_{DP} \\ - \underbrace{\int_{\partial\Omega} \phi \mathbf{D} \nabla\tilde{u} \cdot \boldsymbol{n}\,dS}_{DD} - \theta \underbrace{\int_{\partial\Omega} (\tilde{u} - u^*)\,\mathbf{D}\nabla\phi \cdot \boldsymbol{n}\,dS}_{DT} = 0\end{aligned} \tag{4.19}$$

with σ the penalty parameter chosen so that the positive contribution of the penalty term dominates the boundary flux term $DD + DT$, that is not consistently positive. The stability of interior penalty method is thus governed by this penalty parameter σ, which has to be higher than a certain critical value. However, the choice for θ is arbitrary. Typical three values exist

- $\theta = 0$ one retrieve the *Incomplete Interior Penalty Method (IIPM)* which is simple but rarely used in practice.
- $\theta = 1$ corresponds to the *Symmetric Interior Penalty Method (SIPM)* which has optimal convergence properties.
- $\theta = -1$ corresponds to the *Non-symmetric Interior Penalty Method (NIPM)*. By using this method, the destabilizing effect of interface terms is eliminated, and hence only requires strictly positive penalty parameter.

Therefore, the interface flux for the system in Eq. 4.17 can be written using jump and mean operators as

$$\gamma_{IPM}\left(u^+, u^-, \phi^+, \phi^-, \boldsymbol{n}\right) = \sigma[[\phi]] \cdot [[\tilde{u}]] + [[\phi]] \cdot \langle \mathbf{D} \cdot \nabla\tilde{u} \rangle + \theta[[\tilde{u}]] \cdot \langle \mathbf{D} \cdot \nabla\phi \rangle \tag{4.20}$$

4.1.4 Shape Functions

Let us consider a set of function $C^0_\infty(\Omega)$ on an element e and whose support is this element, and φ_i set of linearly independent basis function of $C^0_\infty(e)$ (called *shape functions*). The variational formulation (Eq. (4.10)) is then valid

$$\sum_e \int_e \varphi_i \left(\partial_t \boldsymbol{u} - \boldsymbol{S}\right) d\Omega - \sum_e \int_e \nabla\varphi_i \cdot \boldsymbol{H}\, d\Omega + \sum_f \int_f \gamma\left(\boldsymbol{u}^+, \boldsymbol{u}^-, \varphi_i^+, \varphi_i^-, \boldsymbol{n}\right) dS = 0 \tag{4.21}$$

since it only needs to be tested with respect to the shape functions. Since continuity between elements is not required, only the choice of shape functions that are supported on a single element is considered. Note that in the case where the shape functions are of order zero, one retrieve the FVM formulation. The basis functions φ_i chosen here are Lagrange polynomials based on either equidistant or Gauss-Lobatto-Legendre (GLL) control points. The main advantage is that on a face element, only shape functions corresponding to interpolation points on the corresponding face are non null, thereby significantly reducing the computational work for the integration of the interface terms [42]. In one space dimension and for a set of distinct points $\{x_i\}_{0\le i\le n}$ the Lagrange polynomial takes 1 at x_i and 0 at x_j, $j \neq i$ as follows [36]

$$\varphi_i(x) = \prod_{j\in\{0,\dots,n\}\setminus\{i\}} \frac{\left(x - x_j\right)}{\left(x_i - x_j\right)}, \quad \forall i \in \{0,\dots,n\} \tag{4.22}$$

Fig. 4.4 shows Lagrange polynomials for order 6 with both kind of control points. In the frame of this work, GLL quadrature points are chosen, as they found to provide an optimal set of interpolation points for higher orders of interpolation.

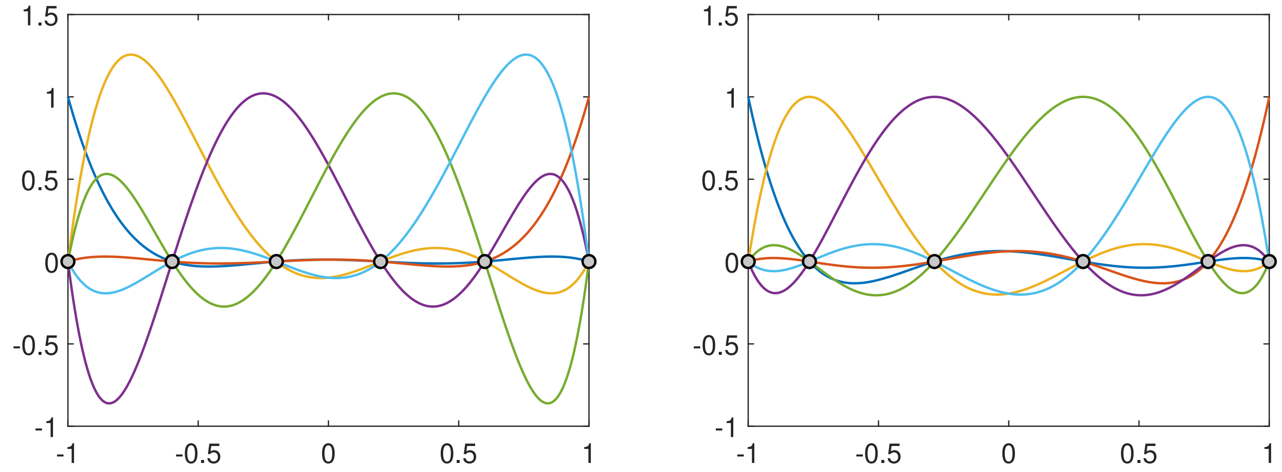

(a) Equispaced points

(b) Gauss-Lobatto-Legendre (GLL) points

Figure 4.4: Legendre interpolation polynomials on the reference interval $[-1;1]$ based on 6 (a) Equidistant points, (b) Gauss-Lobatto-Legendre (GLL) points. The controls points are represented by the grey dots.

With these considerations, the approximate solution in a given element can be expressed

$$\boldsymbol{u}_h^e(x) \equiv \sum_{j=1}^{N} \boldsymbol{u}_j^e \varphi_j^e(x) \tag{4.23}$$

where the index h to emphasise the difference between the approximated and true solution. The flux and the source terms are then computed based on this approximated solution and its gradient (*i.e.* $\boldsymbol{F}(\boldsymbol{u}_h)$,

$\boldsymbol{D}(\boldsymbol{u}_h, \nabla \boldsymbol{u}_h)$, $\boldsymbol{S}(\boldsymbol{u}_h, \nabla \boldsymbol{u}_h)$). Finally, Eq. (4.21) writes

$$\begin{aligned} \sum_e \int_e \varphi_i \varphi_j \partial_t \boldsymbol{u}_j d\Omega - \sum_e \int_e \partial_x \varphi_i \cdot \boldsymbol{H}_h d\Omega + \sum_e \int_e \varphi_i \boldsymbol{S}_h d\Omega \\ + \sum_f \int_f \gamma\left(\boldsymbol{u}^+, \boldsymbol{u}^-, \varphi_i^+, \varphi_i^-, \boldsymbol{n}\right) dS = 0 \end{aligned} \tag{4.24}$$

Since this expression is valid on the element level, one retrieve the semi discrete equation

$$\boldsymbol{M}_{ij} \partial_t \boldsymbol{u}_j^e = \boldsymbol{L}_i \tag{4.25}$$

with the mass matrix $\boldsymbol{M}_{ij}$ and residual $\boldsymbol{L}_i$ given by

$$\boldsymbol{M}_{ij} = \int_e \varphi_i \varphi_j d\Omega \tag{4.26}$$

$$\boldsymbol{L}_i = \sum_e \int_e \partial_x \varphi_i \cdot \boldsymbol{H}_h d\Omega - \sum_e \int_e \varphi_i \boldsymbol{S}_h d\Omega - \sum_f \int_f \gamma\left(\boldsymbol{u}^+, \boldsymbol{u}^-, \varphi_i^+, \varphi_i^-, \boldsymbol{n}\right) dS \tag{4.27}$$

with e the element on which φ_i and φ_j are defined and $\boldsymbol{L}_i$ the residual associated to the shape function φ_i. Note that Eq. (4.32) can be reformulated as a set of ODEs for each of the unknowns, and thus can be solved by exact inversion.

4.1.5 Resolution technique

The semi discrete equation (Eq. (4.32)) reduces for steady-state problem to

$$\boldsymbol{L}(\boldsymbol{u}) = 0 \tag{4.28}$$

since the solution does not vary with time and thus the left hand side of Eq. (4.32) drops. For non-linear system, classical Newton-Raphson approach can be used. Expanding $\boldsymbol{L}$ using a Taylor expansion around a certain value $\boldsymbol{u}_0$ (*initial guess vector*) yields

$$\begin{aligned} \boldsymbol{L}(\boldsymbol{u}) \simeq \boldsymbol{L}(\boldsymbol{u}_0) + \left.\frac{\partial \boldsymbol{L}}{\partial \boldsymbol{u}}\right|_{\boldsymbol{u}_0} (\boldsymbol{u} - \boldsymbol{u}_0) = 0 \\ \boldsymbol{u} = -\left(\left.\frac{\partial \boldsymbol{L}}{\partial \boldsymbol{u}}\right|_{\boldsymbol{u}_0} \right)^{-1} \boldsymbol{L}(\boldsymbol{u}_0) + \boldsymbol{u}_0 \end{aligned} \tag{4.29}$$

where the derivative $\left.\frac{\partial L}{\partial u}\right|_{\boldsymbol{u}_0}$ is the Jacobian. The method uses initial guess $\boldsymbol{u}_0$ and iterate until the convergence rate between two successive stages j and $j+1$ is below a given tolerance. The inverse of Jacobian matrix as well as the residual are evaluated/computed at each iteration (guess). The residual associated to the shape function φ_i is given in Eq. (4.27). Its calculation requires the fluxes and the source term to be found. This is done in an efficient way in three steps:

1. `Collocation` the interpretation of the variables and their parametric gradients from interpolation points to quadrature rule.
2. `Flux computation` the computation of the volume flux and interface flux at quadrature rule
3. `Integration & redistribution` the return from quadrature points to interpolation points.

More information about the residual assembly are available in [42]. Note that in order to compute the Jacobian of the residual, the Jacobian of each term of Eq. (4.27) has to be computed.

As previously mentioned, the next iteration of the Newton-Raphson method requires the evaluation of the residual and its inverse of Jacobian at the previous guess. The inverse of the Jacobian could be found using direct solver. This last is based upon the LU factorization technique (*i.e.* $\mathscr{A} = \mathscr{L}\mathscr{U}$) where the factor matrices are lower and upper triangular to allow their efficient inversion. Note that more storage is required for $\mathscr{L}$ and $\mathscr{U}$ than for $\mathscr{A}$ if the initial matrix $\mathscr{A}$ is not compactly represented near its diagonal. In this case, the factors matrices will be significantly filled in; thus, more storage is required [27]. This is less of problem since the current problem remains small. Memory usage becomes a significant concern as problems grow in size, which is the case for most encountered problems. One solution could be reordering/renumbering the matrix $\mathscr{A}$ to minimize the matrix bandwidth. Another alternative could be to consider Krylov subspace alternative methods. Such iterative methods should generally be considered for large sparse problems with excessive memory requirements. In this work, the problem stencil remains small and then direct solver is used for the resolution of the linear part (*i.e.* inversion of the Jacobian).

4.2 Application to the Reynolds Equation

In this section, the application of the DG method to the current Reynolds equation is presented. More precisely, the numerical fluxes as well as the source terms are identified/constructed for each case ($1D$, $2D$, incompressible, compessible) following the conventions used in Eq. (4.1).

4.2.1 Discretized Reynolds Equation

It is convenient, especially when utilizing the FE or FV method, to rewrite the steady-state compressible Reynolds equation into vector form as

$$\nabla \cdot \left(-\tilde{p}\tilde{h}^3 \nabla \tilde{p}\right) + \nabla \cdot (\tilde{p}\tilde{h})\, \mathbf{s} = 0 \tag{4.30}$$

where $\mathbf{s} = \{\Lambda, 0\}$ is the advection vector, $\Lambda = 6\mu\omega/p_a(R/C)^2$ is the compressibility/bearing number, and $\tilde{h}$ the dimensionless film thickness given by

$$\tilde{h} = \tilde{h}_r(\varepsilon, \phi_0, \theta) + \tilde{h}_c(\tilde{p}) \tag{4.31}$$

with the compliant height $\tilde{h}_c$ only to be considered for foil bearings. With these considerations and following the convention used in Eq. (4.1) one have

$$\boldsymbol{u} = \tilde{p}, \qquad \boldsymbol{F} = \tilde{p}\tilde{h}\,\mathbf{s}, \qquad \boldsymbol{D} = -\tilde{p}\tilde{h}^3\nabla\tilde{p}, \qquad \boldsymbol{S} = \mathbf{0} \tag{4.32}$$

Note that $\boldsymbol{F}, \boldsymbol{D}$ and $\boldsymbol{S}$ are expressed for the two directions θ and $\tilde{z}$. In the following, the DGM is applied to the two-dimensional Reynolds equation for compressible fluid. The numerical fluxes and source term are then computed.

4.2.2 Numerical Fluxes

The numerical fluxes $\boldsymbol{F}^*$ used for this work is the upwind flux.The system of equation as it appears in Eq. (4.30) include a linear advection term with a constant velocity Λ that does not depend on the solution. The solution should be in theory displaced in space at this constant speed. The upwind scheme uses this theoretical solution to evaluate the numerical flux as follows

$$\begin{aligned} \boldsymbol{F}^*(\boldsymbol{u}_L, \boldsymbol{u}_R, \boldsymbol{n}) &= \boldsymbol{F}(\boldsymbol{u}_L) = (\Lambda \cdot \boldsymbol{n})\, \tilde{h}(\boldsymbol{u}_L)\, \boldsymbol{u}_L, \qquad \Lambda \cdot \boldsymbol{n} \geq 0 \\ &= \boldsymbol{F}(\boldsymbol{u}_R) = (\Lambda \cdot \boldsymbol{n})\, \tilde{h}(\boldsymbol{u}_R)\, \boldsymbol{u}_R, \qquad \Lambda \cdot \boldsymbol{n} \leq 0 \end{aligned} \tag{4.33}$$

with

$$\boldsymbol{u}_L = \frac{\boldsymbol{u}_i - \boldsymbol{u}_{i-1}}{\Delta}, \qquad \boldsymbol{u}_R = \frac{\boldsymbol{u}_{i+1} - \boldsymbol{u}_i}{\Delta} \tag{4.34}$$

This can be rewritten in a most compact way

$$\begin{aligned} \boldsymbol{F}^* (\boldsymbol{u}_L, \boldsymbol{u}_R, \boldsymbol{n}) &= \max(0, \Lambda \cdot \boldsymbol{n})\, \tilde{h}(\boldsymbol{u}_L)\, \boldsymbol{u}_L + \min(0, \Lambda \cdot \boldsymbol{n})\, \tilde{h}(\boldsymbol{u}_R)\, \boldsymbol{u}_R \\ &= \Lambda^{nL}\, \tilde{h}(\boldsymbol{u}_L)\, \boldsymbol{u}_L + \Lambda^{nR}\, \tilde{h}(\boldsymbol{u}_R)\, \boldsymbol{u}_R \end{aligned} \tag{4.35}$$

Since that the advection velocity Λ is always positive for this problem, the information goes from the left side of the domain toward the right side. Thus, the convective flux can be expressed as

$$\boldsymbol{F}^* = \boldsymbol{F}(\boldsymbol{u}_L) \tag{4.36}$$

4.2.3 Penalty Term

As presented in section 4.1.3, an internal penalty method is used for the evaluation of the diffusive interface flux $\gamma^{\boldsymbol{D}}$. More specifically, an incomplete interior penalty method (IIPM) (*i.e.* $\theta = 0$) is considered since it is the only one implemented in ForDGe. The choice of σ is based on [42]. A generic expression for the minimal penalty coefficient σ_f^* is given

$$\sigma_f^* = Cp^2 \cdot \frac{\mu^*}{h^*} \tag{4.37}$$

with h^* the length scale of the element, μ^* the diffusivity scale, p the interpolation order and C the fudge factor used as a correction since there are some uncertainties over the choice of h^*. The following values are used since one have Cartesian grid

$$C = (p+1)^2, \qquad \frac{1}{h^*} = 0.5, \qquad \mu^* = \tilde{p}\tilde{h}^3 \tag{4.38}$$

The diffusivity μ^* is computed at each face of a given element and this for all the elements. The mean value is then taken. Once the minimal penalty coefficient σ_f^* is computed, the penalty term coefficient σ is calculated as follows

$$\sigma = \begin{cases} \frac{1.001}{2}\, \sigma_f^* & \text{if } \boldsymbol{D} \text{ is symmetric} \\ 1.001\, \sigma_f^* & \text{otherwise} \end{cases} \tag{4.39}$$

Consequently, the diffusive interface flux is expressed as

$$\gamma_{IPM} = \sigma[[\varphi]] \cdot [[\boldsymbol{u}]] + [[\varphi]] \cdot \langle \boldsymbol{D} \rangle \tag{4.40}$$

Note that in the case where the solution is continuous across the boundaries, the penalty term vanishes and one return back to the FEM.

4.2.4 Source Term

As presented in subsection 4.2.1, the source term is null in the compressible case. However, for journal bearings where the film thickness $\tilde{h}$ is only a function of the shaft/journal position, the 2D equation writes

$$\frac{\partial}{\partial \theta}\left(-\tilde{h}^3 \frac{\partial \tilde{p}}{\partial \theta}\right) + \frac{\partial}{\partial \tilde{z}}\left(-\tilde{h}^3 \frac{\partial \tilde{p}}{\partial \tilde{z}}\right) + \frac{\partial(\Lambda \tilde{h})}{\partial \theta} = 0 \tag{4.41}$$

and thus

$$\boldsymbol{u} = \tilde{p}, \qquad \boldsymbol{F} = \begin{pmatrix} 0 \\ 0 \end{pmatrix}, \qquad \boldsymbol{D} = \begin{pmatrix} -\tilde{h}^3 \partial_\theta \tilde{p} \\ -\tilde{h}^3 \partial_{\tilde{z}} \tilde{p} \end{pmatrix}, \qquad \boldsymbol{S} = \begin{pmatrix} -\Lambda \tilde{h} \\ 0 \end{pmatrix} \tag{4.42}$$

In this case, the convective flux is null since the term $\Lambda\tilde{h}$ does not depend on the solution. The expression of the film thickness is known a priori and can therfore be injected in the equation Tab. 4.1 shows the convective/diffusive flux for the different types of equations and cases considered.

	Reynolds Equation	**Film Height**	**Convective Flux**		**Diffusive Flux**	
			$\boldsymbol{F}_\theta$	$\boldsymbol{F}_{\tilde{z}}$	$\boldsymbol{D}_\theta$	$\boldsymbol{D}_{\tilde{z}}$
Incompressible:						
1D	$\frac{\partial}{\partial\theta}\left(-\tilde{h}^3\frac{\partial\tilde{p}}{\partial\theta}\right)+\frac{\partial}{\partial\theta}(\Lambda\tilde{h})=0$	$\tilde{h}=\tilde{h}_r$	0	/	$-\tilde{h}^3\frac{\partial\tilde{p}}{\partial\theta}$	/
		$\tilde{h}=\tilde{h}_r+\tilde{h}_c$	$\Lambda\tilde{h}$	/	$-\tilde{h}^3\frac{\partial\tilde{p}}{\partial\theta}$	/
2D	$\nabla\cdot\left(-\tilde{h}^3\nabla\tilde{p}\right)+\nabla\cdot\left(\tilde{h}\right)\mathbf{s}=0$	$\tilde{h}=\tilde{h}_r$	0	0	$-\tilde{h}^3\frac{\partial\tilde{p}}{\partial\theta}$	$-\tilde{h}^3\frac{\partial\tilde{p}}{\partial\tilde{z}}$
		$\tilde{h}=\tilde{h}_r+\tilde{h}_c$	$\Lambda\tilde{h}$	0	$-\tilde{h}^3\frac{\partial\tilde{p}}{\partial\theta}$	$-\tilde{h}^3\frac{\partial\tilde{p}}{\partial\tilde{z}}$
Compressible:						
1D	$\frac{\partial}{\partial\theta}\left(-\tilde{p}\tilde{h}^3\frac{\partial\tilde{p}}{\partial\theta}\right)+\frac{\partial}{\partial\theta}(\Lambda\tilde{p}\tilde{h})=0$	$\tilde{h}=\tilde{h}_r$	$\Lambda\tilde{p}\tilde{h}$	/	$-\tilde{p}\tilde{h}^3\frac{\partial\tilde{p}}{\partial\theta}$	/
		$\tilde{h}=\tilde{h}_r+\tilde{h}_c$	$\Lambda\tilde{p}\tilde{h}$	/	$-\tilde{p}\tilde{h}^3\frac{\partial\tilde{p}}{\partial\theta}$	/
2D	$\nabla\cdot\left(-\tilde{p}\tilde{h}^3\nabla\tilde{p}\right)+\nabla\cdot\left(\tilde{p}\tilde{h}\right)\mathbf{s}=0$	$\tilde{h}=\tilde{h}_r$	$\Lambda\tilde{p}\tilde{h}$	0	$-\tilde{p}\tilde{h}^3\frac{\partial\tilde{p}}{\partial\theta}$	$-\tilde{p}\tilde{h}^3\frac{\partial\tilde{p}}{\partial\tilde{z}}$
		$\tilde{h}=\tilde{h}_r+\tilde{h}_c$	$\Lambda\tilde{p}\tilde{h}$	0	$-\tilde{p}\tilde{h}^3\frac{\partial\tilde{p}}{\partial\theta}$	$-\tilde{p}\tilde{h}^3\frac{\partial\tilde{p}}{\partial\tilde{z}}$

Table 4.1: Convective flux $\boldsymbol{F}$ and Diffusive flux $\boldsymbol{D}$ for one dimensional and two dimensional cases for incompressible and compressible fluid. The expressions are given for rigid bearings ($\tilde{h}=\tilde{h}_r$) and foil bearings ($\tilde{h}=\tilde{h}_r+\tilde{h}_c$).

A flow chart of the numerical algorithm developed in the present work is available in Fig. 4.5. For a given bearing geometry and operating conditions, the algorithm start by imposing the value 1 (ambient pressure) for the dimensionless pressure at all the mesh points. With this initial guess for the Newton-Raphson method, the film height is computed either for rigid or foil bearing. For foil bearings, the compliant height is computed using different stiffness model (*i.e.* Wallowit, Iordanoff and Larsen). The next step is the evaluation of the convective/diffusive volume/interface fluxes and the eventual source term. The residual as well as its Jacobian are also computed. The Jacobian is inverted using direct solver and the iterative process is carried out until the convergence criterion in Eq. (4.43) is satisfied. If not, the pressure at the next step is updated and the algorithm is repeated. After convergence, the pressure as well as the film thickness are obtained and used to find the load-carrying capacity and other outputs.

$$\left|\frac{p_j-p_{j-1}}{p_j}\right|\leq 10^{-8} \tag{4.43}$$

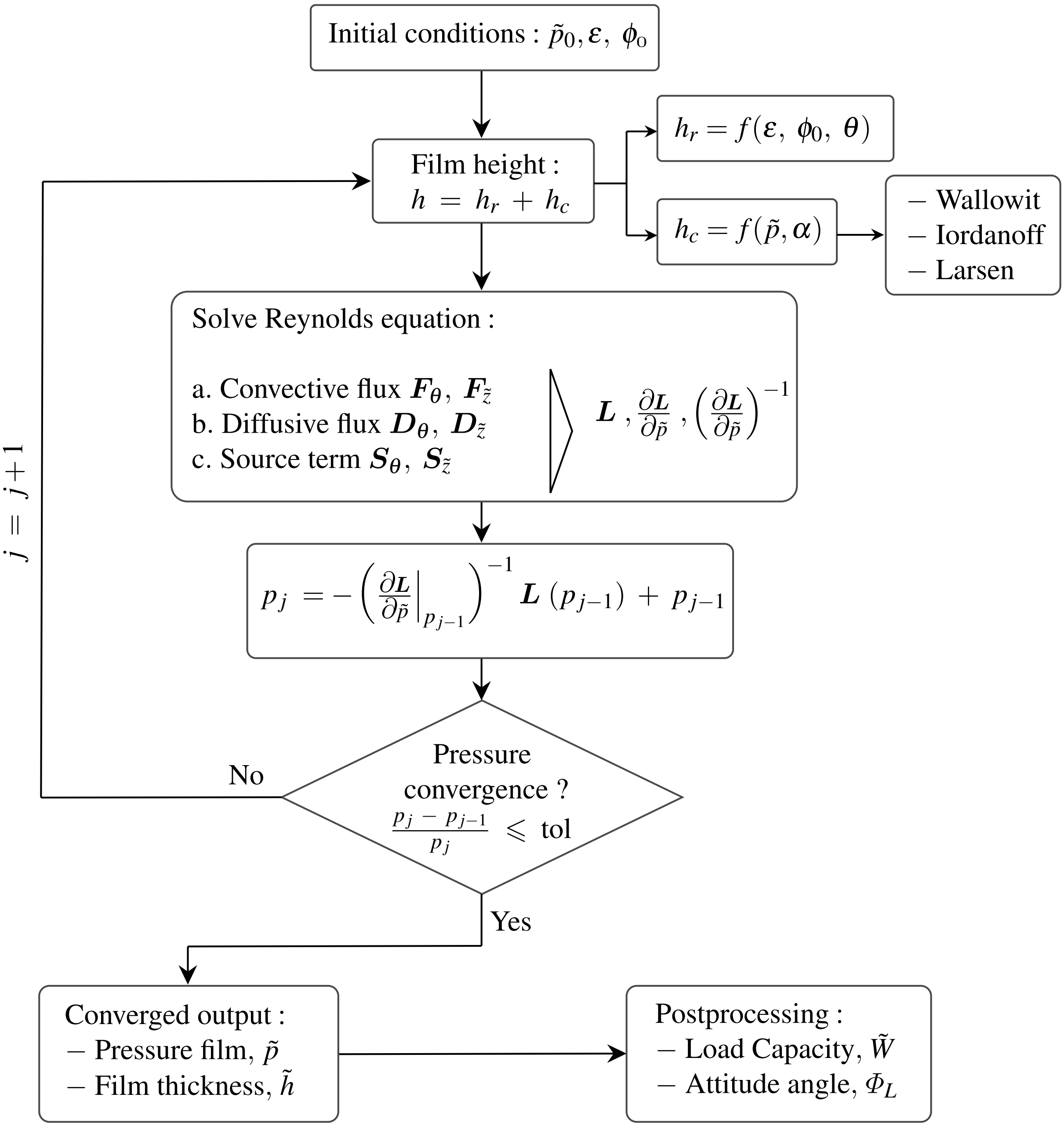

Figure 4.5: Flow chart of the numerical procedure used for gas bearings.

4.3 ForDGe Solver

This section describes the DG-FEM solver, called ForDGe, used to solve the Reynolds equation in Eq. 3.3. Still under development in the Aerospace and Mechanical engineering department of the University of Liège, this solver aims to provide highly accurate solutions to complex physics problems evolving complex geometries by using immersed boundary and, in turn, Adaptive Mech Refinement (AMR) on multiple order Cartesian grids.

ForDGe is implemented in C++ and allows a multi-threading environment with the use of OpenMP library for parallel programming. Six main parts make up its architecture:

- `Algebra` This part contains all the mathematical background needed (*i.e.* matrix, vector operations), as well as the definition of the solvers and preconditioners. ForDGe uses non-linear solver (`Newton, Damped Newton`) to reach the steady-state and linear solver (`Direct, GMRES, DGMRES`) coupled with `ILU` and `Jacobi` preconditions to solve the linear part.
- `Mesh` This part contains all the information related to the mesh, such as the dimension, the domain size, the number of cells and their interpolation order, and connectivity between elements. The data are then stored and rearranged for efficient interface computation.
- `ConservationLaw` This part includes a general class (`FConservationLaw`) that defines the template in which all the conservation law are implemented. Inheritance classes then describe the physics of the problem to be considered, including the definition of the equations to be solved, the conserved variables, the numerical fluxes and the initial and boundary conditions. Fig. 4.6 shows the classes implemented or under development until this day. In the frame of this work, `FReynoldsCLaw` has been implemented.
- `Discretisation` This part concerns the DG spatial discretisation aspect. It provides the main functionality to compute the different contributions to the residual, including convective and diffusive (Volume and interface) terms as well as the source term. The implementation of the IPM method explained in section 4.1.3 is also done in this part.
- `Finite Elements` This part contains the different quadrature rules and shape functions that are used. Lagrange shape functions associated with either equidistant, Gauss-Lobatto-Legendre (GLL) or Gauss quadrature rule controls points are used.
- `Time Integration` This part is responsible for performing the time integration. It allows explicit and implicit time integration, fourth-order Explicit `Runge-Kutta` scheme, `ESDIRK` and `RORK` scheme for implicit time integration.

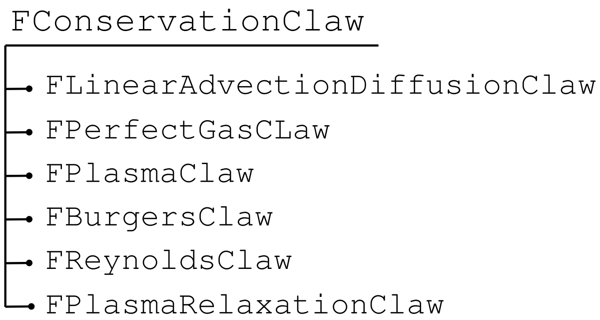

Figure 4.6: Architecture of the `FConservationCLaw` and its main inheritance classes. `FReynoldsCLaw` has been implemented in the frame of this work.

Chapter 5

Validation And Discussion

This chapter is dedicated to the validation of the implemented model. The validity of the analysis and numerical code is assessed by comparing predictions to experimental data and/or numerical results available in the literature. The code will be validated for rigid bearing and first-generation foil bearing with a single 360° pad. The first section presents a mesh convergence study of the numerical model presented in chapter 4 in the incompressible and compressible case to find the best compromise in terms of the number of elements and thus accuracy and computational cost. The second section compares predictions, especially pressure and load capacity, to existing published data.

5.1 Mesh convergence study

Incompressible case

For incompressible fluid, the convergence study is conducted based on existing analytical solutions for infinitely long journal bearing. This case corresponds to the steady state one dimensional Reynolds equation for incompressible fluid. The analytical solution used is the half-Sommerfeld solution. This last uses Dirichlet BCs (ambient pressure) at the edges of the domain (*i.e.* $\theta = 0,\ 180°$). Above $\theta = 180°$ the pressure is constant and is equal to ambient pressure.

The comparison is assessed by computing the relative L_2 norm error $L_2(e)$ between the predicted solution and that of Sommerfeld. The relative error is computed as follows

$$L_2(e) = ||u^* - u||_2 = \sqrt{\frac{\int (u^* - u)^2}{\int u^{*2}}} \tag{5.1}$$

where u^* and u stand respectively for analytical and numerical solution. The integral is carried out in the tangential direction. Fig. 5.1 show the evolution of the L_2 norm error with $1/h$ for different interpolation order $p = 1, 2, 3, 4, 5$. The quantity $1/h$ gives an indication about the degrees of freedom (DOFs) and is calculated as follows

$$\text{NDOF} = \begin{cases} N_x(p+1) & \text{in 1D} \\ N_x N_z (p+1)^2 & \text{in 2D} \end{cases}, \qquad h = \text{NDOF}^{-1/d} \tag{5.2}$$

with N_x and N_z the number of element in the x and z direction, d the dimension and p the interpolation order. As it can be seen in Fig. 5.1, the error decreases as long as the domain is refined. The error decreases also with increasing interpolation order p so that high accuracy can be obtained by choosing high interpolation order and a large stencil size. However, as far as numerical simulation is concerned, computational cost becomes one of the important aspect. More precisely, increasing p results in higher accuracy than increasing

N_x at the expense of higher computational cost. This effect will be shown latter in the compressible case. Therefore, A compromise need to be found. By choosing $N_x = 50$ and $p = 4$, a relative error of $\approx 9.44 \times 10^{-7}$ could be obtained, which is relatively sufficient to provide results with high accuracy and acceptable computational time. Note that in Fig. 5.1, one can retrieve the interpolant order from the slope of the corresponding curve. More precisely, the slope of a given curve is equal to p if the corresponding order is an even number (*i.e.* $p = 2,4$) and is equal to $p+1$ if it corresponds to an odd number (*i.e.* $p = 1,3,5$).

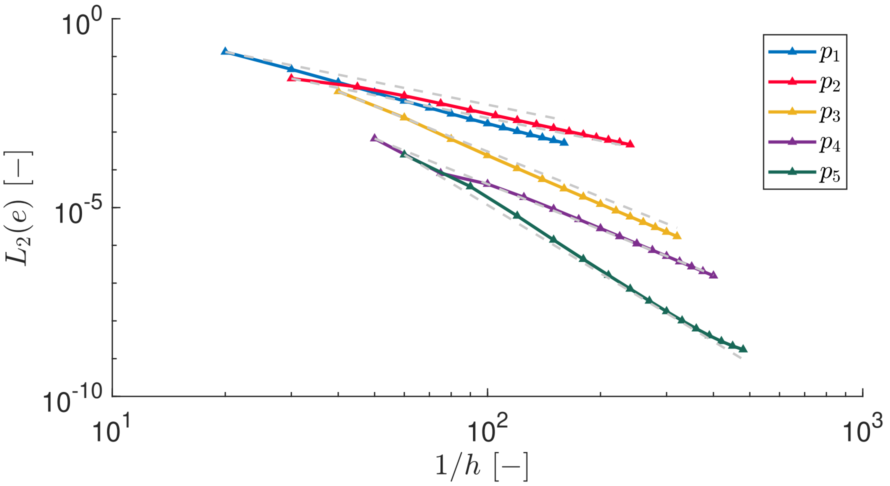

Figure 5.1: Evolution of relative L_2 norm error with $1/h$ for rigid bearing in the incompressible case with $\varepsilon = 0.8$, and $\Lambda = 1$. The results are shown for different interpolations order p with $N_x \in [10;120]$.

Compressible case

For compressible fluids, no analytical solution exists. Therefore, a mesh convergence study is conducted based on the maximum predicted pressure peak inside the bearing. The current case corresponds to the steady state two-dimensional Reynolds equation for compressible fluids. Fig. 5.2 and Fig 5.3 depict the evolution of the maximum pressure peak with $1/h$ for rigid and foil bearing respectively. In Fig. 5.2a and Fig. 5.3a, the number of elements along the z direction is fixed to $N_z = 20$ while N_x takes values between 10 and 120. The results show that the value of the pressure peak converges to a relatively fixed value for high order of interpolation. This effect is delayed to a higher value of N_x for foil bearing. For low interpolation order (*i.e.* $p = 2$), the results are not satisfactory for both rigid and foil bearings.

Similarly, in Fig. 5.2b and Fig. 5.3b, the number of elements along the x direction is fixed to $N_x = 40$ while N_z is varying from 10 to 120. The same remarks as previously are still applicable here, except that the pressure peak converges more rapidly in this case than when varying N_x (*i.e.* one converges faster for each order). This can be explained by the fact that the solution does not change significantly in this direction. Finally, the computational time are plotted in Fig. 5.2c and Fig. 5.3c for rigid and foil bearing respectively. The results show an increase in the computational time with interpolation order. Additionally, the different curves are shifted to a higher value of computational time for foil bearings. This is due to the additional non-linearity added in this case, as the film thickness depends on the pressure itself. Additional iterations were thus necessary for the Newton-Raphson method to reach convergence. Note that for all the above-depicted graphs, a relative convergence of 10^{-8} has been used for the Newton-Raphson method.

In the following, the number of elements in the tangential direction, axial direction and the interpolation order used in the case of rigid bearings are $N_x = 50, N_z = 30, p = 4$ while those used in the case of foil bearings are $N_x = 80, N_z = 50, p = 4$.

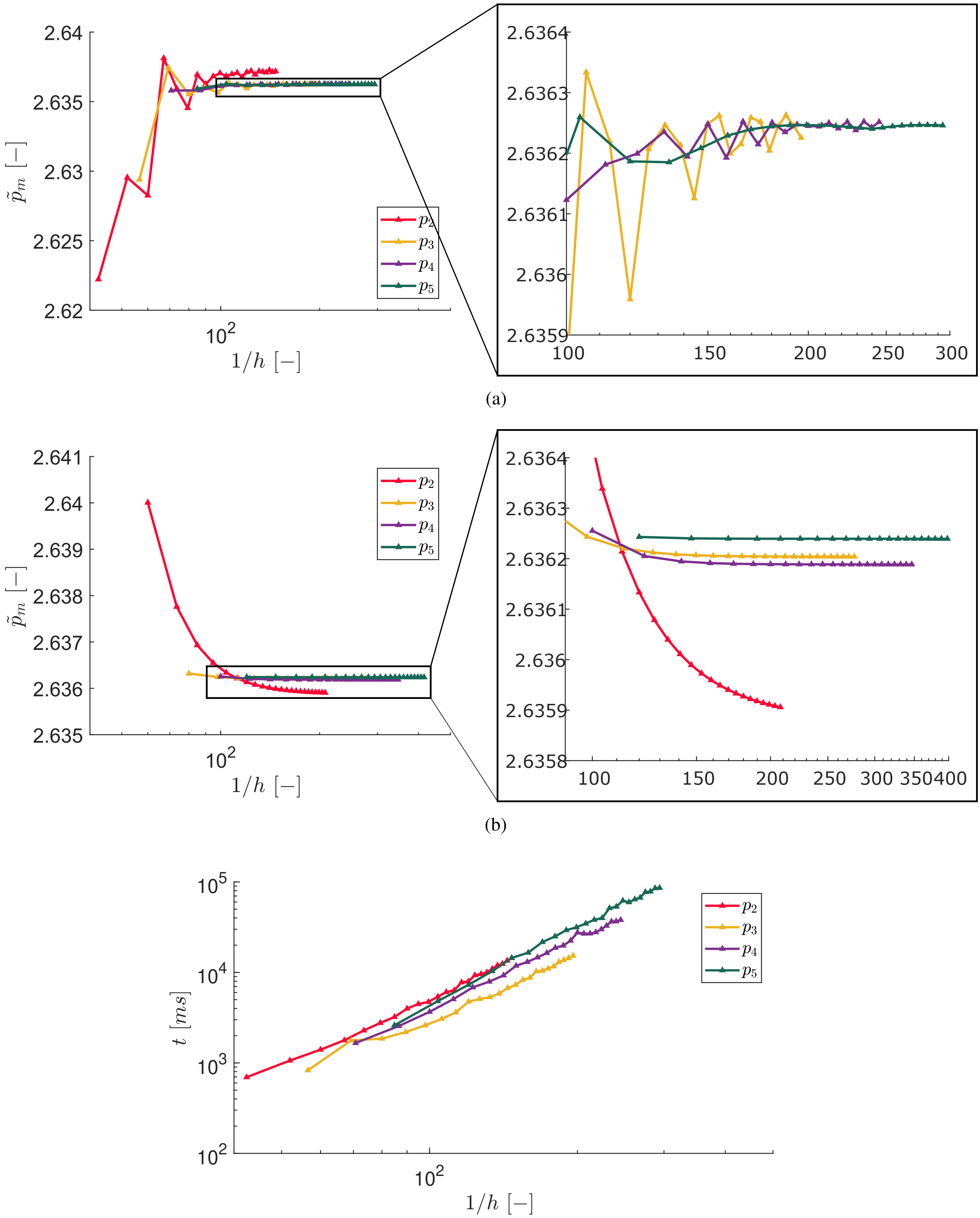

(a)

(b)

(c)

Figure 5.2: Evolution of (a,b) Maximum pressure peak and (c) Computational time with $1/h$ for rigid bearing in the compressible case with $\varepsilon = 0.8$, $L/D = 1$ and $\Lambda = 1$. The results are shown for different interpolations order p with (a) $N_z = 20, N_x \in [10; 120]$ and (b) $N_x = 40, N_z \in [10; 120]$.

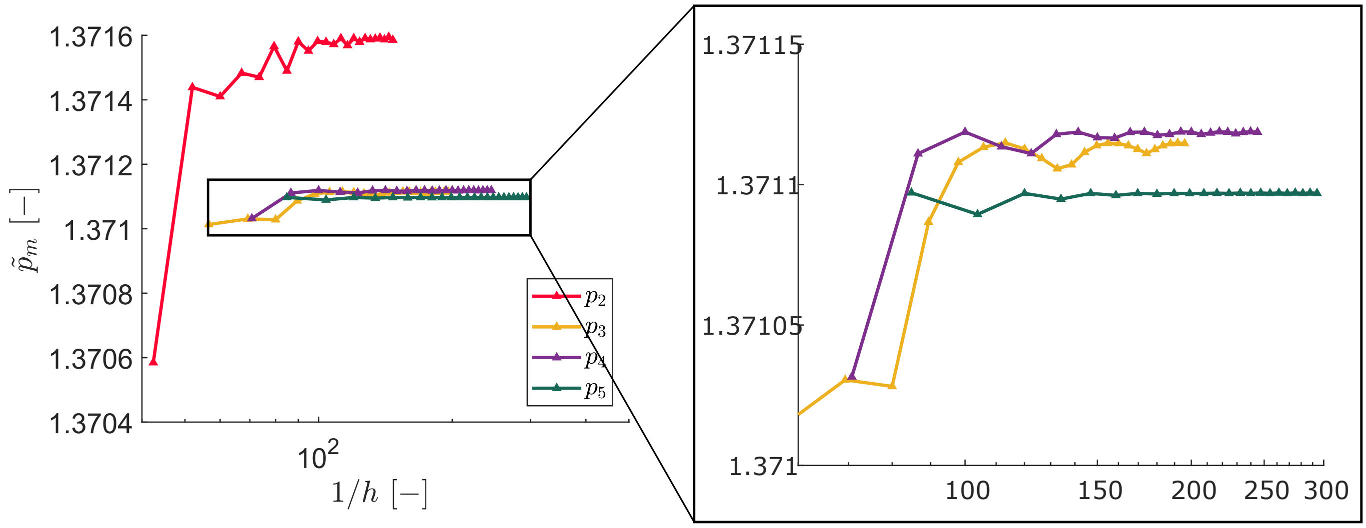

(a)

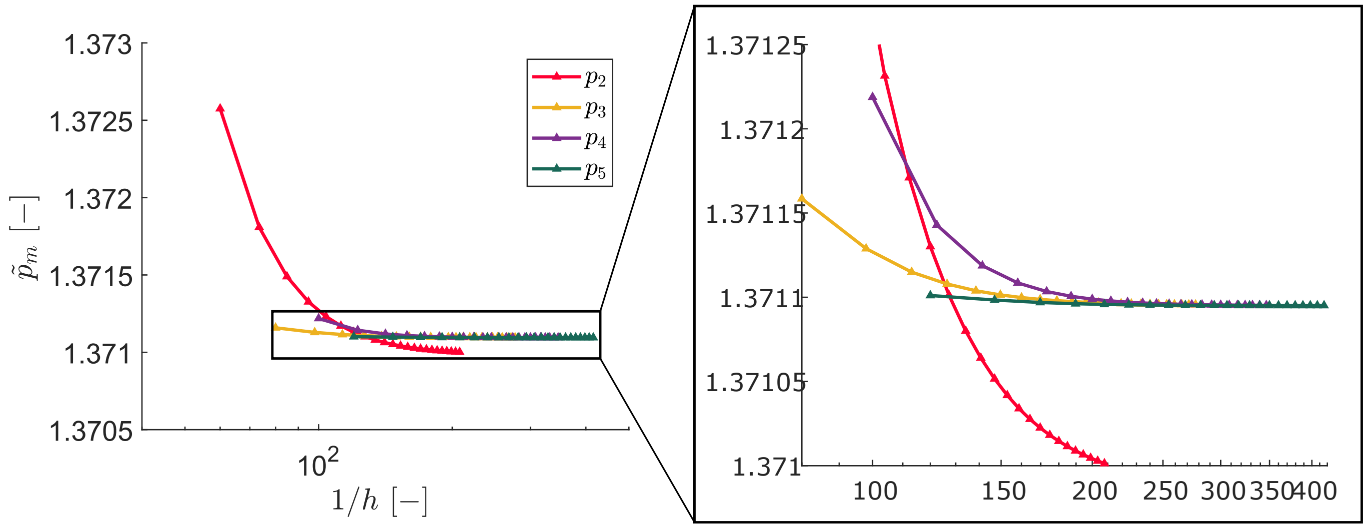

(b)

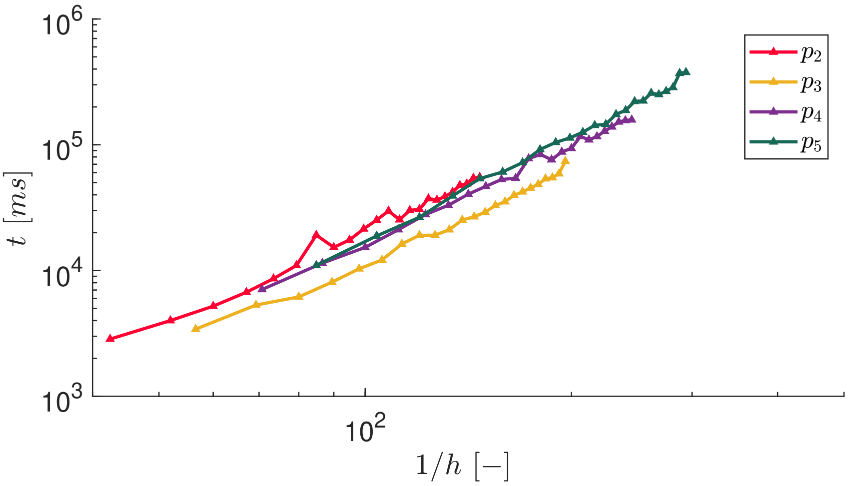

(c)

Figure 5.3: Evolution of (a,b) Maximum pressure peak and (c) Computational time with $1/h$ for first generation foil bearing in the compressible case with $\varepsilon = 0.8$, $L/D = 1$ and $\Lambda = S = 1$. The results are shown for different interpolations order p with (a) $N_z = 20, N_x \in [10;120]$ and (b) $N_x = 40, N_z \in [10;120]$.

5.2 Validation of static performance

This section compares the pressure and the steady-state static performance to published data. Fig. 5.4 compares predicted pressure distribution to Sommerfeld and Cameron and Wood incompressible solutions for $\varepsilon = 0.9$ and $\Lambda = 1.2511$. The first uses Dirichlet BCs (ambient pressure) at the domain boundaries, whereas the second imposes Neumann Bc (zero pressure gradient) at the end of the domain. Perfect matching between predictions and analytical solutions is observed, which enforces the present numerical model for rigid bearings. Moreover, the load-carrying capacity is represented in Fig. 5.5 where predictions are compared to perturbed solutions and numerical models. At low eccentricity ratio (*i.e.* $\varepsilon < 0.4$), all the results coincide. Above this value, the 1st order perturbation model is no more valid since it is only considered a first-order term. On the other hand, the linearized *ph* solution underestimates the load capacity at high eccentricity ratios. Finally, predictions follow the other numerical codes.

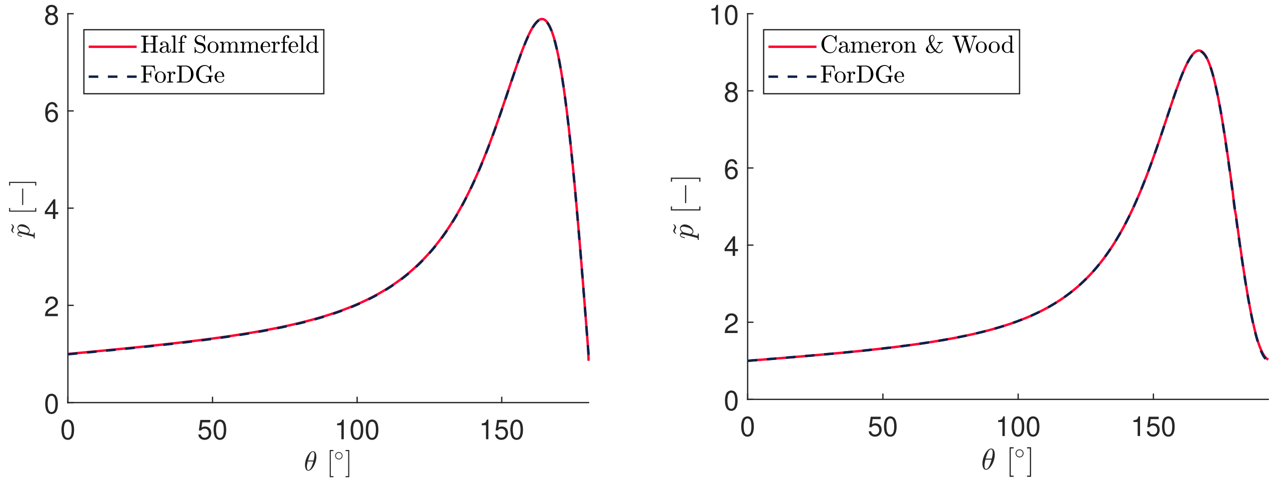

(a) Sommerfeld (b) Cameron and Wood

Figure 5.4: Pressure distribution for infinitely long journal bearing in the incompressible case with $\varepsilon = 0.9$ and $\Lambda = 1.2511$.

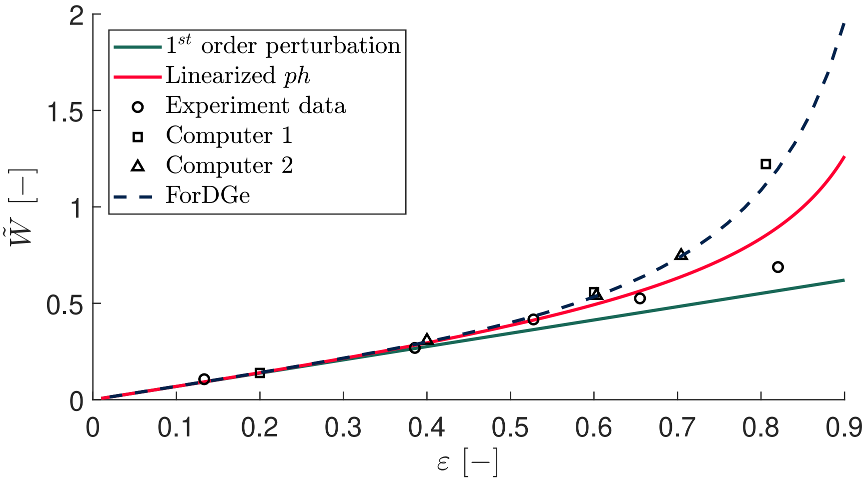

Figure 5.5: Load versus eccentricity ratio for finite journal bearing in the compressible case. The results are obtained with $\Lambda = 1.3$ and $L/D = 1.5$.

Tab. 5.1 compares the load-carrying capacity and the attitude angle with the published data of Heshmat et al. [10], Peng and Caprino [16], Patil et al. [43] and Jamir et al. [47] with $L/D = \Lambda = 1$ and $S = 0,\ 1$ for different eccentricity ratio ε. Note that a bearing with bearing compliance $S = 0$ is equivalent to a rigid gas bearing.

According to Heshmat [10], similar BCs to those used for cavitation must be used. Indeed, the construction of the foil bearings does not permit the generation of sub-ambient pressures. When sub-ambient pressures are produced in the fluid film, especially in the divergent region, the reigning ambient pressure will lift the top foil up until both sides of the foil are experiencing equal pressures. Thus to be able to compare with the aforementioned references, The results are obtained with Reynolds BCs at an unknown angular position θ_2, which from continuity requirements must fulfil both ambient pressure and zero pressure gradient BC. The BCs used in the tangential direction are thus

$$\begin{aligned} &\text{at}\ \ \theta = \theta_l \qquad \tilde{p} = 1 \\ &\text{at}\ \ \theta = \theta_2 \qquad \tilde{p} = 1\ \ \text{and}\ \ \frac{\partial \tilde{p}}{\partial \theta} = 0 \end{aligned} \tag{5.3}$$

Heshmat gives an estimation of θ_2 for different values of eccentricity ratio. This angle depends on the angular position of the pressure peak and thus on the eccentricity ratio. Note that in addition to the BCs mentioned in Eq. (5.3), ambient pressure are enforced at the edges of the bearings ($\tilde{p} = 1$ at $\tilde{z} = 0,\ \tilde{L}$). Patil et al. uses similar BCs than Heshmat et al. while Peng and Caprino and Jamir et al. impose ambient pressure in both directions (*i.e.* $\tilde{p} = 1$ at $\theta = \theta_l,\ \theta_t$ and $\tilde{z} = 0,\ \tilde{L}$).

From Tab. 5.1, it can be seen that for foil bearing ($S = 1$), the present results are in good agreement with those from the reference, validating the present computational model. In the case where $S = 0$, good matching is observed. However, a minor overestimation of the load-carrying capacity is observed at high eccentricity ratios. Fig. 5.6 compares the predicted pressure distribution, the compliant surface deflection, and the film thickness of the first-generation foil bearing with the results provided in [43]. The results show relatively good agreement, despite slight differences between minimum and maximum pressure/film thickness angular positions. The values of the maximum and minimum pressure, deflection and film thickness are the same as those obtained in [43] (see Tab. 5.1).

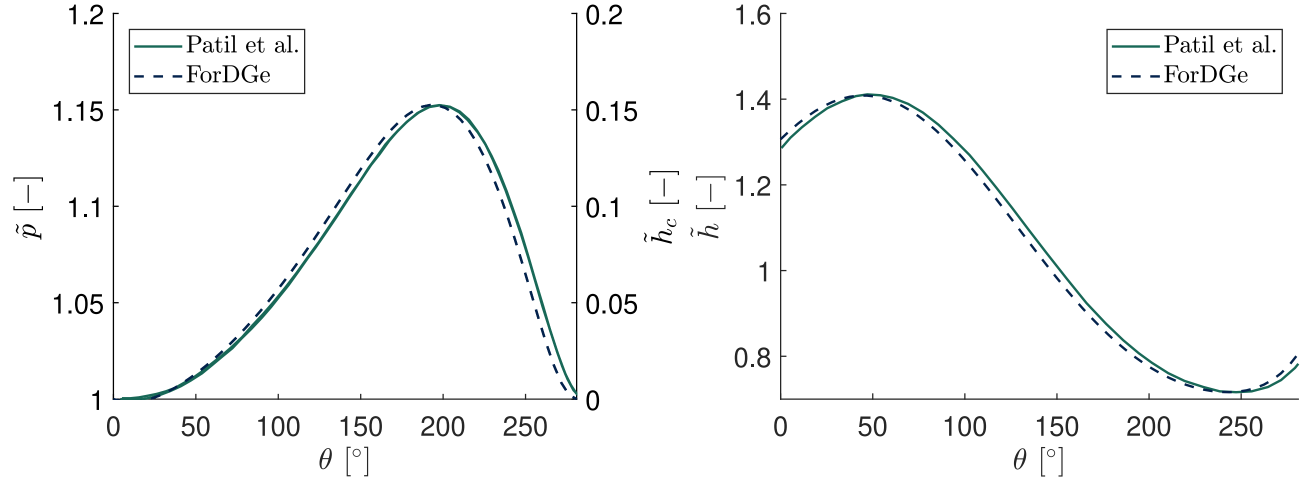

(a) Nondimensional Pressure/Deflection (b) Nondimensional Film Thickness

Figure 5.6: Mid-plane (a) Pressure distribution and Foil deflection and (b) Film thickness of a 360° foil bearing with Reynolds BCs. The results are shown for $\varepsilon = 0.4$, $\phi_0 = 40°$ and $L/D = \Lambda = S = 1$.

Compliance	Eccentricity ratio	Max. pressure		Attitude angle		load	
S, α	ε	$\tilde{p}_{\max}$ (present)	$\tilde{p}_{\max}$	Φ_L (present)	Φ_L	$\tilde{W}$ (present)	$\tilde{W}$
0	0.6	1.542	/	36.56	35.70^{a} 36.50^{b} 36.85^{c} 36.13^{d}	0.964	0.951^{a} 0.961^{b} 0.969^{c} 0.898^{d}
	0.75	2.189	/	24.50	24.10^{a} 24.70^{b} 24.37^{c} 24.12^{d}	1.936	1.894^{a} 1.922^{b} 1.963^{c} 1.847^{d}
	0.9	4.866	/	12.96	12.80^{a} 12.90^{b} 12.69^{c}	5.265	5.055^{a} 5.073^{b} 5.150^{c}
1	0.6	1.254	1.253^{a}	34.42	32.10^{a} 34.00^{b} 34.41^{c} 35.55^{d}	0.577	0.568^{a} 0.567^{b} 0.554^{c} 0.515^{d}
	0.75	1.321	/	28.48	26.30^{a} 27.70^{b} 28.07^{c} 28.53^{d}	0.794	0.783^{a} 0.778^{b} 0.763^{c} 0.728^{d}
	0.9	1.435	1.434^{a}	24.31	21.40^{a} 22.40^{b} 22.20^{c}	1.042	1.028^{a} 1.020^{b} 1.008^{c}

[a] Heshmat et al. [10]
[b] Peng and Carpino [16]
[c] Patil et al. [43]
[d] Jamir et al. [47]

Table 5.1: Steady state characteristics of a 360° foil bearing with $L/D = 1$ and $\Lambda = 1$. The attitude angle Φ_L is measured in degree.

In order to to be able to compare predictions concerning the load-carrying capacity with those of references, the load-carrying capacity is presented with an eccentricity ratio varying from 0.1 to 0.8 for different values of compliance factor S, bearing number Λ and length to diameter ratio L/D. The load components are computed the same way they are computed in the reference cases.

$$\left\{ \begin{array}{c} \tilde{W}_x \\ \tilde{W}_y \end{array} \right\} = \begin{cases} \int_0^{\tilde{L}} \int_0^{2\pi} (\tilde{p}-1) \left\{ \begin{array}{c} -\cos\theta \\ \sin\theta \end{array} \right\} d\theta d\tilde{z}, & \text{if} \quad \tilde{p} > 1 \\ \mathbf{0}, & \text{otherwise} \end{cases} \tag{5.4}$$

Fig. 5.7 compares the load-carrying capacity with increasing eccentricity ratio with those obtained from references. Perfect matching is observed with Patil et al.. However, some difference appears when compared to Jamir et al. due to the insufficient data points provided. Fig. 5.8, Fig. 5.9 and Fig. 5.10 compares the evolution of the load capacity with eccentricity ratio in the case of foil bearing and for different value of S, Λ and L/D respectively with published data. The figures mentioned above show that the present results are in very good agreement with those from references, especially at low and moderate values of eccentricity ratio. However, some discrepancies appear at high eccentricity ratios where an overestimation of the load capacity is observed.

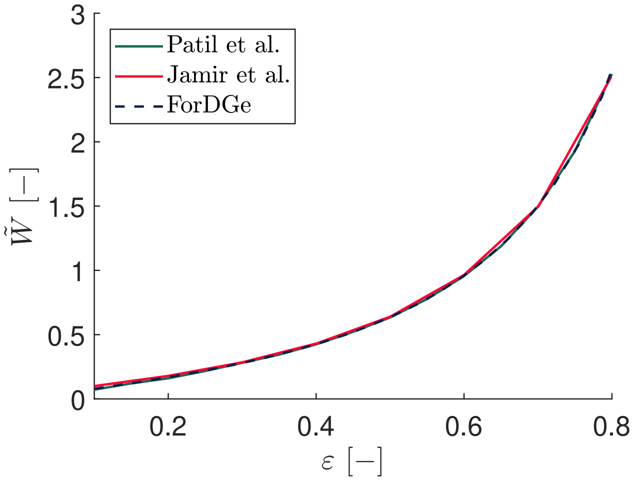

Figure 5.7: Load-carrying capacity versus eccentricity ratio for rigid bearing with $\Lambda = L/D = 1$ and $S = 0$.

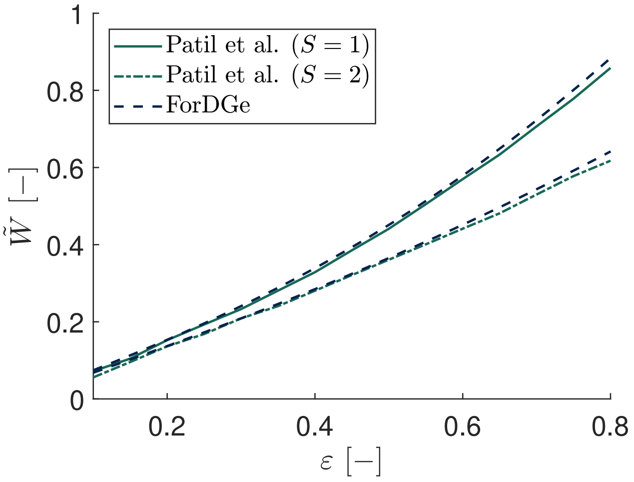

Figure 5.8: Effect of foil compliance on the load-carrying capacity with eccentricity ratio. The results are obtained with a first generation foil bearing ($\beta = 360°$) with $\Lambda = L/D = 1$ and $S = 1, 2$.

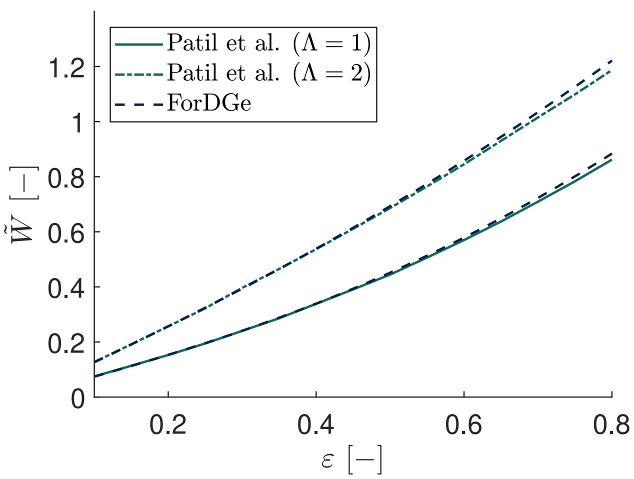

Figure 5.9: Effect of bearing number on the load-carrying capacity with eccentricity ratio. The results are obtained with a first generation foil bearing ($\beta = 360°$) with $L/D = S = 1$.

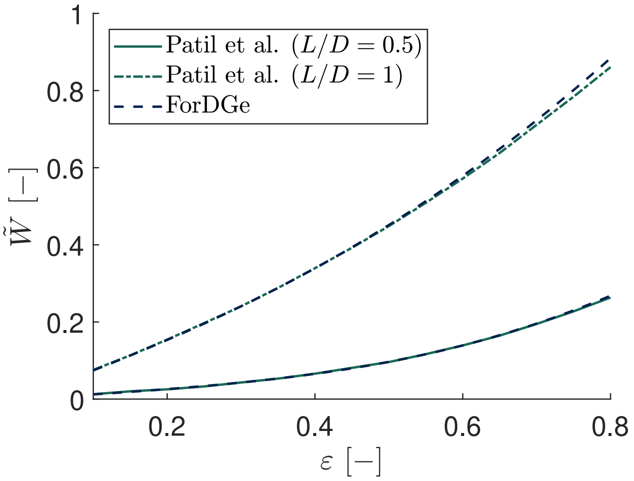

Figure 5.10: Effect of length to diameter ratio on the load-carrying capacity with eccentricity ratio. The results are obtained with a first generation foil bearing ($\beta = 360°$) with $\Lambda = S = 1$.

For further validation, predictions are compared essentially to the experimental data provided by Ruscitto [9] but also to other numerical simulations performed by other authors [31, 29, 23, 55]. The foil bearing used by [9] is a first-generation foil bearing with a single 360° bump layer topped by a top foil. Both are made of Inconel X750 and are welded to the bearing housing at one end and free at the other. The design parameters of the tested foil bearing are reported in Tab. 5.2.

Parameter	**Symbol**	**Value**	**Unit**
Bearing length	L	38.1	mm
Bearing radius	$R = D/2$	19.05	mm
Radial clearance	C	31.8	µm
Ambient pressure	p_a	101325	Pa
Dynamic viscosity	μ	$1.85\,.10^{-5}$	$\mathrm{N.s.m^{-2}}$
Friction coefficient	μ_f	0.05	/
Top foil thickness	t_t	101.6	mm
Bump foil thickness	t_b	101.6	mm
Bump pitch	s_b	4.572	mm
Half bump length	l_b	1.778	mm
Bump height	h_b	0.508	mm
Bump foil Young's modulus	E_b	214	GPa
Bump foil Poisson ratio	ν_b	0.29	/
Number of bumps	N_b	26	/

Table 5.2: Design parameters of foil bearing [9, 23].

In order to be consistent with the reference cases [9, 31, 29], Iordanoff's formulas are used to estimate the bump structural stiffness. The bump pitch is considered constant, and interaction between adjacent bumps is neglected. This leads to a bump stiffness per unit area for a welded-free ($K_I^{fw} = 4.7 \times 10^9$ N/m^3) ends and a free-free ($K_I^{ff} = 1.04 \times 10^{10}$ N/m^3) ends respectively. Additionally, the nominal clearance is set to 31.8 µm as reported it citeRuscitto. Finally, all tests are performed with air at ambient conditions.
Fig. 5.11 and Fig. 5.12 compare the minimum film thickness and the journal attitude angle versus static load, respectively for operation speed $\omega = 30$ krpm and $\omega = 45$ krpm with those of reference. The curves are established by carrying out multiple simulations, and during each simulation, the journal eccentricity is slightly increased along the radial direction. The minimum film thickness and resulting force are then recorded. The load capacity are computed according to Eq. (5.4).

The predicted results concerning the film thickness are in relatively good agreement with Kim et al. data with minor discrepancies. This difference between predictions and numerical data can be explained by the fact that in the reference model, the film thickness does not vary across the bearing width since their model relies on an axially averaged pressure field [29]. Indeed, the present results are computed based on local pressure, which potentially varies along the axial direction. On the other hand, at low load capacity, there is a significant discrepancy between predictions and experimental results for both minimum film thickness and attitude angle. The main reason is due to the fabrication inaccuracy (*i.e.* a lack of conformity between the arc radius of the bump layer and the top foil). Additionally, Ruscitto et al. [9] do not report the uncertainty of their test results, including the nominal radial clearance. Concerning the attitude angle, predictions are slightly underestimated. Notably, the small attitude angles at high load capacity demonstrate decreased cross-coupled hydrodynamic effects and show the foil-strip structure to be the dominant factor [31, 29]. Finally, it can be seen that the smallest predicted average film thickness reported in Fig.5.11 is about 11 µm. This means that the minimum film thickness across the bearing width is even smaller. In this case, the problem becomes singular, and the code crashes when trying to invert the Jacobian.

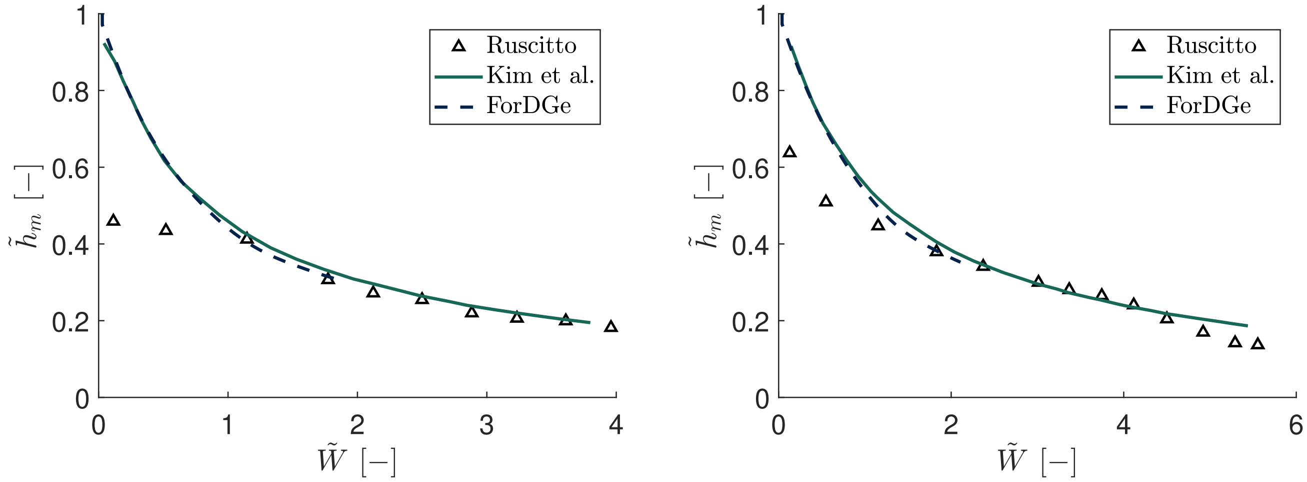

(a) $\omega = 30,000$ rpm (b) $\omega = 45,000$ rpm

Figure 5.11: Average minimum film thickness versus static load for two different angular speed. The results are obtained with foil bearing whose design parameters are listed in Tab. 5.2.

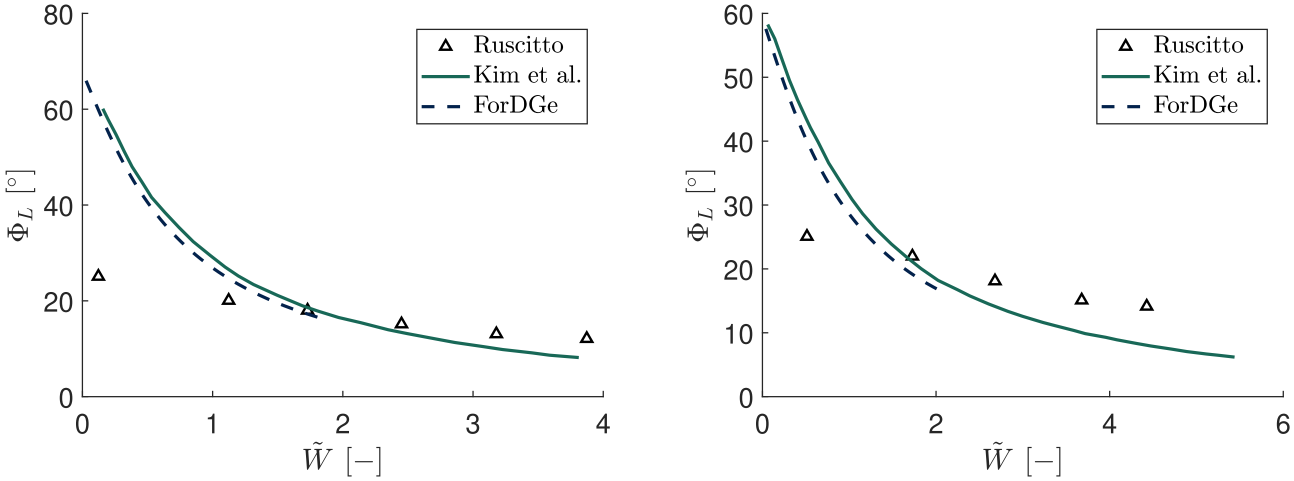

(a) $\omega = 30,000$ rpm (b) $\omega = 45,000$ rpm

Figure 5.12: Average journal attitude angle versus static load for two different angular speed. The results are obtained with foil bearing whose design parameters are listed in Tab. 5.2.

For further validation of the pressure distribution, predictions are compared to those of Peng et al. [23] and Sankar et al. [55]. The design parameters of the tested bearing are reported in Tab. 5.2 except that here, the nominal clearance is set to 50 µm. The bumps are modelled using linear elastic springs. Wallowit formula used firstly by Heshmat [10] is used for estimating the bump stiffness. Fig. 5.13 and Fig. 5.14 compare the predicted dimensionless pressure and film thickness with those from references in the case of rigid and foil bearing, respectively. The results are obtained with $\varepsilon = 0.79$ with a compliance factor of 0.4 for foil bearing. A good agreement could be observed with a small overestimation of the pressure peak. On the other hand, an underestimation of the minimum pressure is observed for foil bearing.

For foil bearing, the eccentricity ratio can take values greater than unity. Hence to compare the pressure generating ability, the eccentricity ratio is increased such that the minimum film thickness is maintained the same as that of rigid bearing (see [23, 55]). A minimum film thickness of 10.5 µm is used throughout the simulations. This minimum value, if exceeded, could result in surface-to-surface contact and thus to the failure of the bearing [23]. Fig. 5.15 and Fig. 5.16 show the results obtained with an eccentricity ratio of $\varepsilon = 1.26$ and $\varepsilon = 1.13$ respectively. Good matching is observed when compared to Sankar et al.. A small overestimation of the minimum film thickness is observed, leading to lower minimum and maximum pressure peaks for predictions. Moreover, discrepancies between predictions and Peng et al. data are identified. This can be explained by the fact that in Peng et al. study, more precisely in the estimation of the pressure, the attitude of the shaft has been adjusted along with the eccentricity. In the current study, as in Sankar et al. work, only the clearance is updated such that the minimum film thickness is maintained the same between rigid and foil bearing. Note that in Peng's work, periodic BCs in the tangential direction are enforced, while for Sankar, ambient pressure is enforced. In the present work, similar BCs to [55] is used.

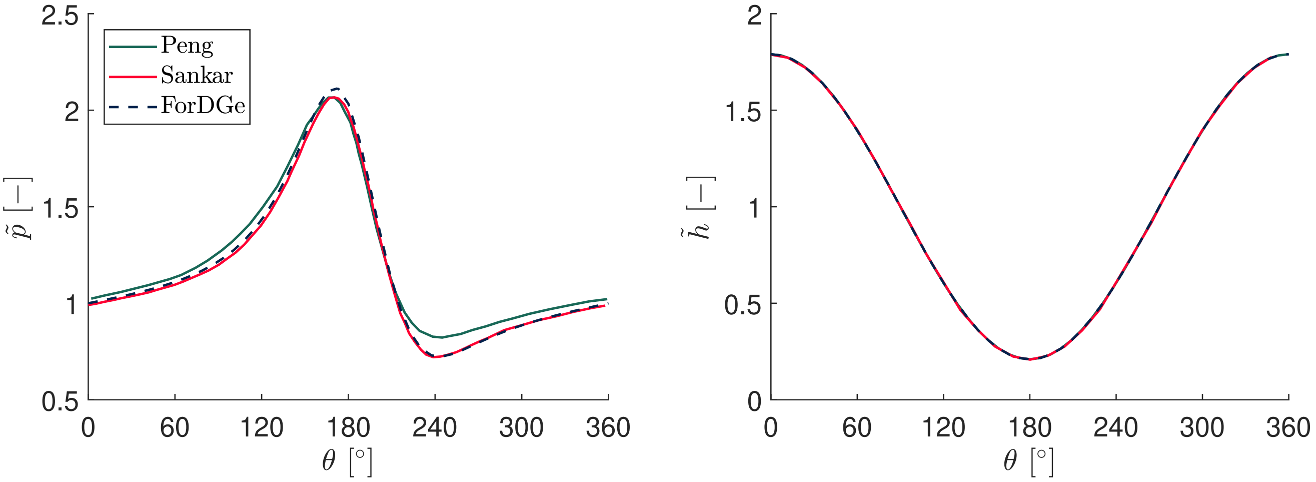

(a) Dimensionless pressure

(b) Dimensionless film thickness

Figure 5.13: Mid-plane (a) Pressure distribution and (b) Film thickness of a rigid bearing with $\varepsilon = 0.79$.

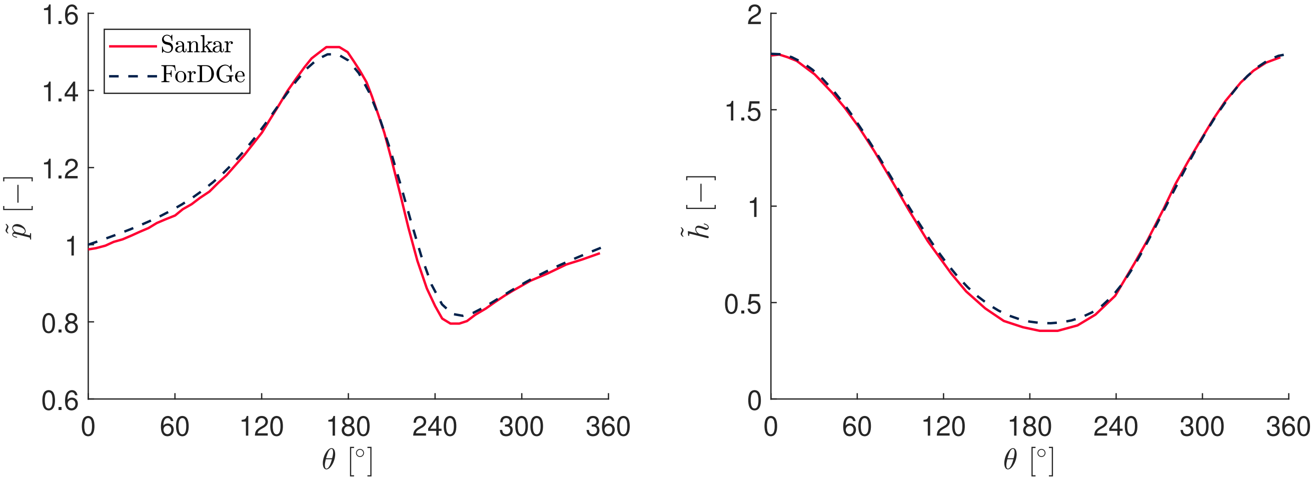

(a) Dimensionless pressure

(b) Dimensionless film thickness

Figure 5.14: Mid-plane (a) Pressure distribution and (b) Film thickness of a 360° foil bearing with $\varepsilon = 0.79$.

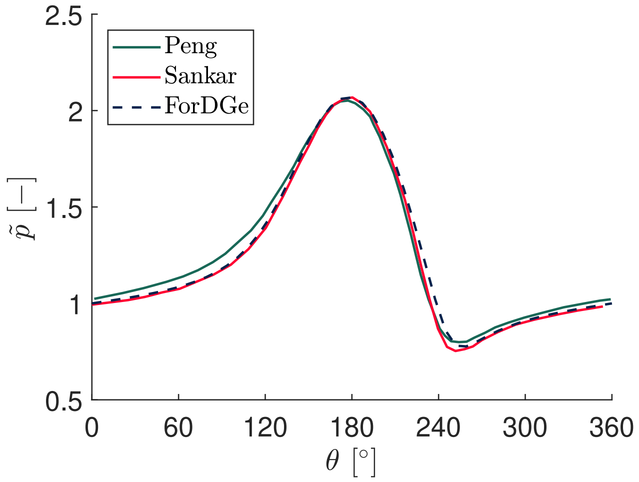

Figure 5.15: Mid-plane pressure distribution of a 360° foil bearing with $\varepsilon = 1.26$.

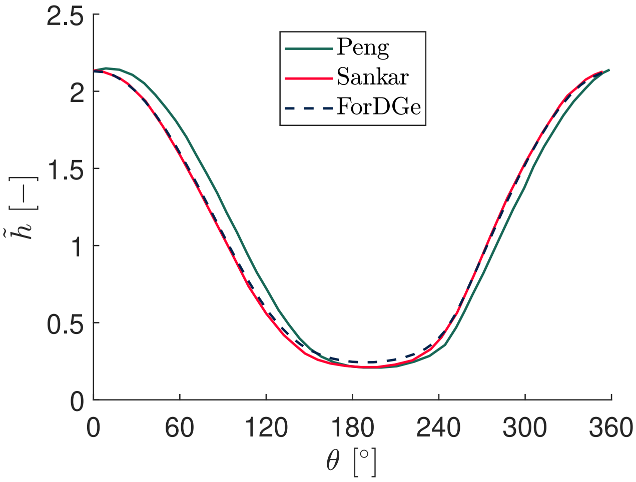

Figure 5.16: Mid-plane film thickness of a 360° foil bearing with $\varepsilon = 1.12$. The result from [55] are computed with $\varepsilon = 1.13$.

RESULTS

Chapter 6

Impact of Design Parameters on Bearing Load Capacity

This chapter shows the impacts of main design parameters on the static performance of GFBs. More precisely, the impact of loading position ϕ_0, bearing number Λ, bearing compliance factor S, length-to-diameter ratio L/D, stiffness model and the addition of inlet slope on the load capacity is shown. The results are obtained with an eccentricity ratio varying from 0.1 to 0.8. The dimensionless load $\tilde{W}$ is computed following Eq. (5.4).

Three different bearing configurations are investigated, one 360° pad, two 180° pads, and three 120° pads foil bearing. The two-dimensional Reynolds equation for compressible fluids is solved under steady-state conditions. The boundary conditions used are those presented in section 3.1.1. All The results are obtained using 80 elements and 40 elements in the tangential and axial direction of the bearing, respectively, with interpolation order $p = 4$. The followed numerical algorithm is that of Fig. 4.5.

6.1 Loading position

In the following, the pressure distribution and film thickness are shown for the three bearings configurations with $\varepsilon = 0.8$, $\phi_0 = 0°$, $\Lambda = 0.66$, $S = 0.12$, $L/D = 1/2$ and different values of ϕ_0. In particular, two scenarios will be considered, either ϕ_0 is at the attachment point or the middle of a given pad. This allows quantifying two extreme cases where the load could eventually be minimum or maximum.

Fig. 6.2, Fig. 6.3 show the pressure distribution and film thickness for single pad foil bearing with the design parameters cited above and $\phi_0 = 180°$ and $\phi_0 = 0°$ respectively. The mid-plane pressure and film height are also presented. It is clear that the pressure profiles are different in shape in the two cases, and this is due to the boundary conditions imposed at the attachment point. However, one retrieves the classical known pressure profile with a convergent region followed by a divergent region where the pressure takes values lower than ambient pressure. In the first case (*i.e.* $\phi_0 = 180°$), the maximum pressure peak is near the attachment point, and thus the pressure is forced to take ambient value at this position. Therefore, the area of the convergent region is reduced, and that of the divergent region is increased. It should be noted that if the value of ϕ_0, the angle of minimum film thickness, is changed, the pressure profile is delayed either to the left or the right depending if ϕ_0 is positive or negative, respectively. The film height increases from the bearing edge toward the bearing centerline, where its maximum values are observed. The maximum pressure ($\tilde{p}_m = 1.48$) is found to be at the midplane of the bearing width. Its value is the same for both cases.

Again, two cases are investigated for the two pads bearing when ϕ_0 is at an attachment point or at the middle of a given pad. Fig. 6.4 and Fig. 6.5 show the pressure and film height for $\phi_0 = 0°$ and $\phi_0 = -90°$

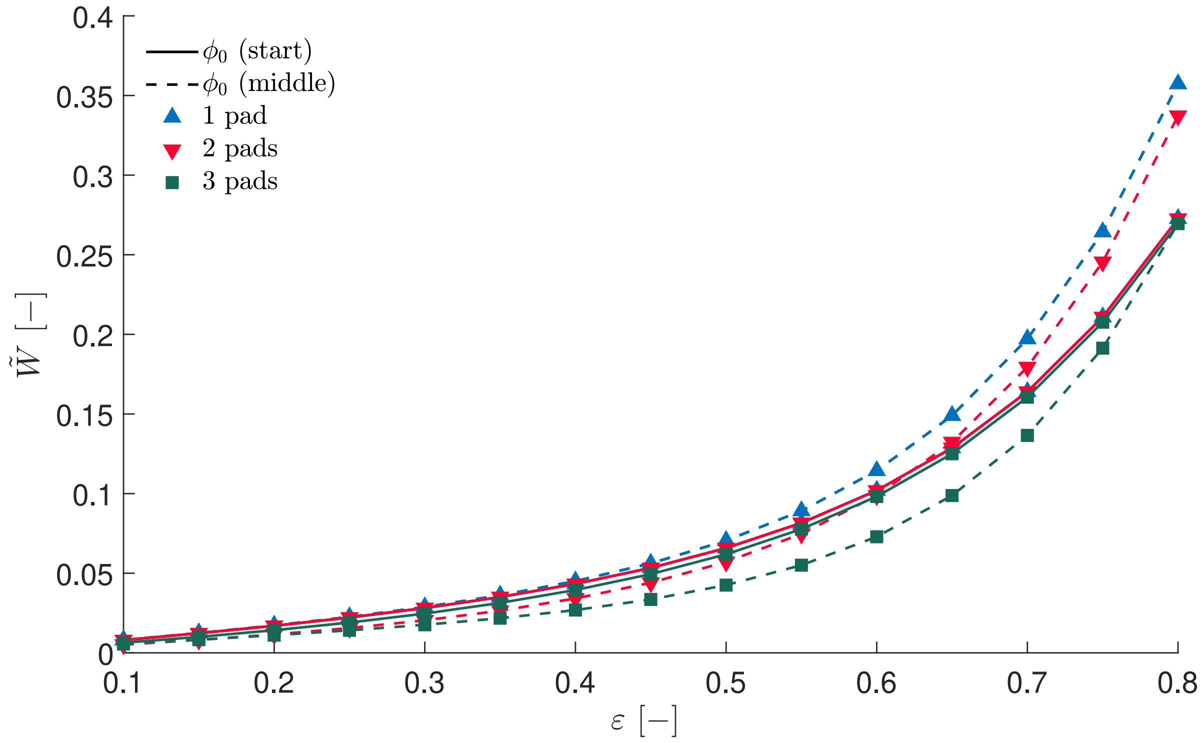

Figure 6.1: Effect of loading position on Load capacity for different bearing geometries, one pad (in blue ▲), two pads (in red ▼) and three pads (in green ■). The results are obtained with $\Lambda = 0.66$, $S = 0.12$, $L/D = 1/2$ and $\theta_l = 0°$. The solid line and dashed line are for ϕ_0 at start and middle pad of corresponding bearing respectively.

respectively. Same interpretations as those cited previously for the one pad bearing are applicable except that here, the shape is more complex due to the additional BC at $\theta = 180°$. The pressure film is separated into several regions (convergent and divergent) whose areas depend on the position on ϕ_0. The convergent area could be extended at the expense of a smaller divergent region and vice versa. The maximum pressure is smaller than that obtained for one pad foil bearing ($\tilde{p}_m \sim 1.44$) and is observed at the centerline of the bearing width. The maximum pressure in nearly the same for the two cases (*i.e.* $\phi_0 = 0°$ and $\phi_0 = -90°$) whit a slightly higher value in the second case. For the three pads bearings, again, the shape of the pressure profile is altered. The shape is more complex since ambient pressure is imposed at the beginning of each pad. However, the same interpretations for the two pads configuration are still applicable. The maximum pressure is slightly smaller. Two different values for two minimum film thickness angular position are considered (*i.e.* $\phi_0 = -180°$ and $\phi_0 = 0°$). The corresponding pressure and film thickness are shown in Fig. 6.6 and Fig. 6.7 respectively. The maximum pressure value is about $\tilde{p}_m = 1.41$ for the first case. In the second case, the pressure peak is slightly higher.

The effect of the loading angle on the bearing load capacity can be shown in Fig. 6.1 where results are shown for the three bearings and with two scenarios, ϕ_0 at the start and middle of the bearing pad. It is clear that for one and two pads foil bearings; results show a higher load when ϕ_0 is located in the middle of the pad. This is due to the higher area of the convergent region in this case. This effect is more pronounced at a high eccentricity ratio, particularly for the single pad foil bearing. This effect can be neglected at a low to medium eccentricity ratio, especially for the two pads bearings. For the last configuration (three pad foil bearing), high load capacity is obtained when ϕ_0 is at the start of a given pad (*i.e.* $\phi_0 = -180°$). Note that in the following, results are shown for the three bearing configurations with ϕ_0 in the middle of the corresponding pad.

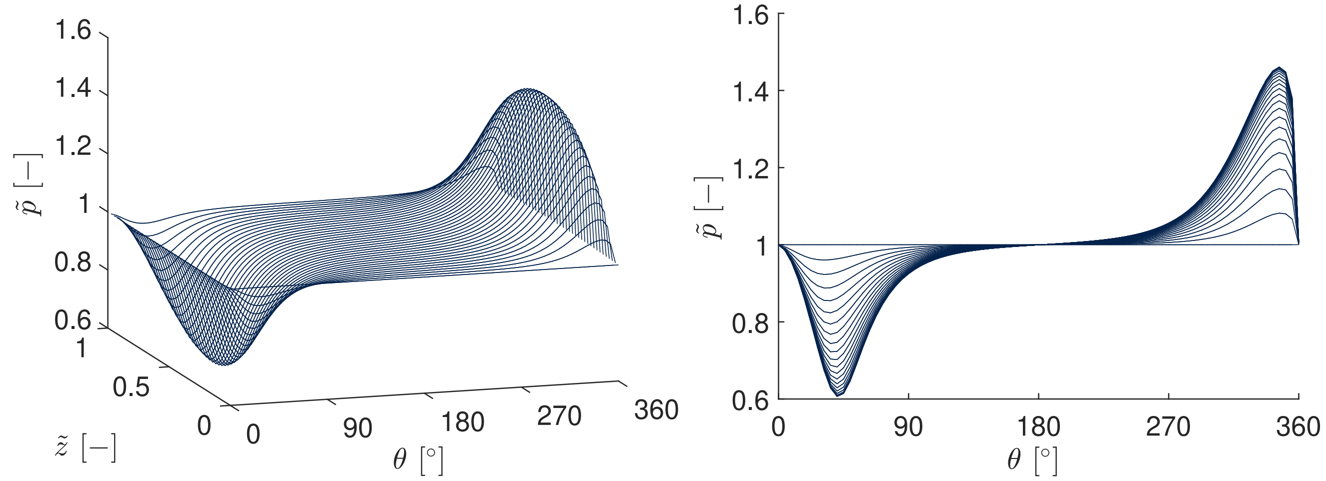

(a) Pressure distribution (2D)

(b) Pressure distribution (side view)

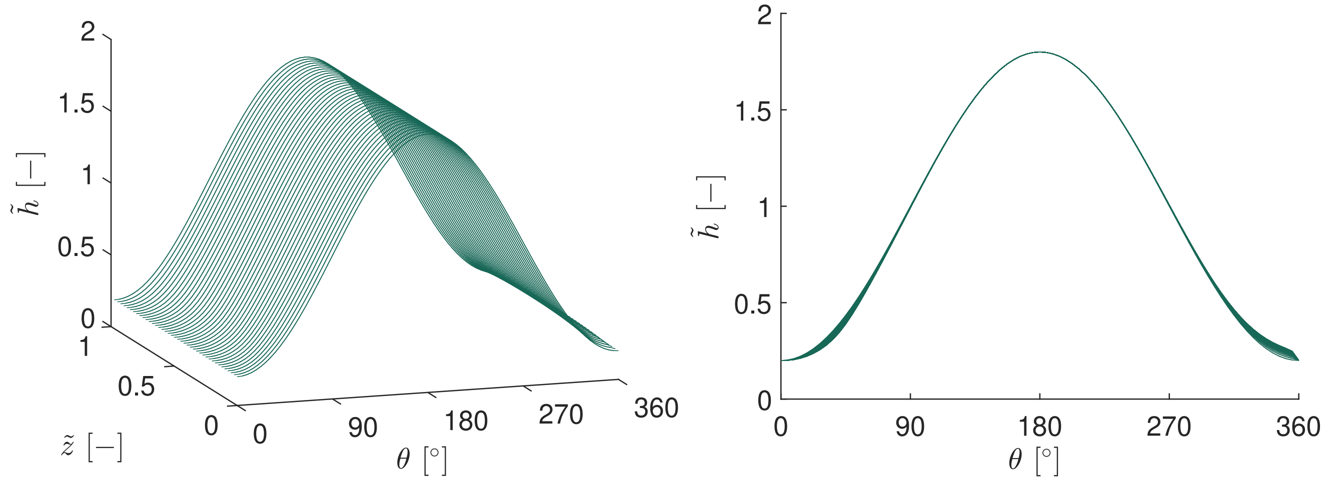

(c) Film thickness (2D)

(d) Film thickness (side view)

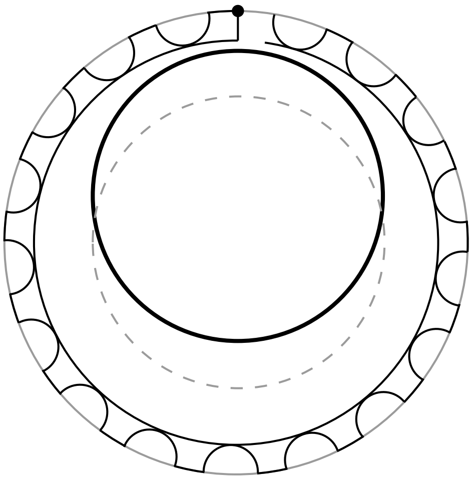

(e) Bearing configuration

Figure 6.2: (a,b) Film pressure and (c,d) Film height for one pad foil bearing running at 100 krpm. The results are obtained with $\varepsilon = 0.8$, $\phi_0 = -180^\circ$, $\theta_l = 0^\circ$ $\Lambda = 0.66$, $S = 0.12$, $L/D = 1/2$.

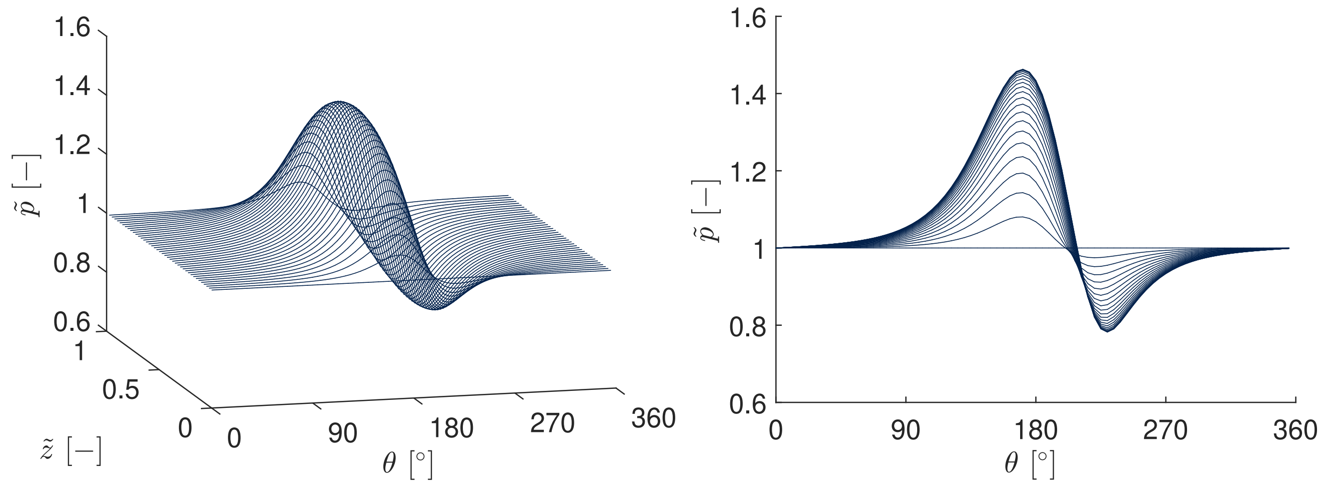

(a) Pressure distribution (2D)

(b) Pressure distribution (side view)

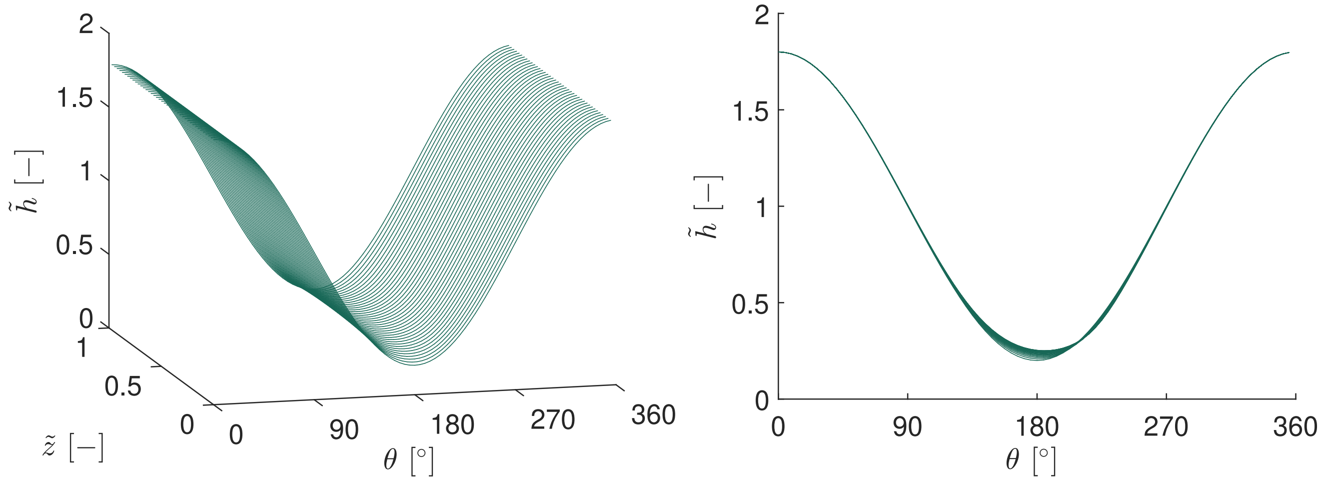

(c) Film thickness (2D)

(d) Film thickness (side view)

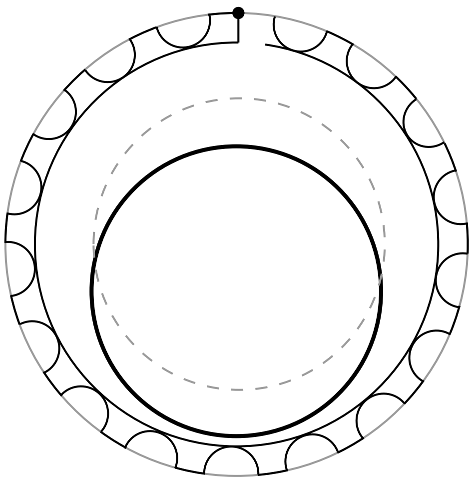

(e) Bearing configuration

Figure 6.3: (a,b) Film pressure and (c,d) Film height for one pad foil bearing running at 100 krpm. The results are obtained with $\varepsilon = 0.8$, $\phi_0 = 0^\circ$, $\theta_l = 0^\circ$ $\mathit{\Lambda} = 0.66$, $S = 0.12$, $L/D = 1/2$.

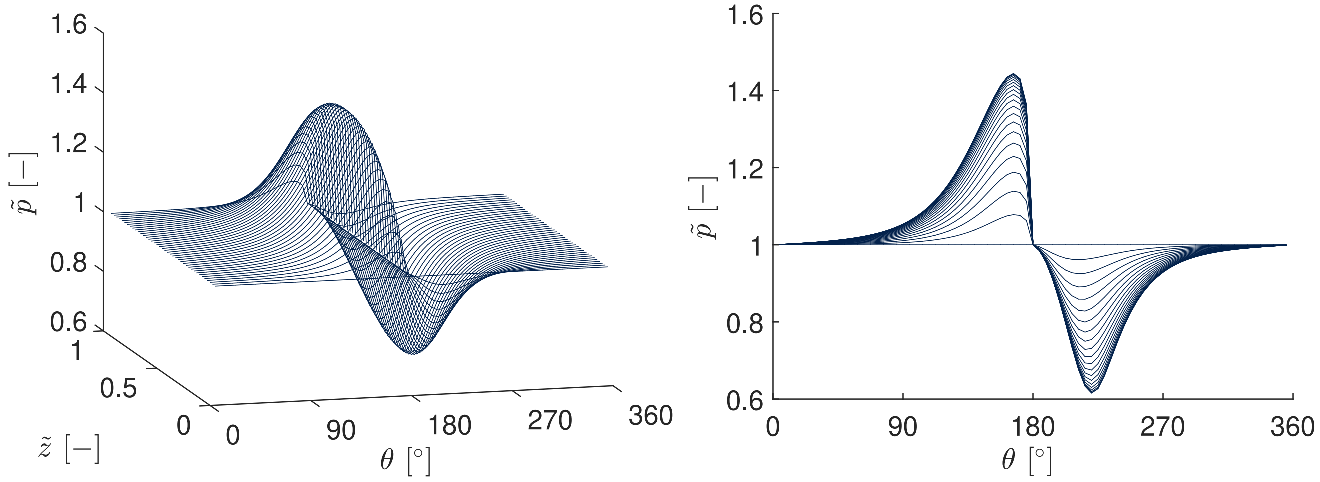

(a) Pressure distribution (2D)

(b) Pressure distribution (side view)

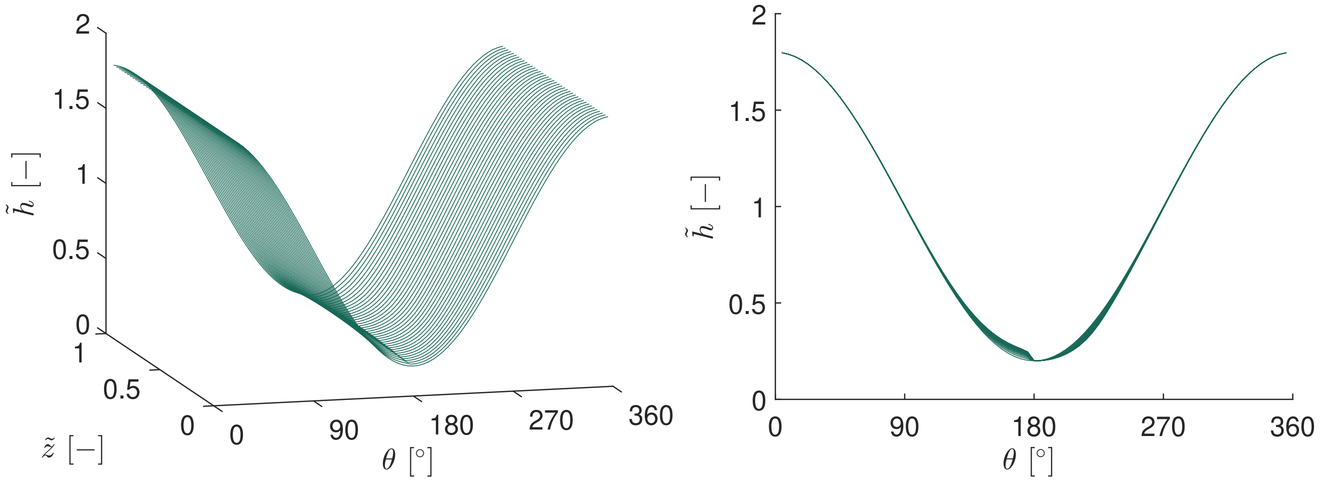

(c) Film thickness (2D)

(d) Film thickness (side view)

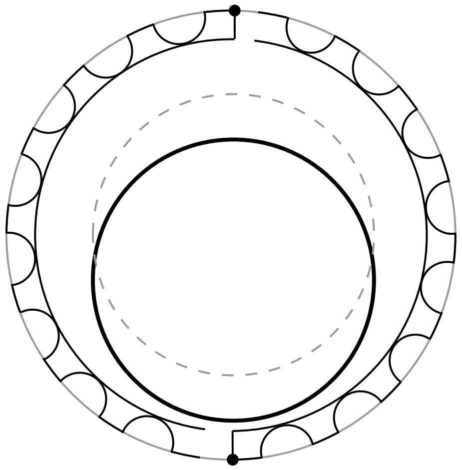

(e) Bearing configuration

Figure 6.4: (a,b) Film pressure and (c,d) Film height for two pads foil bearing running at 100 krpm. The results are obtained with $\varepsilon = 0.8$, $\phi_0 = 0^\circ$, $\theta_l = 0^\circ$ $\Lambda = 0.66$, $S = 0.12$, $L/D = 1/2$..

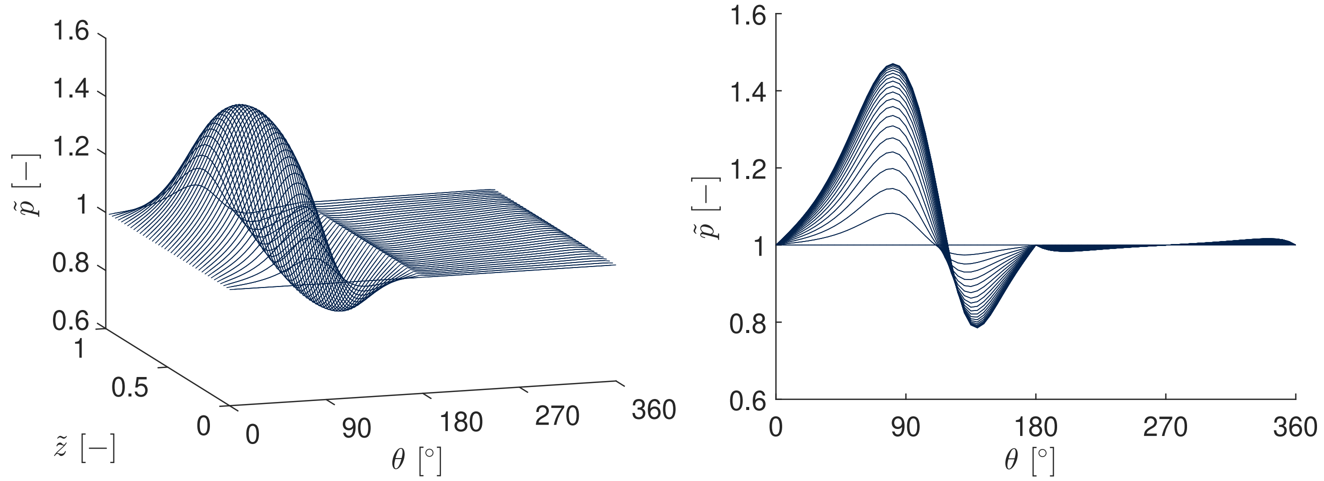

(a) Pressure distribution (2D)

(b) Pressure distribution (side view)

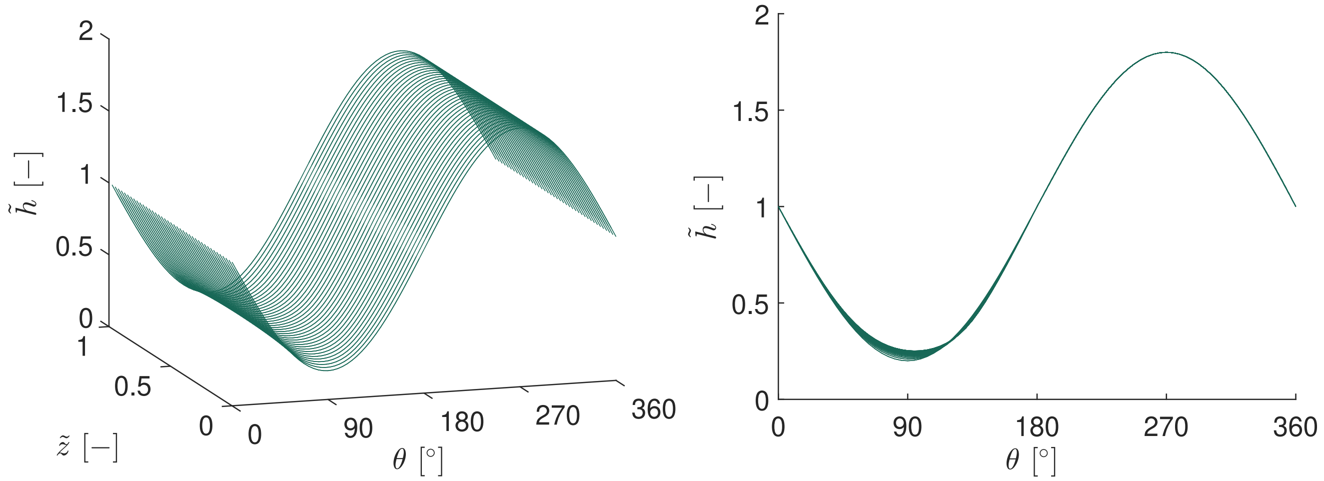

(c) Film thickness (2D)

(d) Film thickness (side view)

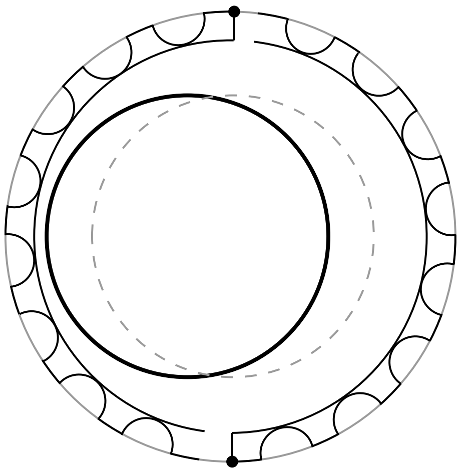

(e) Bearing configuration

Figure 6.5: (a,b) Film pressure and (c,d) Film height for two pads foil bearing running at 100 krpm. The results are obtained with $\varepsilon = 0.8$, $\phi_0 = -90°$, $\theta_l = 0°$ $\Lambda = 0.66$, $S = 0.12$, $L/D = 1/2$.

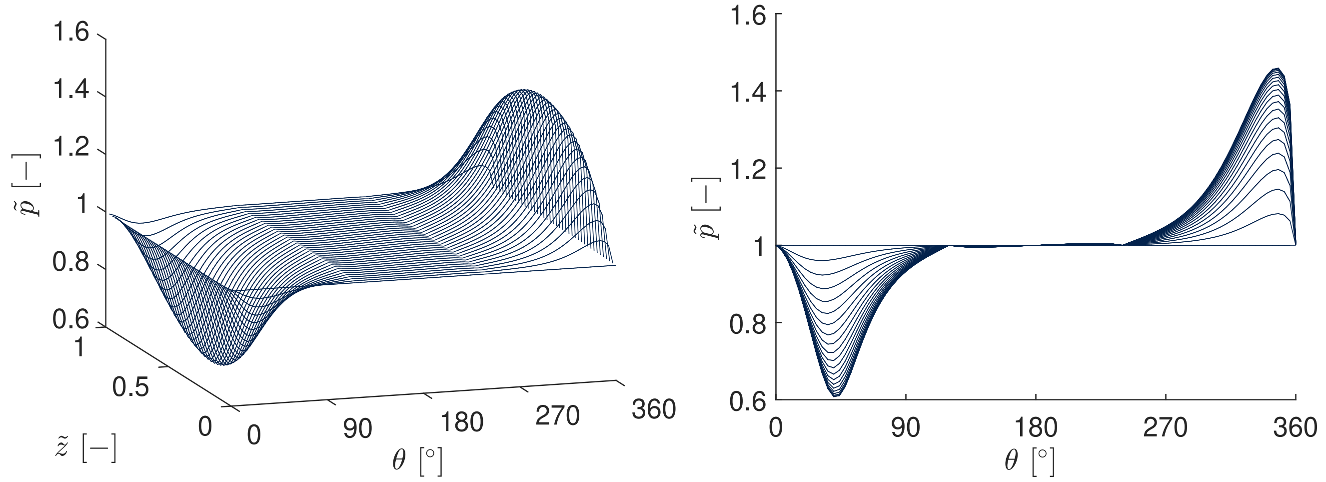

(a) Pressure distribution (2D) (b) Pressure distribution (side view)

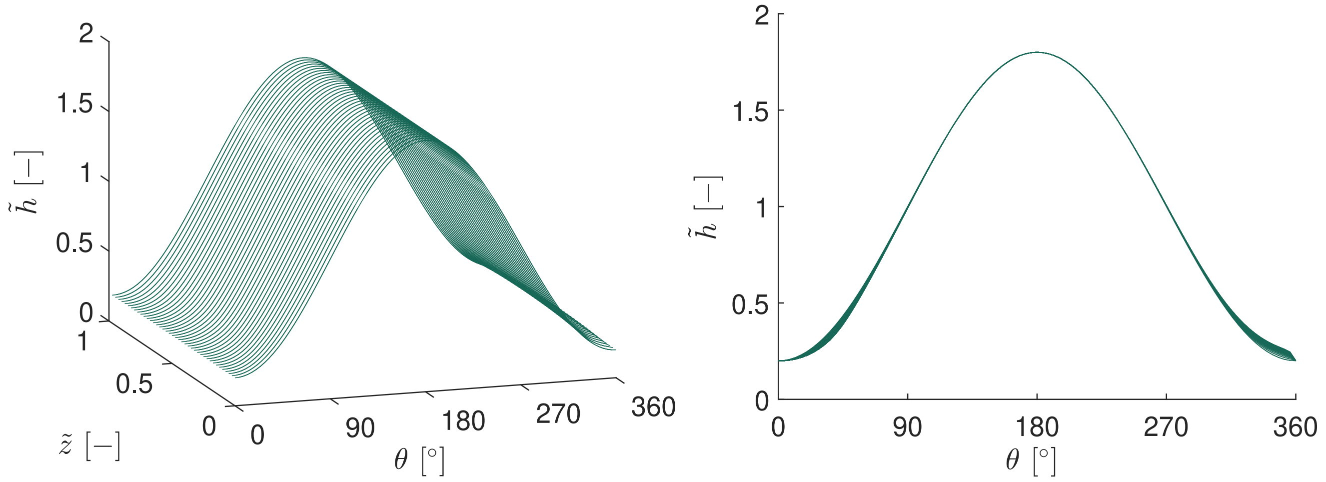

(c) Film thickness (2D) (d) Film thickness (side view)

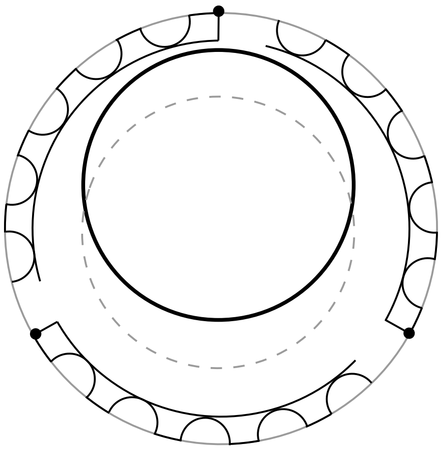

(e) Bearing configuration

Figure 6.6: (a,b) Film pressure and (c,d) Film height for three pads foil bearing running at 100 krpm. The results are obtained with $\varepsilon = 0.8$, $\phi_0 = -180^\circ$, $\theta_l = 0^\circ$ $\Lambda = 0.66$, $S = 0.12$, $L/D = 1/2$.

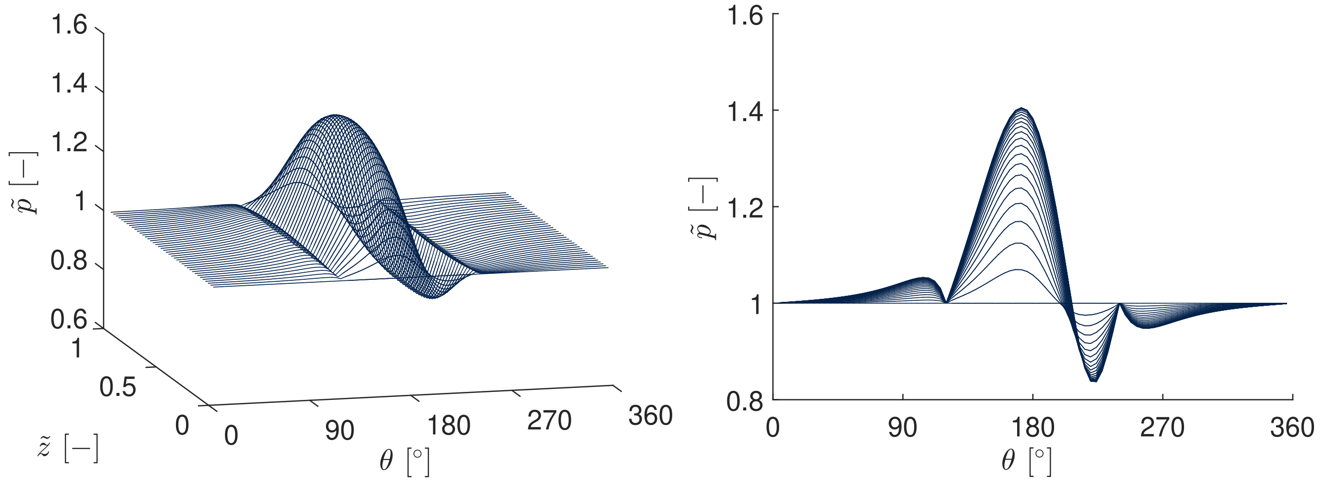

(a) Pressure distribution (2D)

(b) Pressure distribution (side view)

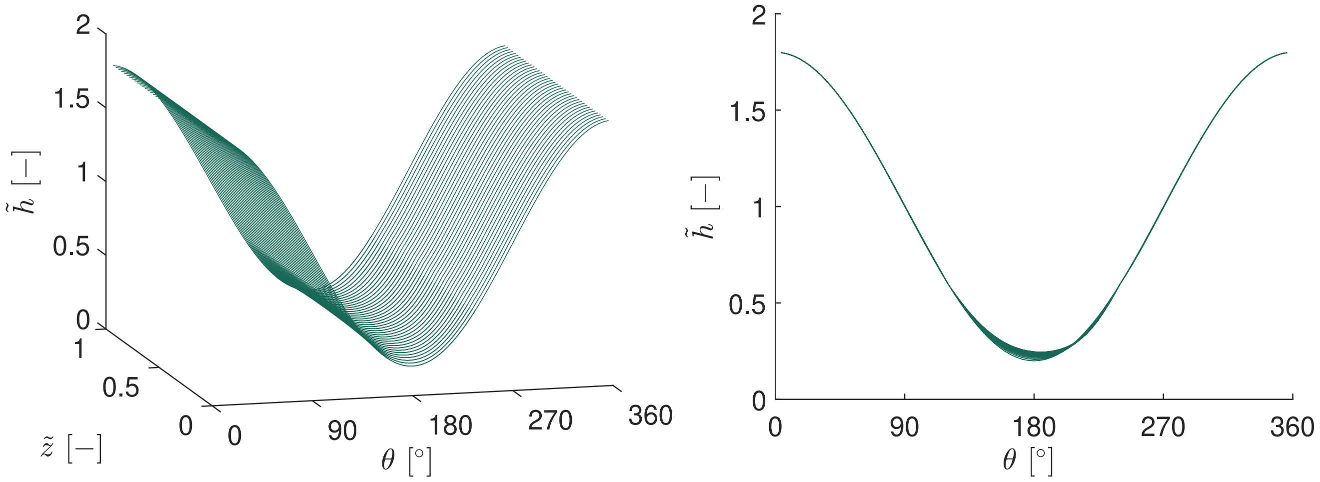

(c) Film thickness (2D)

(d) Film thickness (side view)

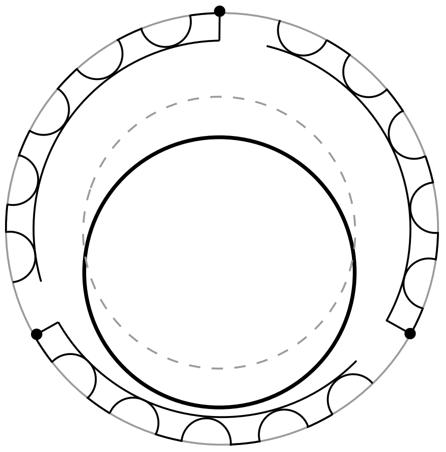

(e) Bearing configuration

Figure 6.7: (a,b) Film pressure and (c,d) Film height for three pads foil bearing running at 100 krpm. The results are obtained with $\varepsilon = 0.8$, $\phi_0 = 0^\circ$, $\theta_l = 0^\circ$ $\mathit{\Lambda} = 0.66$, $S = 0.12$, $L/D = 1/2$.

6.2 Bearing number

The bearing number is a parameter representing paramount importance in gas film lubrication. It regroups the effect of operating conditions (rotation speed ω, viscosity μ, reference pressure p_a) and bearings geometry (shaft diameter D, bearing radial clearance C) through $\Lambda = 6\mu\omega/p_a(R/C)^2$. Under given geometrical characteristics, the bearing number can vary for different performance characteristics and vice versa. Fig. 6.8 shows the effect of bearing number on the load capacity for different bearing configurations. Observing the aforementioned figure, it is found that as the eccentricity ratio increases, the load capacity increases since the film thickness decreases. A decreased film thickness tends to compress air in the fluid film, thereby increasing the load capacity. As shown in Fig. 6.8 the trend is the same in each case. The load increases with increasing eccentricity ratio, and this is for all bearings configurations. Moreover, when Λ increases, load capacity increases. Indeed as the bearing number is proportional to the shaft rotation speed, more fluid is dragged at high bearing numbers, which generates more pressure and allows higher loads to be supported by the bearing. This behaviour is the same for each bearing configuration. However, for a given bearing number, comparisons show a lower load for multiple pad GFB compared to the single pad.

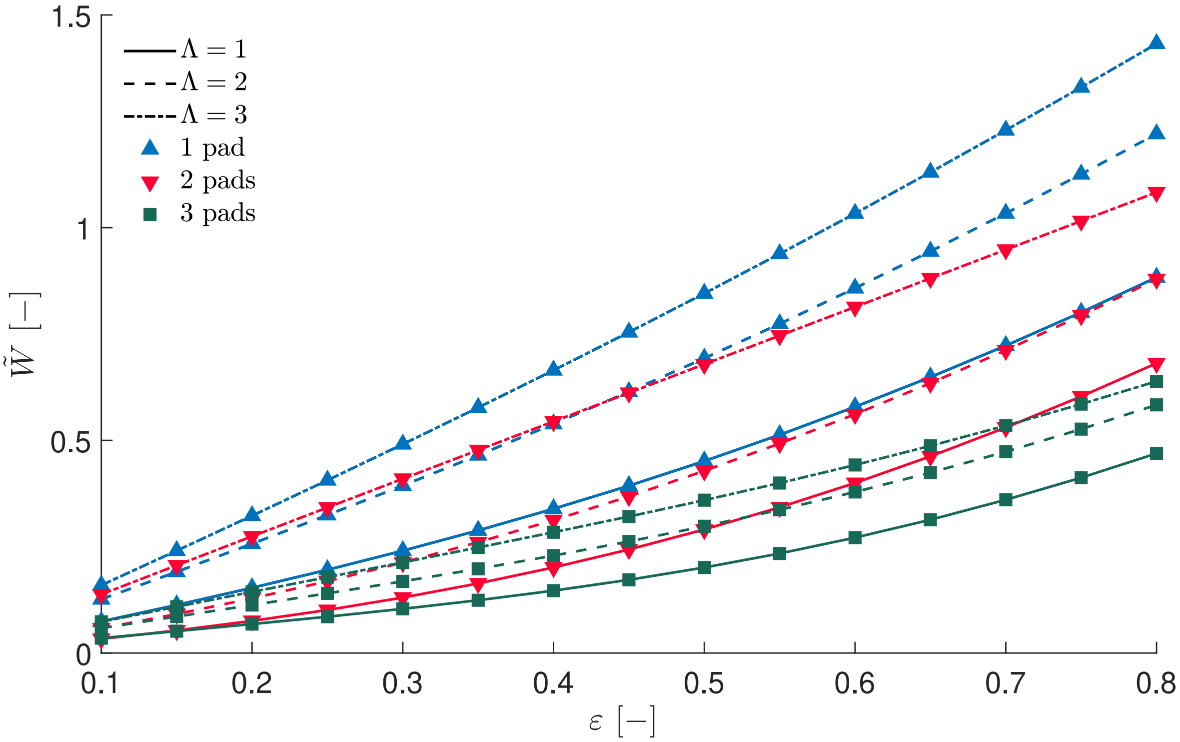

Figure 6.8: Effect of bearing number on Load capacity for different bearing geometries, one pad (in blue ▲), two pads (in red ▼) and three pads (in green ■). The results are obtained with $S = L/D = 1$ and $\Lambda = 1$ (solid line), $\Lambda = 2$ (dashed line) and $\Lambda = 3$ (dotted line).

6.3 Bearing compliance

Bearing compliance/coefficient reflects the rigidity of the compliant structure, including its material properties (Young's modulus E, Poisson ratio ν) and geometrical parameters (bump thickness t_b, bump pitch S_B, bump length l_b). Analyzing Fig. 6.9, it can be seen that increasing the compliance factor reduces the load capacity for all bearings configurations. Indeed, the deflection of the compliant foil structure is reduced for an increasing compliance factor, thus decreasing the load capacity. Once again, one pad foil bearing shows improvement over multiple pads in load capacity for a given compliance factor.

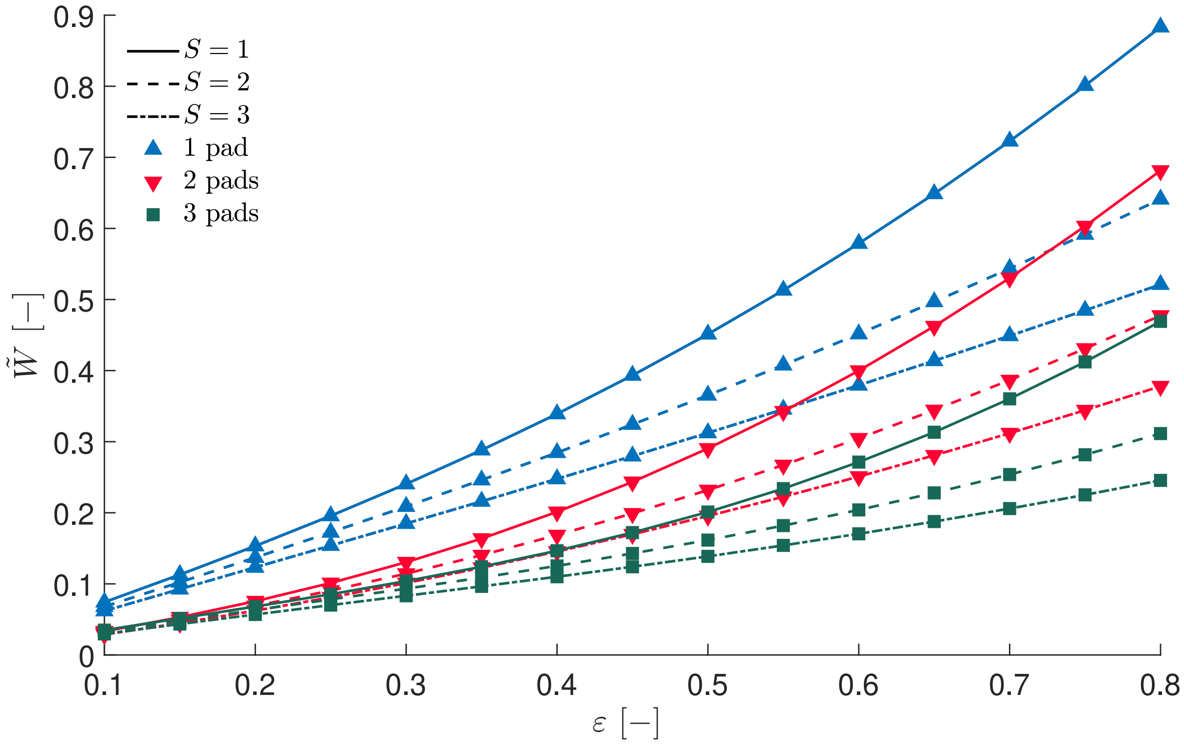

Figure 6.9: Effect of foil compliance on Load capacity for different bearing geometries, one pad (in blue ▲), two pads (in red ▼) and three pads (in green ■). The results are obtained with $\Lambda = L/D = 1$ and $S = 1$ (solid line), $S = 2$ (dashed line) and $S = 3$ (dotted line).

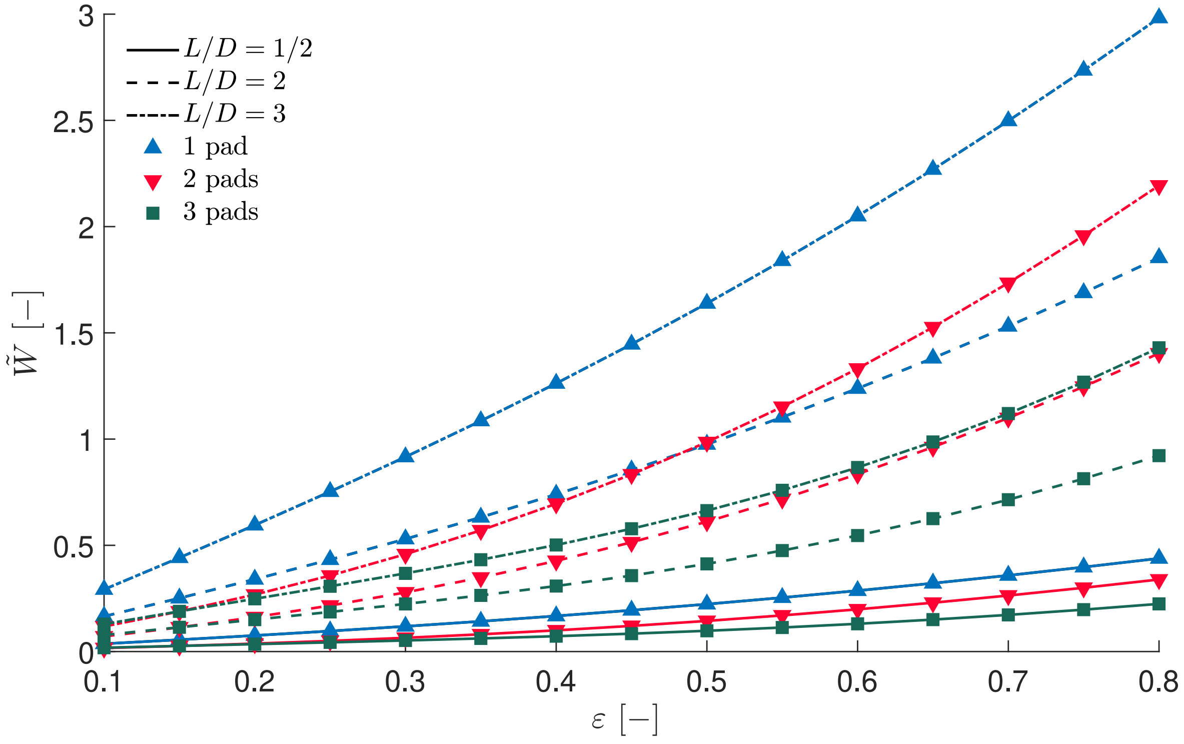

Figure 6.10: Effect of length-to-diameter ratio on Load capacity for different bearing geometries, one pad (in blue ▲), two pads (in red ▼) and three pads (in green ■). The results are obtained with $\Lambda = S = 1$ and $L/D = 1/2$ (solid line), $L/D = 2$ (dashed line) and $L/D = 3$ (dotted line).

6.4 Length-to-diameter ratio

Fig. 6.10 depict the load capacity versus eccentricity ratio for different values of L/D. It is found that, as the length to diameter ratio increases, bearing load capacity increases for a given eccentricity ratio. The length to diameter ratio being proportional to the size of the bearing; as the size increases, the pressure distribution is extended over a larger area, increasing the load capacity. The pressure peak takes higher values for higher L/D. The load is increased nearly by a factor of 2 when L/D is doubled for all bearing configurations. It can also be noted that single pad foil bearing shows larger load capacity for a given bearing size compared to other bearing configurations.

6.5 Stiffness model

As discussed in section 3.2, three existing stiffness models based on analytical expressions for the stiffness are used. Tab. 6.1 summarises the results concerning the load-carrying capacity for the three models. The results are shown for different eccentricity ratios ε varying from 0.1 to 0.8. It can be noted that the load capacity is very similar for the three models. A small difference in results is observed between Iordanoff, and other models are observed at high eccentricity ratios. However, this difference remains minimal. Note that the results using Wallowit and Larsen models are quite the same, meaning that the effect of including the top foil stiffness in Larsen model is not indispensable. Moreover, in Tab. 6.1, the friction coefficient μ_f has been set to 0.05 based on other authors [54, 65]. The effect of this last on the load capacity is shown in Fig. 6.11 where four values of friction coefficient has been used (*i.e.* $\mu_f \in \{0,\ 0.1,\ 0.2,\ 0.3\}$). These values are mainly used in literature.

It can be seen that at low eccentricity ratios, the results coincide whatever the value of μ_f. However, at high eccentricity ratios, a slight difference is observed where an increase in the friction coefficient leads to an increase in the load capacity since the bump compliance factor is decreased and foil deflection is increased. This effect is more pronounced when going from medium to high value of ε.

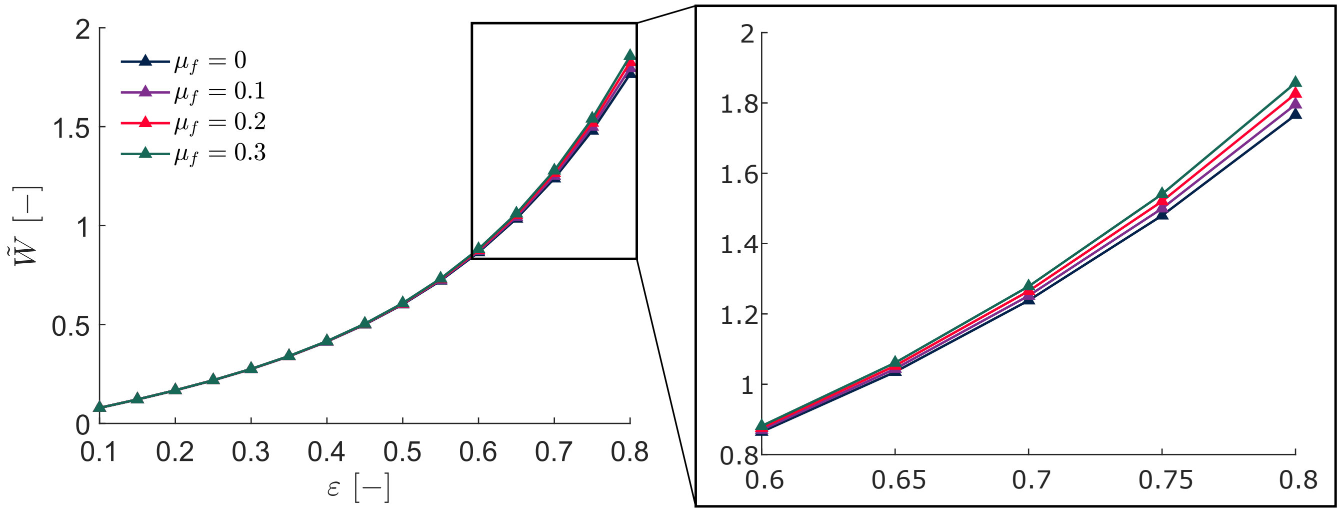

Figure 6.11: Load capacity versus eccentricity ratio for varying coefficient of friction in Iordanoff model.

	Eccentricity ratio ε							
	0.1	0.2	0.3	0.4	0.5	0.6	0.7	0.8
Wallowit	0.0786	0.1673	0.2747	0.4135	0.6018	0.8657	1.2408	1.7718
Iordnaoff	0.0786	0.1673	0.2748	0.4138	0.6025	0.8674	1.2448	1.7805
Larsen	0.0786	0.1673	0.2747	0.4135	0.6018	0.8657	1.2409	1.7718

Table 6.1: Load capacity with eccentricity ratio for different stiffness models. The results are obtained for a single pad foil bearing with $\Lambda = L/D = 1$, $t_b = t_t = 0.1$ mm, $E_b = E_t = 1.96$ GPa, $\nu_b = \nu_t = 0.3$, $l_b = 0.852$ mm, $S_b = 2.170$ mm, $\theta_b = 91.84°$ and friction coefficient $\mu_f = 0.05$.

6.6 Inlet slope

In this section, bearings with inlet slope are investigated. This consists of a slight retraction of the pad towards the bearing sleeve at the attachment points, where both bump and top foil are pinned to the bearing housing. It has been shown to improve stability by generating a converging gap between the top foil and the shaft. It also eliminates the risk of having rotor-foil contact in the attachment points, which are generally less compliant than the rest of the pad surface [54]. A schematic of such configuration is given in Fig. 3.1b where the rigid contribution of the film height is given according to Eq. (3.7) [65]. To do so, two values of inlet slope extend θ_s and inlet slope height $\tilde{h}_s$ are considered. Tab. 6.2 report the load capacity for different values θ_s, $\tilde{h}_s$ and eccentricity ratio ε. The results are shown for segmented bearings with a different number of pads N_p. It can be observed that adding inlet slope height has an impact on increasing the bearing load capacity for the single foil bearing, especially at low eccentricity ratios. For 2-pads and 3-pads foil bearings, this load increase at low eccentricity is more pronounced as the number of pads N_p increases. However, load capacity is decreased for 2-pads bearings at high eccentricity ratios. This effect is more pronounced for higher values of inlet slope angle and inlet slope height. Similarly, at high eccentricity ratio,*i.e.* $\varepsilon = 0.8$, the effect of height slope is nearly negligible for 1-pads bearing. For a given $\tilde{h}_s$, by extending the inlet slope angle θ_s, the load capacity is improved or decreased depending on the bearing configuration and the eccentricity ratio. Note that this reduction of load capacity at high eccentricity ratios could be neglected since the reduction is -2.33% at its maximum value. This is not the case with the 2-pads configuration, where the reduction can reach -14.51%.

		1 pads FB				2 pads FB				3 pad FB			
θ_s	$\tilde{h}_s$	0.2	0.4	0.6	0.8	0.2	0.4	0.6	0.8	0.2	0.4	0.6	0.8
30°	2	+10.29	+1.54	+0.22	±0.00	+32.24	+8.50	−0.36	−3.39	+38.40	+22.99	+14.35	+8.76
	4	+10.03	+1.51	+0.24	+0.04	+20.02	+0.48	−6.33	−7.98	+30.00	+13.68	+4.52	−0.38
60°	2	+25.32	+4.71	+1.04	+0.22	+31.81	+9.24	−0.85	−5.19	+43.18	+33.38	+21.53	+11.82
	4	+25.67	+4.37	+1.02	+0.22	+12.97	−5.94	−12.72	−14.51	+23.93	+16.03	+5.27	−2.33

Table 6.2: Change in load capacity with inlet slope with respect to the standard configuration (without inlet slope) in %. The results are obtained with $\Lambda = S = L/D = 1$. Results are shown for two different values of inlet slope extend θ_s and inlet slope height $\tilde{h}_s$ for different eccentricity ratio $\varepsilon \in \{0.2,\ 0.4,\ 0.6,\ 0.8\}$ and different bearings geometries.

Chapter 7

Industrial Application

This chapter is dedicated to applying the numerical method performed in the frame of this work to the bearing configuration used by Mitis SA for their turbogenerators. The tested bearing is a two pads foil bearing manufactured by Omega Dot, a small British R&D company specialising in bespoke and innovative engineering solutions for the turbomachinery market. The bearing has a simple design consisting on a bump layer (Inconel X750) topped by a top foil (Inconel X750). The top foil is heat treated and coated with a skinny layer of Teflon. Both bump and top foils are pinned together to the bearing sleeve at their leading edges and free at the other extremity. The attachment to the bearing sleeve is based on a simple technique in which the foil flaps are bent after being inserted through two holes in the bearing housing. The shaft, made up of Stainless Steel 316L, rotates in the direction from the trailing edge (free end) to the leading edge (pinned end). The design parameters of the tested bearing are reported in Tab. 7.1. All The results are obtained in the case where $\phi_0 = 0°$, since the effect of the loading angle can be neglected for the two pad GFB.

Bearing configuration					
Bearing length, L	24	mm	Number of pads, N_p	2	/
Bearing diameter, D	24	mm	First pad leading edge, θ_l	0	deg
Radial clearance, C	50	µm	First pad trailing edge, θ_t	180	deg
Fluid properties					
Ambient pressure, p_a	101325	Pa	Dynamic viscosity, μ	$2.934\,.10^{-5}$	N.s.m^{-2}
Bump foil properties					
Bump foil thickness, t_b	0.10	mm	Bump foil Young's modulus, E_b	196	GPa
Bump pitch, s_b	2.17	mm	Bump foil Poisson ratio, ν_b	0.30	/
Bump half length, l_b	0.852	mm	Density, ρ_b	8.28	g.cm^{-3}
Bump half angle, θ_b	45.92	deg	Friction coefficient, μ_f	0.05	/
Bump height, h_b	0.248	mm	Bump radius, R_b	1.186	mm
Top foil properties					
Top foil thickness, t_t	101.6	mm	Top foil Young's modulus, E_t	196	GPa
Density, ρ_b	8.28	g.cm^{-3}	Top foil Poisson ratio, ν_t	0.30	/

Table 7.1: Geometry, material properties and operating conditions of the Omega Dot bearings. The material properties are taken at 300°C.

The operating conditions for the bearing depend on the position of this last inside the turbogenerator. Since two main configurations are tested in Mitis SA (see Fig. 2.1), the operating temperature could be different. Moreover, Operating temperature varies axially through the bearing width. The numerical code is based on the hypothesis of isothermal surface. Therefore, to study the effect of temperature variation, results are shown for operating temperature in the range of 200° to 400°. These temperatures correspond to the extremes of minimum and maximum temperature observed during experimental tests. Moreover, the nominal rotation speed of the shaft is about $110,000$ rpm. For more generality, results are shown for different rotation speed (*i.e.* $\omega \in [40,000;\, 110,000]$ rpm).

7.1 Rotation speed

Fig. 7.1 depict the load capacity, attitude angle and maximum pressure versus shaft rotation speed. Both load capacity and maximum pressure peak increase with increasing rotation speed and thus for all eccentricity ratios. Nearly linear behaviour is observed with a more significant slope for higher eccentricity values. The pressure increases with the eccentricity ratio for a given rotation speed, resulting in a higher load. More precisely, the load is multiplied by a factor of two when the eccentricity ratio is increased by 0.2. On the other hand, the reverse behaviour is observed for the attitude angle, where a slight linear decrease with rotation speed is more pronounced for lower values of eccentricity ratio.

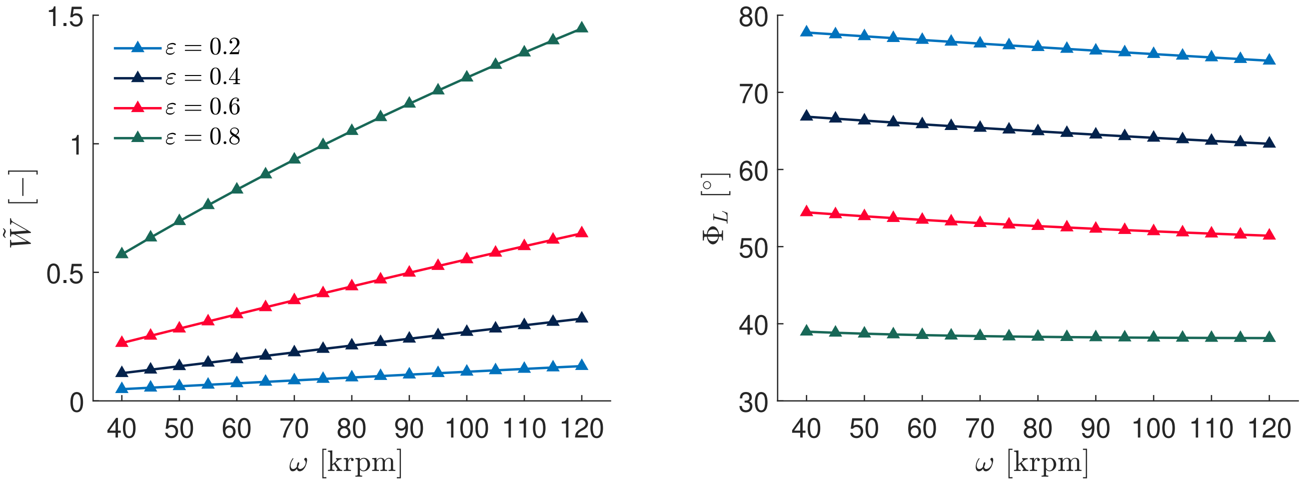

(a) Load capacity (b) Attitude angle

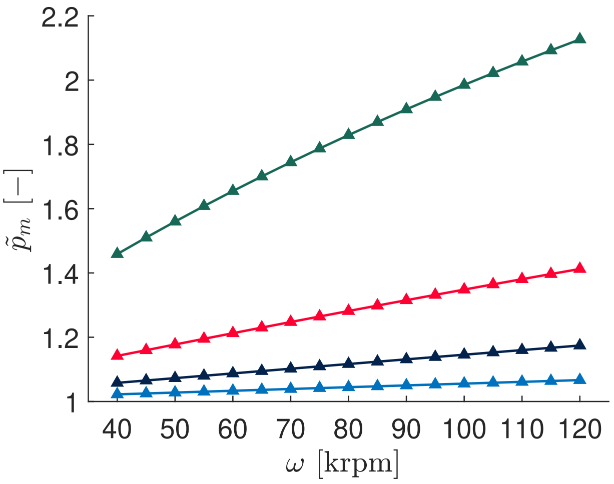

(c) Maximum pressure

Figure 7.1: (a) Load, (b) Attitude angle and (c) Maximum pressure versus rotation speed for different values of eccentricity ratio. The results are obtained with the design parameters in Tab. 7.1 at $T = 300^\circ$ C.

7.2 Temperature

The effect of temperature on load capacity, attitude angle and maximum pressure is shown in Fig. 7.2 where all the simulations are performed for the nominal rotation speed $110,000$ rpm. The results show a small increase in the maximum pressure with temperature and, therefore, an increase in the bearing load-carrying capacity. Despite that, the slope of the different curves is more important for a higher eccentricity ratio, the effect of temperature on the load is relatively small and can be negligible, especially for low values of eccentricity ratio. Concerning the attitude angle, a minimal decrease of this last with increasing temperature is observed. For a given eccentricity ratio, the curves are nearly constant. Consequently, the attitude angle can be taken constantly so that the temperature effect can be discarded.

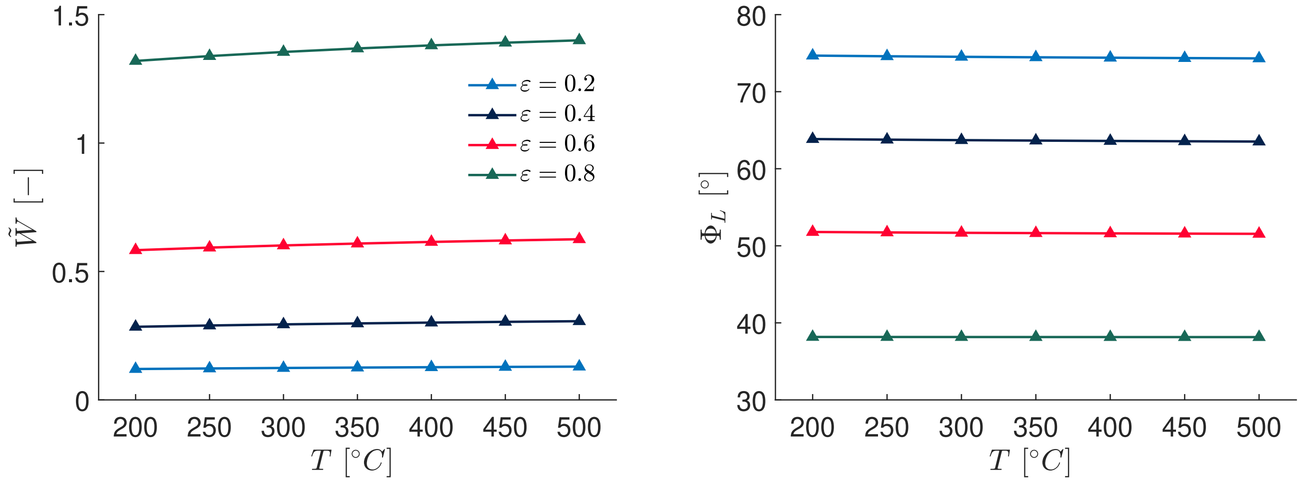

(a) Load capacity

(b) Attitude angle

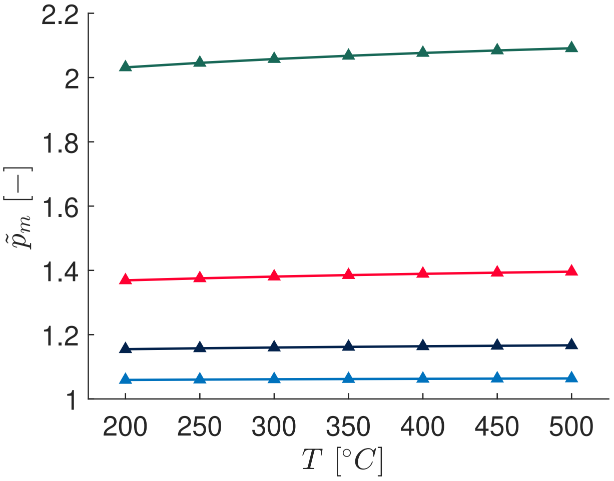

(c) Maximum pressure

Figure 7.2: (a) Load, (b) Attitude angle and (c) Maximum pressure versus temperature for different values of eccentricity ratio. The results are obtained with the design parameters in Tab. 7.1 at $\omega = 110,000$ rpm.

7.3 Clearance Axial Variation

Numerical simulations of the turbogenerator used in Mitis SA have shown a variation of clearance through the bearing's width. Depending on the material used for the shaft and/or bearing sleeve, a different percentage of variation is observed. This phenomenon is due to the material expansion/contraction due to temperature variation across the bearing's width. Tab. 7.2 gives the percentage of predicted clearance variation with different materials.

Shaft Sleeve	Inconel718	W303
Inox316L	+2.16%	+3.53%
W303	−1.76%	±0.00%

Table 7.2: Axial clearance variation due to temperature gradient from one bearing edge to the other.

In the following, one will denote the different cases corresponding to Tab. 7.2 as follows: case 1 (+2.16%), case 2 (+3.53%), case 3 (−1.76%) and case 4 (±0.00%). Fig. 7.3 shows the load carrying capacity and attitude angle versus eccentricity ratio for the abovementioned cases. It can be seen in Fig. 7.3a the highest load capacity is observed for case 3. This is because the radial clearance decreases over the bearing width and thus decreases the film thickness, increasing the pressure and the load capacity. Conversely, an increase of the clearance results in a larger film height and thus a smaller value of load capacity. Concerning the attitude angle, it decreases with an increasing eccentricity ratio. The pressure peak is located more and more near the middle of the domain (*i.e.* at $\theta = 180°$). Consequently, for a given eccentricity ratio, the smallest value is observed for the case 2 where the percentage of axial clearance variation is the highest (*i.e.* radial clearance that increases across the bearing width). This effect is shown in Fig. 7.3b.

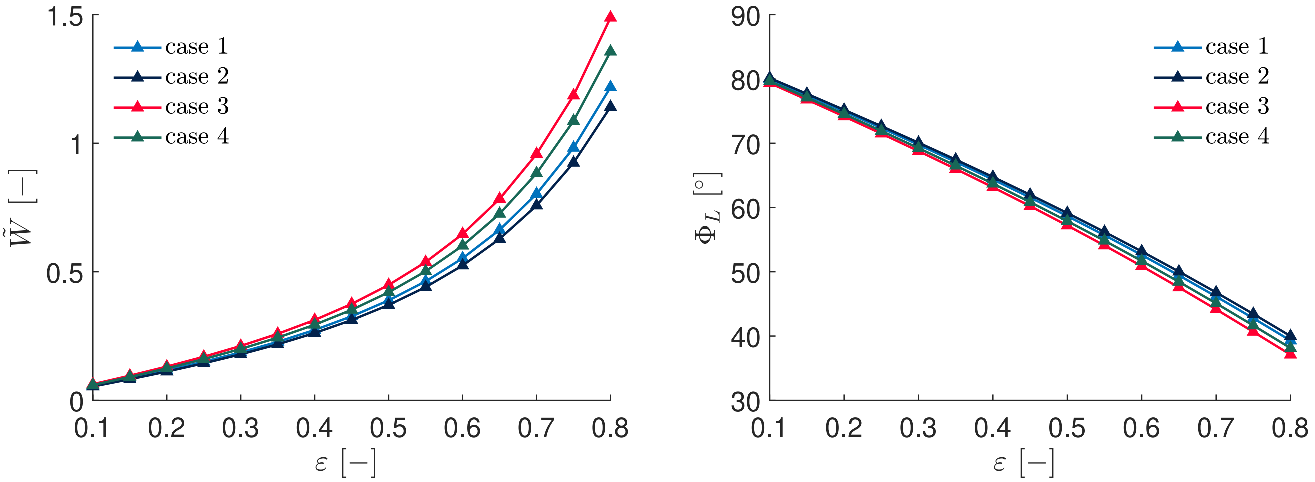

(a) Load capacity (b) Attitude angle

Figure 7.3: (a) Load and (b) Attitude angle versus eccentricity ratio. The results are obtained with the design parameters in Tab. 7.1 at $\omega = 110,000$ rpm and $T = 300°$ C. The different cases corresponds to the percentages of variation presented in Tab. 7.2 with case 1 (+2.16%), case 2 (+3.53%), case 3 (−1.76%) and case 4 (±0.00%).

Fig. 7.4 depicts the pressure distribution for the above mentioned cases. The results are shown at different axial position (*i.e.* $\tilde{z} = z/R = 0.5,\ 1,\ 1.5$). Similar interpretation as previously, the pressure peak increase with decreasing pressure film so that higher load capacity is obtained for the case 3.

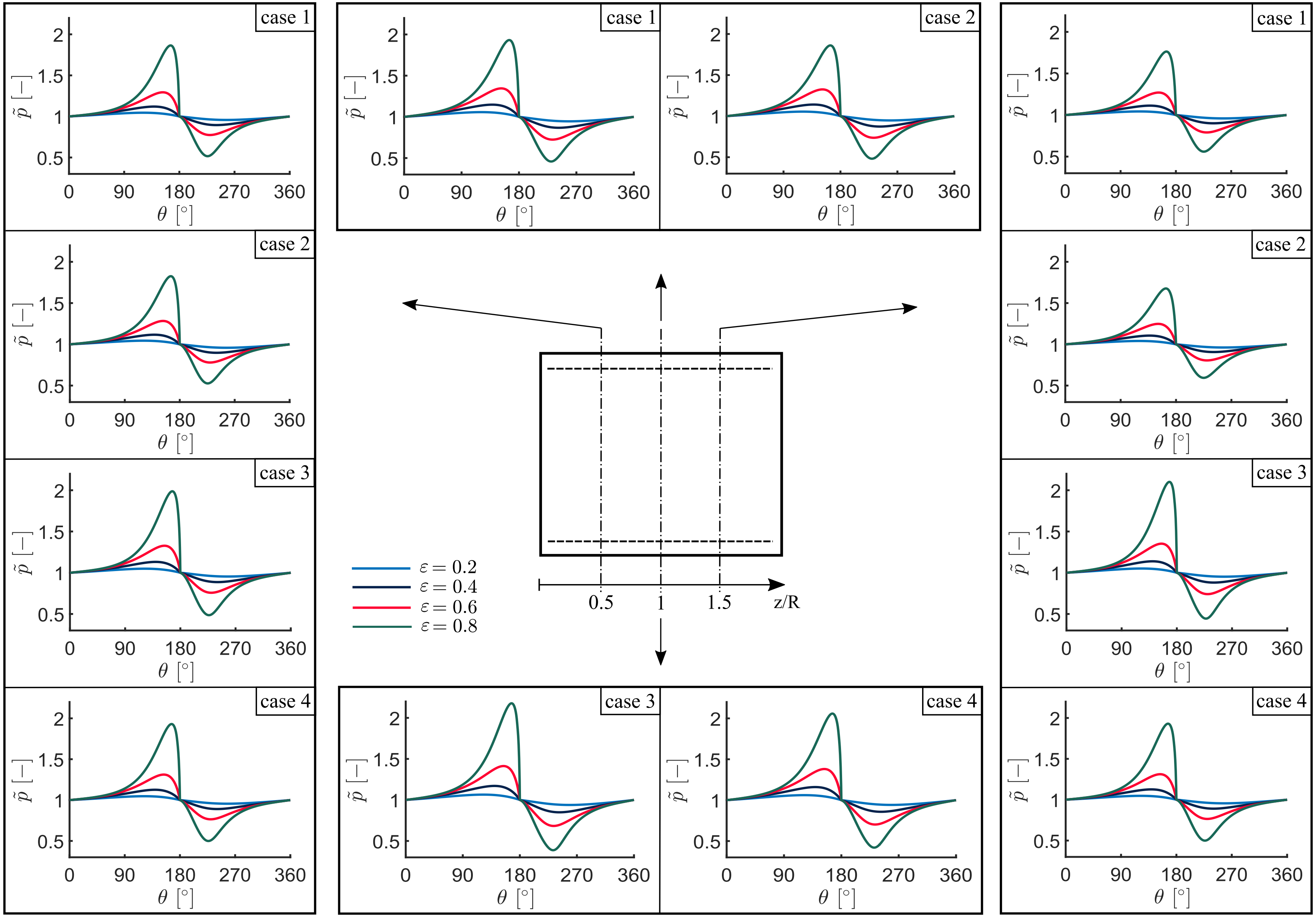

Figure 7.4: Effect of clearance axial variation on pressure film. The results are obtained with the design parameters in Tab. 7.1 at $\omega = 110{,}000$ rpm and $T = 300°$ C. The different cases corresponds to the percentages of variation presented in Tab. 7.2 with case 1 (+2.16%), case 2 (+3.53%), case 3 (−1.76%) and case 4 (±0.00%).

Conclusion and Perspectives

7.4 Thesis summary

The present work focused mainly on the theoretical aspects of GFB modelling and particularly on the behaviour of the lubrication gas film. This paved the way for deriving the two-dimensional Reynolds equation governing the fluid film pressure distribution inside the bearing. The equation has been derived under the assumptions of Newtonian and isoviscous fluid, laminar flow, isothermal surfaces and steady-state conditions. The work has comprised the development and implementation of a numerical recipe using the Discontinuous Galerkin finite element Method (DG-FEM). The numerical aspect of the hyperbolic-elliptic problem has been addressed with the implementation of specific approaches. First, upwind flux has been proposed for the convective formulation, and then an incomplete internal penalty method (IIPM) has been considered for evaluating the diffusive interface flux. Particular attention has been given to the penalty term involved in the IIPM. Newton-Raphson method has been used to solve the nonlinear equation. The residual and the inverse of the Jacobian have been computed using direct solver, which itself is based upon the LU factorization technique. Such iterator is pre-implemented in ForDGe, an immersed boundary, and in turn, Adaptive Mech Refinement (AMR) on multiple order Cartesian grids, still under development at ULiège.

The modelling of the foil structure is built based upon existing models. Three analytical expressions based on static stiffness have been used to estimate the foil structure flexibility. The coupling between structural and fluid parts has been done at the level of the film thickness using the Simple Elastic Foundation Model (SEFM). The validity of the analysis and numerical code has been assessed by comparing predictions to experimental and/or numerical published data. Perfect matching between predictions and analytical solutions for infinitely long journal rigid bearings has been observed. Good agreements with numerical solutions have been reported for foil bearings with a small overestimation of the load capacity at high eccentricity ratios. Moreover, the minimum film thickness and attitude angle versus load have been compared to the experimental results provided by Ruscitto. Significant discrepancy at low capacity has been observed. The main reason seems to be the fabrication inaccuracy (*i.e.* a lack of conformity between the arc radius of the bump layer and the top foil). The smallest predicted average film thickness reported was about 11 μm which, if exceeded, may result in singular problem, leading to a code crash. Finally, very good matching with numerical results for the pressure distribution has been reported.

The impact of design parameters on the bearing load capacity has been shown for three bearings configurations with single, two and three pads. The main results are the followings:

(i). The bearing load capacity increases with eccentricity ratio due to the decrease of the film height, and this is for all the bearings configurations. Moreover, load capacity decreases with an increasing number of pads so that a higher load can be obtained with the single pad bearing.

(ii). Two different scenarios considering the loading angle ϕ_0 at the start and middle of the pad of the corresponding bearing were investigated. Results showed an impact on the pressure profile and thus the bearing load capacity. At low to medium eccentricity ratio, this effect can be neglected, especially for two pads foil bearing.

(iii). Increasing the bearing number leads to an increase in the load capacity since more fluid is dragged in this case which generates more pressure and allows a higher load to be supported by the bearing. The behaviour is the same for each bearing configuration.

(iv). Increasing the compliance factor reduces the load capacity. This is due to the reduction of the deflection of the compliant foil structure, which results in a lower load.

(v). The length to diameter ratio being proportional to the size of the bearing; as the size increases, the pressure distribution is extended over a larger area, increasing the load capacity.

(vi). With the three stiffness models considered, Wallowit and Larsen showed nearly the same results so that the effect of top foil involved in Larsen model is negligible. Moreover, the friction coefficient involved in the Iordanoff model significantly impacted the foil stiffness. At low eccentricity ratios, the results coincide whatever the value of the friction coefficient. However, at high eccentricity ratios, an increase in the friction coefficient leads to an increase in the load capacity since the bump compliance factor is decreased and foil deflection is increased.

(vii). Bearings with inlet slope height seemed to increase or decrease the load capacity, depending on the bearings configuration and eccentricity ratio.

Finally, the last chapter has been dedicated to the application of the numerical method to a specific bearing configuration. Results for the two pads bearing developed by Omega Dot and used by Mitis SA have been presented. The main results were that load capacity increases with rotation speed, especially at high eccentricity ratios. Clearance axial variation (due to temperature effect) had a relatively high impact on static performance parameters.

7.5 Perspectives

In light of the results of the findings through this present work, it is clear that future work should be considered to improve the current status and conclude the results of this work.

Regarding the foils modelling, the analytical stiffness models used in the present work seem to overestimate the flexibility of the foils since they do not consider bump-bump interactions. An advanced mathematical model capturing the actual mechanical behaviour of the foils should be developed. A fascinating and widely used model is that developed by Le Lez [28]. The model describes the bump foil structure as interacting bumps (three degrees of freedom per bump, *i.e.* horizontal and vertical displacement and rotation) connected by elementary springs that have analytically expressed stiffness so that the model can be adjusted for a wide range of diameters and material properties. This model has, therefore, the advantage of being easily integrated into the numerical code developed in the frame of this work. Note that this model is only valid for bump foil. However, the author believes that by adding some nodes and elementary springs between the top of the bumps, an analytical model describing the top foil could be obtained. Other complex FE models coupling the elastic deflection of the 1D beam-like or 2D shell top foil to the gas film hydrodynamics exist [34]. A frictional model considering the dissipation by sliding forces in the foil structure must be added. A good example is given in [65].

Regarding the dynamics of the rigid rotor, a mathematical model proposed by [54] and used by [65] could be used. The derivation model is based on Newton's second law and describes the shaft with two nodes at its extremities. Two degrees of freedom, the horizontal and vertical displacement, are related to each node. The model considers the shaft mass, transverse mass moment of inertia, and gyroscopic moment of inertia. The equations of motion (steady or transient) are then solved by introducing the reaction forces from the bearings, obtained by solving the Reynolds equation.

Appendices

Appendix A

Gas journal bearings solutions

A.1 Pressure perturbation solution

In 1959, Ausman used the perturbation method to linearize Eq. (3.1) in order to obtain an approximate analytical solution. This is is done by substituting Eq. (A.1) into Eq. (3.1).

$$p = p_a + \varepsilon p_1 + \varepsilon^2 p_2 + \ldots . \tag{A.1}$$

By neglecting all terms of order ε^2 or higher, Eq. (3.1) can be solved for the first order (in ε) perturbation pressure. After integration, the dimensionless load components are [22]

$$\begin{aligned} W_x^{(1)} &= \frac{w_x^{(1)}}{p_a L D} = \left(\frac{\pi}{2}\right) \frac{\varepsilon \Lambda}{1+\Lambda^2} \left[\Lambda + f_x\left(\Lambda, \frac{L}{D}\right)\right] \\ W_y^{(1)} &= \frac{w_z^{(1)}}{p_a L D} = \left(\frac{\pi}{2}\right) \frac{\varepsilon \Lambda}{1+\Lambda^2} \left[1 - f_y\left(\Lambda, \frac{L}{D}\right)\right] \end{aligned} \tag{A.2}$$

with

$$\begin{aligned} f_x\left(\Lambda, \frac{L}{D}\right) &= \frac{(\sigma - \xi \Lambda) \sin\left(2\xi \frac{L}{D}\right) - (\sigma \Lambda + \xi) \sinh\left(2\sigma \frac{L}{D}\right)}{\frac{L}{D}\sqrt{1+\Lambda^2}\left[\cosh\left(2\sigma \frac{L}{D}\right) + \cos\left(2\xi \frac{L}{D}\right)\right]} \\ f_y\left(\Lambda, \frac{L}{D}\right) &= \frac{(\sigma - \xi \Lambda) \sinh\left(2\sigma \frac{L}{D}\right) + (\sigma \Lambda + \xi) \sin\left(2\xi \frac{L}{D}\right)}{\frac{L}{D}\sqrt{1+\Lambda^2}\left[\cosh\left(2\sigma \frac{L}{D}\right) + \cos\left(2\xi \frac{L}{D}\right)\right]} \end{aligned} \tag{A.3}$$

and

$$\begin{aligned} \sigma &= \sqrt{\frac{\left(1+\Lambda^2\right)^{1/2} + 1}{2}} \\ \xi &= \sqrt{\frac{\left(1+\Lambda^2\right)^{1/2} - 1}{2}} \end{aligned} \tag{A.4}$$

with resultant dimensionless load $W^{(1)}$ and attitude angle $\Phi^{(1)}$

$$W^{(1)} = \sqrt{\left(W_x^{(1)}\right)^2 + \left(W_y^{(1)}\right)^2}, \qquad \Phi^{(1)} = \tan^{-1}\left(\frac{W_y^{(1)}}{W_x^{(1)}}\right) \tag{A.5}$$

A.2 Linearized *ph* solution

The linearized *ph* solution for gas-lubricated journal bearings comes as generalization and improvement of the first order perturbation solution. This method, also developed by Asuman [5], result in linear load-eccentricity ratio curve (see Eq. (A.2)) which gives good results for small eccentricity ratio ($\varepsilon < 1/2$). The linezarization principle is the same except that the product *ph* is considered to be the dependant variable. By substituting Eq. (A.6) into Eq. (3.1).

$$ph = p_a C + \Delta(ph) \tag{A.6}$$

Again, by considering only first order (in eccentricity) terms as solving for the first order perturbation equation, the pressure can be obtained

$$p = \frac{p_a}{1+\varepsilon\cos\theta}\left(1+\varepsilon\frac{\Lambda}{1+\Lambda^2}\left[g_1(\zeta)\sin\theta + g_2(\zeta)\cos\theta\right]\right) \tag{A.7}$$

where

$$\begin{aligned} g_1(\zeta) &= 1 - \mathrm{A}\,\sinh(\sigma\zeta)\sin(\xi\zeta) + \mathrm{B}\,\cosh(\sigma\zeta)\cos(\xi\zeta) \\ g_2(\zeta) &= \frac{1}{\Lambda} + \mathrm{A}\,\cosh(\sigma\zeta)\cos(\xi\zeta) + \mathrm{B}\,\sinh(\sigma\zeta)\sin(\xi\zeta) \end{aligned} \tag{A.8}$$

and

$$\begin{aligned} \mathrm{A} &= \frac{\Lambda\cosh\left(\sigma\frac{L}{D}\right)\cos\left(\xi\frac{L}{D}\right) + \sinh\left(\sigma\frac{L}{D}\right)\sin\left(\xi\frac{L}{D}\right)}{\sinh^2\left(\sigma\frac{L}{D}\right) + \cos^2\left(\xi\frac{L}{D}\right)} \\ \mathrm{B} &= \frac{\Lambda\sinh\left(\sigma\frac{L}{D}\right)\sin\left(\xi\frac{L}{D}\right) - \cosh\left(\sigma\frac{L}{D}\right)\cos\left(\xi\frac{L}{D}\right)}{\sinh^2\left(\sigma\frac{L}{D}\right) + \cos^2\left(\xi\frac{L}{D}\right)} \end{aligned} \tag{A.9}$$

After integration, the dimensionless load components, the resultant load $W^{(ph)}$ and the attitude angle $\Phi^{(ph)}$ can be expressed as a function of those obtained with the first order pressure perturbation

$$\begin{aligned} W_x^{(ph)} &= \frac{2}{\varepsilon^2}\left[\frac{1-\left(1-\varepsilon^2\right)^{1/2}}{\left(1-\varepsilon^2\right)^{1/2}}\right] W_x^{(1)} \\ W_y^{(ph)} &= \frac{2}{\varepsilon^2}\left[1-\left(1-\varepsilon^2\right)^{1/2}\right] W_y^{(1)} \end{aligned} \tag{A.10}$$

and therefore

$$W^{(ph)} = \frac{2W^{(1)}}{\varepsilon^2}\left[\frac{1-\left(1-\varepsilon^2\right)^{1/2}}{\left(1-\varepsilon^2\right)^{1/2}}\right]\sqrt{1-\varepsilon^2\sin^2\Phi^{(1)}}, \qquad \Phi^{(ph)} = \sqrt{1-\varepsilon^2}\,\tan\Phi^{(1)} \tag{A.11}$$

Note that in first order pressure perturbation method and linearized *ph* method, the *x*-axis is pointing right and the *y*-axis is pointing upward.

Appendix B

Iordanoff's compliance

- **Welded bump** The welded bump is assumed to be fixed at one end and free at the other one. Local compliance α_I^{fw} is given by

  $$\alpha_I^{fw} = \frac{12 p_a S_b J\left(\theta_b, \mu_f\right)}{E C \sin^3 \theta_b} \left(\frac{l_b}{t_b}\right)^3 \left(1 - \nu_b^2\right) \tag{B.1}$$

  with

  $$J = y_a \left[\left(\cos\theta_b - 1\right)\left(\sin\theta_b + \mu_f \cos\theta_b\right) + \frac{\mu_f (1 - \cos(2\theta_b))}{4} \right] + (1 - y_a)\left(\frac{\theta_b}{2} - \frac{\sin(2\theta_b)}{4}\right) \tag{B.2}$$

  $$y_a = \frac{-\left(\frac{3\sin(2\theta_b)}{4} - \frac{\theta_b}{2} - \sin\theta_b\right)}{2\theta_b \sin\theta_b \left(\sin\theta_b + \mu_f \cos\theta_b\right) - 2\mu_f \sin^2\theta_b + \theta_b - \frac{\sin(2\theta_b)}{2}} \tag{B.3}$$

- **Free bump** The free bump is free at its extremities. Local compliance α_I^{ff} is then

  $$\alpha_I^{ff} = \frac{6 p_a S_b I\left(\theta_b, \mu_f\right)}{E C \sin^3 \theta_b} \left(\frac{l_b}{t_b}\right)^3 \left(1 - \nu_b^2\right) \tag{B.4}$$

  with

  $$\begin{aligned} I = \left(A^2 + \frac{1 + \mu_f^2}{2}\right)\theta_b - \frac{\left(1 - \mu_f^2\right)\sin(2\theta_b)}{4} - \frac{\mu_f(\cos(2\theta_b) - 1)}{2} \\ - 2A\left[1 - \cos\theta_b + \mu_f \sin\theta_b\right] \end{aligned} \tag{B.5}$$

  $$A = \sin\theta_b + \mu_f \cos\theta_b \tag{B.6}$$

Note that both formulas considers Coulomb friction forces between bump and bearing housing [20].

Appendix C

Jumb and average operators

Following the convention presented in section 4.1.1, one can define the jump operator

$$\begin{aligned} [[a]] &= a^+\boldsymbol{n}^+ + a^-\boldsymbol{n}^- \\ [[\boldsymbol{a}]] &= \boldsymbol{a}^+\cdot\boldsymbol{n}^+ + \boldsymbol{a}^-\cdot\boldsymbol{n}^- \\ [[\boldsymbol{a}]]_\otimes &= \boldsymbol{a}^+\boldsymbol{n}^+ + \boldsymbol{a}^-\boldsymbol{n}^- \end{aligned} \tag{C.1}$$

The jump of a scalar is a vector whereas for vectors quantities, the jump can be defined as the inner product, resulting in a scalar and as an outer product resulting in a second order tensor.

The average operator is defined as follows

$$\begin{aligned} \langle a\rangle &= \frac{a^+ + a^-}{2} \\ \langle \boldsymbol{a}\rangle &= \frac{\boldsymbol{a}^+ + \boldsymbol{a}^-}{2} \end{aligned} \tag{C.2}$$

From these considerations, the following identity can be proved

$$[[a\boldsymbol{b}]] = \langle a\rangle[[\boldsymbol{b}]] + [[a]]\cdot\langle\boldsymbol{b}\rangle \tag{C.3}$$

Bibliography

[1] Osborne Reynolds. “On the theory of lubrication and its application to Mr. Beauchamp tower’s experiments, including an experimental determination of the viscosity of olive oil”. *Philosophical transactions of the Royal Society of London* 177 (1886), pp. 157–234.

[2] Sommerfeld A. “Zur hydrodynamischen theori eder schmiermittelreibung.” *Journal of Mathematics and Physics* (1904).

[3] A Cameron and WL Wood. “The full journal bearing”. *Proceedings of the Institution of Mechanical Engineers* 161.1 (1949), pp. 59–72.

[4] LN Tao. “General solution of Reynolds equation for a journal bearing of finite width”. *Quarterly of Applied Mathematics* 17.2 (1959), pp. 129–136.

[5] JS Ausman. “An improved analytical solution for self-acting, gas-lubricated journal bearings of finite length” (1961).

[6] S Ramachandra. “A solution of Reynolds equation for a full finite journal bearing” (1961).

[7] MA Barnett and A Silver. *Application of air bearings to high-speed turbomachinery*. Tech. rep. SAE Technical Paper, 1970.

[8] William H Reed and Thomas R Hill. *Triangular mesh methods for the neutron transport equation*. Tech. rep. Los Alamos Scientific Lab., N. Mex.(USA), 1973.

[9] Ruscitto et al. *Hydrodynamic Air Lubricated Compliant Surface Bearing for an Automotive Gas Turbine Engine: Bhushan, B., Ruscitto, D., Gray, S. Materials and coatings*. Vol. 2. Department of Energy, Office of Conservation and Solar Applications . . ., 1978.

[10] H Heshmat, JA Walowit, and O Pinkus. “Analysis of gas-lubricated foil journal bearings” (1983).

[11] C-P Roger Ku and H Heshmat. “Compliant foil bearing structural stiffness analysis: part I—theoretical model including strip and variable bump foil geometry” (1992).

[12] Christopher McAuliffe and Paul J Dziorny. *Bearing cooling arrangement for air cycle machine*. US Patent 5,113,670. May 1992.

[13] H Heshmat and P Hermel. “Compliant foil bearings technology and their application to high speed turbomachinery”. In: *Tribology Series*. Vol. 25. Elsevier, 1993, pp. 559–575.

[14] C-P Roger Ku and Hooshang Heshmat. “Compliant foil bearing structural stiffness analysis—part II: experimental investigation” (1993).

[15] J-P Peng and M Carpino. “Calculation of stiffness and damping coefficients for elastically supported gas foil bearings” (1993).

[16] J-P Peng and M Carpino. “Coulomb friction damping effects in elastically supported gas foil bearings©”. *Tribology transactions* 37.1 (1994), pp. 91–98.

[17] Giri L Agrawal. “Foil air/gas bearing technology—an overview”. In: *Turbo Expo: Power for Land, Sea, and Air*. Vol. 78682. American Society of Mechanical Engineers. 1997, V001T04A006.

[18] Giri L Agrawal. "Foil air/gas bearing technology—an overview". *Turbo Expo: Power for Land, Sea, and Air* 78682 (1997), V001T04A006.

[19] Bill Wilson. "History of Tribology". *Industrial Lubrication and Tribology* (1998).

[20] I Iordanoff. "Analysis of an aerodynamic compliant foil thrust bearing: method for a rapid design" (1999).

[21] Christopher DellaCorte and Mark J Valco. "Load capacity estimation of foil air journal bearings for oil-free turbomachinery applications". *Tribology Transactions* 43.4 (2000), pp. 795–801.

[22] Bernard J Hamrock, Steven R Schmid, and Bo O Jacobson. *Fundamentals of fluid film lubrication*. CRC press, 2004.

[23] Z-C Peng and MM Khonsari. "Hydrodynamic analysis of compliant foil bearings with compressible air flow". *J. Trib.* 126.3 (2004), pp. 542–546.

[24] EP Petrov and DJ Ewins. "Generic friction models for time-domain vibration analysis of bladed disks". *J. Turbomach.* 126.1 (2004), pp. 184–192.

[25] Daniel Lubell, Christopher DellaCorte, and Malcolm Stanford. "Test evolution and oil-free engine experience of a high temperature foil air bearing coating". In: *Turbo Expo: Power for Land, Sea, and Air*. Vol. 42401. 2006, pp. 1245–1249.

[26] Frank M White and Joseph Majdalani. *Viscous fluid flow*. Vol. 3. McGraw-Hill New York, 2006.

[27] Jan S Hesthaven and Tim Warburton. *Nodal discontinuous Galerkin methods: algorithms, analysis, and applications*. Springer Science & Business Media, 2007.

[28] Szbastien Le Lez, Mihaı Arghir, and Jean Frene. "A new bump-type foil bearing structure analytical model". In: *Turbo Expo: Power for Land, Sea, and Air*. Vol. 47942. 2007, pp. 747–757.

[29] Luis San Andre
s and Tae Ho Kim. "Improvements to the analysis of gas foil bearings: Integration of top foil 1d and 2d structural models". In: *Turbo Expo: Power for Land, Sea, and Air*. Vol. 47942. 2007, pp. 779–789.

[30] Christopher DellaCorte. "Technical development path for foil gas bearings". In: *International Joint Tribology Conference*. Vol. 43369. 2008, pp. 299–302.

[31] Tae Ho Kim and Luis San Andrés. "Heavily loaded gas foil bearings: a model anchored to test data". *Journal of Engineering for Gas Turbines and Power* 130.1 (2008).

[32] Daejong Kim and Soongook Park. "Hydrostatic air foil bearings: Analytical and experimental investigation". *Tribology International* 42.3 (2009), pp. 413–425.

[33] Krzysztof Nalepa, Paweł Pietkiewicz, and Grzegorz Żywica. "Development of the foil bearing technology". *Technical Sciences* 12 (2009), pp. 229–240.

[34] Luis San Andrés and Tae Ho Kim. "Analysis of gas foil bearings integrating FE top foil models". *Tribology International* 42.1 (2009), pp. 111–120.

[35] Andras Z Szeri. *Fluid film lubrication*. Cambridge university press, 2010.

[36] Daniele Antonio Di Pietro and Alexandre Ern. *Mathematical aspects of discontinuous Galerkin methods*. Vol. 69. Springer Science & Business Media, 2011.

[37] Samuel A Howard and Luis San Andrés. "A new analysis tool assessment for rotordynamic modeling of gas foil bearings". *Journal of engineering for gas turbines and power* 133.2 (2011).

[38] Shuangbiao Liu. "On boundary conditions in lubrication with one dimensional analytical solutions". *Tribology International* 48 (2011), pp. 182–190. DOI: `10.1016/j.triboint.2011.11.021`.

[39] Bernardo Cockburn, George E Karniadakis, and Chi-Wang Shu. *Discontinuous Galerkin methods: theory, computation and applications*. Vol. 11. Springer Science & Business Media, 2012.

[40] Dimitris Sfyris and Athanasios Chasalevris. “An exact analytical solution of the Reynolds equation for the finite journal bearing lubrication”. *Tribology International* 55 (2012), pp. 46–58.

[41] Timothy J Barth and Herman Deconinck. *High-order methods for computational physics*. Vol. 9. Springer Science & Business Media, 2013.

[42] Koen Hilleweart. “Development of the discontinuous Galerkin method for high-resolution, large scale CFD and acoustics in industrial geometries”. Doctoral dissertation. Louvain-la-Neuve, 2013.

[43] Milind Babasaheb Patil, Karuna Kalita, and Sashindra K Kakoty. “Performance analysis of gas foil bearing with different foil pivot configuration”. *Advances in Mechanical Engineering* 5 (2013), p. 843419.

[44] Ethirajan Rathakrishnan. *Theoretical aerodynamics*. John Wiley & Sons, 2013.

[45] Gwidon W Stachowiak and Andrew W Batchelor. *Engineering tribology*. Butterworth-heinemann, 2013.

[46] Philip Bonello and Hai Minh Pham. “The efficient computation of the nonlinear dynamic response of a foil–air bearing rotor system”. *Journal of Sound and Vibration* 333.15 (2014), pp. 3459–3478.

[47] TM Jamir and SK Kakoty. “Load Capacity Analysis of Gas Foil Bearing (GFB) for Different Foil Materials”. In: *Proceedings of International Conference on Advances in Tribology and Engineering Systems*. Springer. 2014, pp. 331–343.

[48] Jon S Larsen, Alejandro C Varela, and Ilmar F Santos. “Numerical and experimental investigation of bump foil mechanical behaviour”. *Tribology International* 74 (2014), pp. 46–56.

[49] Jong Sung Lee and Tae Ho Kim. “Analysis of Three-Pad Gas Foil Journal Bearing for Increasing Mechanical Preloads”. *Tribology and Lubricants* 30.1 (2014), pp. 1–8.

[50] Kyuho Sim, Yong-Bok Lee, and Tae Ho Kim. “Rotordynamic analysis of an oil-free turbocharger supported on lobed gas foil bearings—predictions versus test data”. *Tribology Transactions* 57.6 (2014), pp. 1086–1095.

[51] Christoph Baum, Hartmut Hetzler, and Wolfgang Seemann. “On the stability of balanced rigid rotors in air foil bearings”. *Proceedings of the SIRM* (2015).

[52] Dorota Kozanecka et al. “Experimental research of oil-free support systems to predict the high-speed rotor bearing dynamics”. *International Journal of Dynamics and Control* 3.1 (2015), pp. 9–16.

[53] Jon S Larsen and Ilmar F Santos. “Efficient solution of the non-linear Reynolds equation for compressible fluid using the finite element method”. *Journal of the Brazilian Society of Mechanical Sciences and Engineering* 37.3 (2015), pp. 945–957.

[54] Jon Steffen Larsen. *Nonlinear Analysis of Rotors Supported by Air Foil Journal Bearings-Theory & Experiments*. DTU Mechanical Engineering, 2015.

[55] Balaji Sankar and Sadanand Kulkarni. “Modeling of gas lubricated compliant foil bearings using pseudo spectral scheme”. *Tribology Online* 10.5 (2015), pp. 295–305.

[56] Saeid Dousti and Paul Allaire. “A compressible hydrodynamic analysis of journal bearings lubricated with supercritical carbon dioxide”. In: *Proceeding of supercritical CO2 power cycle symposium, San Antonio, TX*. 2016.

[57] Robert Hoffmann and Robert Liebich. “Experimental and numerical analysis of the dynamic behaviour of a foil bearing structure affected by metal shims”. *Tribology International* 115 (2017), pp. 378–388.

[58] Michael M Khonsari and E Richard Booser. *Applied tribology: bearing design and lubrication*. John Wiley & Sons, 2017.

[59] T Leister, C Baum, and W Seemann. “On the importance of frictional energy dissipation in the prevention of undesirable self-excited vibrations in gas foil bearing rotor systems”. *Technische Mechanik-European Journal of Engineering Mechanics* 37.2-5 (2017), pp. 280–290.

[60] Hooshang Heshmat, JF Walton, and José Luis Córdova. “Technology readiness of 5th and 6th generation compliant foil bearing for 10 MWE s-CO2 turbomachinery systems”. In: *Proceeding of the 6th International Supercritical CO2 Power Cycles Symposium. Pittsburg, PA*. 2018.

[61] Tim Leister, Christoph Baum, and Wolfgang Seemann. “Computational analysis of foil air journal bearings using a runtime-efficient segmented foil model”. *Journal of Fluids Engineering* 140.2 (2018).

[62] Guo-Ping Wang, Shuang Cheng, and Hua-Ning Hao. “Recent progress on the structural styles of journal foil gas bearings”. In: *IOP Conference Series: Materials Science and Engineering*. Vol. 439. 4. IOP Publishing. 2018, p. 042016.

[63] P Samanta, NC Murmu, and MM Khonsari. “The evolution of foil bearing technology”. *Tribology international* 135 (2019), pp. 305–323.

[64] Nicolas Corthouts et al. “Travail de Fin d’Etudes: Discontinuous Galerkin Finite Element Method Applied to Plasma Flows” (2020).

[65] A. S. Von Osmanski. “Modelling of Gas Foil Bearings Towards Controllable Operation : Multi-domain Analysis”. PhD thesis. Technical University of Denmark. DCAMM Special Report No. S273, 2020.

[66] François Custinne et al. “Master thesis and internship [BR]-Master’s thesis: Plasma sheath modeling with a high order Discontinuous Galerkin Method [BR]-Integration internship” (2021).

[67] Yu Hou et al. “Application of gas foil bearings in China”. *Applied Sciences* 11.13 (2021), p. 6210.

[68] N. Leveux A. Bilcoq. “Computational Fluid Dynamics (guest lecture): Discontinuous Galerkin Method”. University of Liège, 2022.